Deep learning-based prognostics for fuel cells under variable load operating conditions

Chu Wang

NNT/NL : 2022AIXM0530/029ED184

THÈSE DE DOCTORAT

Soutenue à la Northwestern Polytechnical University, Xi'an, Chine
en cotutelle avec la Northwestern Polytechnical University
le 15 Décembre 2022 par

Chu Wang

Deep learning-based prognostics for fuel cells under variable load operating conditions

Discipline
Automatique

École doctorale
ED 184 Mathématiques et informatique

Laboratoire/Partenaires de recherche
Laboratoire d'informatique et systèmes

Composition du jury

Weiguo Liu Northwestern Polytechnical University	Président du jury
Zheng Xiang Xidian University	Rapporteur
Marie-Cécile Péra Université de Franche-Comté	Rapporteuse
Deliang Liang Xi'an Jiaotong University	Examinateur
Kamal Medjaher Université Fédérale Toulouse Midi-Pyrénées	Examinateur
Rachid Outbib Aix-Marseille Université	Directeur de thèse
Manfeng Dou Northwestern Polytechnical University	Directeur de thèse
Zhongliang Li Aix-Marseille Université	Co-directeur de thèse

Affidavit

I, undersigned, Chu Wang, hereby declare that the work presented in this manuscript is my own work, carried out under the scientific direction of Rachid Outbib, Manfeng Dou and Zhongliang Li, in accordance with the principles of honesty, integrity and responsibility inherent to the research mission. The research work and the writing of this manuscript have been carried out in compliance with both the French national charter for Research Integrity and the Aix-Marseille University charter on the fight against plagiarism.

This work has not been submitted previously either in this country or in another country in the same or in a similar version to any other examination body.

Place Xi'an, date 13 Septembre 2022

Signature : 

Liste de publications et participation aux conférences

1) Liste des publications réalisées dans le cadre du projet de thèse :

   1. **Chu Wang**, Zhongliang Li, Rachid Outbib, Manfeng Dou, Dongdong Zhao. Symbolic deep learning based prognostics for dynamic operating proton exchange membrane fuel cells. ***Applied Energy*** 2022; 305: 117918. (DOI: 10.1016/j.apenergy.2021.117918)

   2. **Chu Wang**, Zhongliang Li, Rachid Outbib, Manfeng DOU, Dongdong Zhao. A novel long short-term memory networks-based data-driven prognostic strategy for proton exchange membrane fuel cells. ***International Journal of Hydrogen Energy*** 2022; 47 (18): 10395-10408. **(ESI Highly Cited Papers)** (DOI: 10.1016/j.ijhydene.2022.01.121)

   3. **Chu Wang**, Manfeng Dou, Zhongliang Li, Rachid Outbib, Dongdong Zhao, Bin Liang. A fusion prognostics strategy for fuel cells operating under dynamic conditions. ***eTransportation*** 2022; 12: 100166. (DOI: 10.1016/j.etran.2022.100166)

   4. **Chu Wang**, Manfeng Dou, Zhongliang Li, Rachid Outbib, Dongdong Zhao, Jian Zuo, Yuanlin Wang, Bin Liang. Data-driven prognostics based on time-frequency analysis and symbolic recurrent neural network for fuel cells under dynamic load. ***Reliability Engineering and System Safety*** (under review).

2) Participation aux conférences pendant la période de thèse :

   1. **Chu Wang**, Zhongliang Li, Rachid Outbib, Dongdong Zhao, Manfeng Dou. Proton Exchange Membrane Fuel Cells Prognostic Strategy Based on Navigation Sequence Driven Long Short-term Memory Networks. ***IECON 2020*** *The 46th Annual Conference of the IEEE Industrial Electronics Society*, Singapore, 2020: 3969-3974 (oral presentation). (DOI: 10.1109/IECON43393.2020.9255373)

   2. **Chu Wang**, Zhongliang Li, Rachid Outbib, Dongdong Zhao, Manfeng Dou. A Hybrid Prognostics Approach for Proton Exchange Membrane Fuel Cells under Dynamic Operating Conditions. ***EVS34*** *The 34th World Electric Vehicle Symposium & Exhibition*, Nanjing, 2021 (oral presentation). **(Best Paper Award)**

Résumé

Les systèmes de pile à combustible à membrane échangeuse de protons (PEMFC) conviennent à diverses applications de transport grâce à leurs structure compacte, densité de puissance élevée, faible température de démarrage/fonctionnement et absence d'émissions de carbone. Le coût élevé et le manque de durabilité des PEMFC restent les principaux facteurs limitant leur commercialisation à grande échelle. Dans les applications de transport, la détérioration des PEMFC est aggravée par des conditions de charge variables, ce qui entraîne une diminution de leur durée de vie utile restante (RUL). La gestion des pronostics et de la santé (PHM) est un outil efficace pour prévoir les risques du système, gérer les calendriers de contrôle/maintenance du système, améliorer la sécurité et la fiabilité du système, prolonger la durée de vie du système et réduire les coûts d'exploitation/maintenance. Le pronostic est une base importante et un support clé pour le PHM, et ses tâches principales incluent l'extraction d'indicateurs de santé, la prédiction des tendances de dégradation et l'estimation de la RUL. Les caractéristiques de dégradation à long terme des PEMFC sont dissimulées dans des conditions de charge variables, ce qui augmente la difficulté d'extraction des indicateurs de santé, réduit la précision de la prédiction de la dégradation et inhibe la fiabilité de l'estimation de la durée de vie. Dans cette optique, le travail de thèse part de la modélisation du comportement de dégradation des PEMFC dans des conditions de charge variables et mène des travaux de recherche sur l'extraction d'indicateurs de santé, la prédiction des tendances de dégradation à court/long terme, l'estimation RUL et l'évaluation de la fiabilité. Les principaux contenus de recherche et contributions de la thèse sont les suivants : (1) extraction en temps réel des indicateurs de santé des piles à combustible dans des conditions de charge variables ; (2) prévision des tendances de la dégradation des piles à combustible à court/long terme basée sur les données ; et (3) prédiction RUL dans des conditions de charge variables basées sur des méthodes hybrides.

Mots clés : pile à combustible à membrane échangeuse de protons, pronostic, comportement de détérioration, apprentissage profond, conditions de charge variables, indicateur de santé, durée de vie utile restante, horizon de pronostic

Abstract

Proton Exchange Membrane Fuel Cell (PEMFC) systems are suitable for various transportation applications thanks to their compact structure, high power density, low start/running temperature, and zero carbon emissions. High cost and lack of durability of PEMFC are still the core factors limiting their large-scale commercialization. In transportation applications, the deterioration of PEMFCs is aggravated by variable load conditions, resulting in a decrease in their Remaining Useful Life (RUL). Prognostics and Health Management (PHM) is an effective tool to forecast potential system risks, manage system control/maintenance schedules, improve system safety and reliability, extend system life, and reduce operation/maintenance costs. Prognostics is an important foundation and key support for PHM, and its core tasks include health indicator extraction, degradation trend prediction, and RUL estimation. The long-term degradation characteristics of PEMFC are concealed in variable load conditions, which increases the difficulty of health indicator extraction, reduces the accuracy of degradation prediction, and inhibits the reliability of life estimation. In view of this, the thesis work starts from modeling the degradation behavior of PEMFC under variable load conditions and carries out research work on health indicator extraction, short/long-term degradation trend prediction, RUL estimation and reliability evaluation. The main research contents and contributions of the thesis are as follows: (1) real-time extraction of fuel cell health indicators under variable load conditions; (2) data-driven short/long-term fuel cell degradation trend prediction; and (3) RUL prediction under variable load conditions based on hybrid methods.

Keywords: proton exchange membrane fuel cell, prognostics, deterioration behavior, deep Learning, variable load conditions, health indicator, remaining useful life, prognostic horizon

Acknowledgements

To begin with, I would like to express my heartfelt gratitude to my two supervisors, Prof. Rachid Outbib and Prof. Manfeng Dou, and my co-supervisor, Dr. Zhongliang Li. Retrospectively, I feel extremely fortunate to have worked with them. I thank them for their patient guidance and kind help. When I encountered difficulties and setbacks, they always offered unreserved support and encouragement. I appreciate their teaching me how to dig into scientific problems in practical applications. Their actions helped me to understand the importance of finding a good "problem" and trying to describe it clearly in the simplest terms. This is obviously particularly important for scientific research, and sometimes even more challenging than solving the "problem". They have been a beacon and role model for me in my academic career.

I am very grateful to Prof. Dongdong Zhao, Dr. Meiling Yue, Dr. Zhiguang Hua, Dr. Jian Zuo, Mr. Liang Guo, and Mr. Hanbin Dang. I thank them for their help in the academic field, especially for their constructive comments and impressive ideas in the online/offline seminars. Their radiant achievements in the field and their dedication to scientific work will also continue to spur me on.

I would like to thank Prof. Rémy Bulot, Prof. Bernard Espinasse, Ms. Sonia Asseum, Ms. Géraldine Callier, Ms. Béatrice Alcala, Ms. Véronique Bianciotto from Aix-Marseille University. As well as Dr. Lan Yang from Xidian University. They provided me with crucial support and assistance for my PhD dissertation.

Furthermore, I would like to sincerely thank my colleagues in the lab group belonging to Northwestern Polytechnical University. In particular, Dr. Yuanlin Wang, Dr. Jianwei Yang, Dr. Liming Yan, Dr. Haitao Zhang, Mr. Changliang Dang, Ms. Mengxi Dang, Mr. Shuhao Yan, Mr. Zhibing Ma, Mr. Liheng Xu, Mr. Sixun Du, Mr. Tian Jin, Mr. Bo Zhou, Mr. Yanwei Zhang, Mr. Heming Yang, Mr. Qiwei Xia, and Mr. Xuan Wu. It is pleasant and comfortable to work with them, and I thank them for all the efforts they put into my dissertation. I would especially like to thank my housemates at Northwestern Polytechnical University, Mr. Bofan Guan and Mr. Weizhou Yang, for accompanying me through an unforgettable campus life, and wish them all the best in their future endeavors.

Please allow me to express my sincere gratitude to my beloved family. I thank them for their unconditional devotion to me and for giving me enough freedom to choose the ideal way of life. They are like the brightest stars in the night sky, guiding me when I lose my way. They are also my warmest harbor, soothing me when I am tired and frustrated, always bringing me peace and hope.

Nomenclature

Abbreviations

PEMFC	Proton Exchange Membrane Fuel Cell
PHM	Prognostics and Health Management
RUL	Remaining Useful Life
FC	Fuel Cells
SOFC	Solid Oxide Fuel Cell
PAFC	Phosphoric Acid Fuel Cell
MCFC	Molten Carbonate Fuel Cell
DMFC	Direct Methanol Fuel Cell
AFC	Alkaline Fuel Cell
DOE	The United States Department of Energy
FCEV	Fuel Cell Electric Vehicle
SoH	State of Health
ISO	The International Organization for Standardization
HI	Health Indicators
WOS	Web of Science
DNN	Deep Neural Network
ESN	Echo State Network
LPV	Linear Parameter Varying
LSTM	Long Short-Term Memory (a. k. a., Raw-LSTM or Vanilla-LSTM)
ARIMA	Autoregressive Integrated Moving Average
C-V	Current Density-Voltage (Curve)
ARIMAX	Autoregressive Integrated Moving Average Model with Exogenous Variables
ABBA	Adaptive Brownian Bridge-based Aggregation
ABBA-LSTM	An LSTM model with ABBA
GRU	Gated Recurrent Unit
ABBA-GRU	ABBA-based Gated Recurrent Unit
HHT	Hilbert-Huang Transform
CV	Cyclic Voltammetry
ECSA	Electrochemcial Active Surface Area
EIS	Electrochemical Impedance Spectroscopy
RNN	Recurrent Neural Network
NS	Navigation Sequence
NSD-LSTM	Navigation Sequence Driven LSTM

NARX	Nonlinear Autoregressive Exogenous
XS	Exogenous Sequences
FT	Failure Threshold
EoL	End of Life
SD	Standard Deviation
LOESS	Locally Estimated Scatterplot Smoothing
CI	Confidence Interval
RMSE	Root-Mean-Square Error
RE	Relative Error
AST	Accelerated Stress Test
IV	Instrumental Variable
WCSS	Within-Cluster Sum of Squares
PFR	Probable Failure Range
CFR	Calculable Failure Range
NEDC	New European Driving Cycle
PH	Prognostics Horizon
TA	Trust Area
CBM	Condition-Based Maintenance
IMF	Intrinsic Mode Function
EMD	Empirical Mode Decomposition
HT	Hilbert Transform
HSA	Hilbert Spectral Analysis
IF	Instantaneous Frequency
PDF	Probability Distribution Function
RA	Relative Accuracy
LPV-ARX	LPV Identification for Autoregressive Model with Exogenous Input Model

Symbol

H_2	Hydrogen
O_2	Oxygen
H_2O	Water
H^+	Hydrogen ion
e^-	Electron
E_{act}	Operation voltage affected by activation losses only
E_{rev}	Open-circuit voltage of the fuel cell
V_{act}	Voltage drop triggered by the activation losses
E_r	Operation voltage affected by Ohmic losses only
V_r	Voltage drop induced by Ohmic losses
E_{conc}	Operation voltage affected by concentration losses only
V_{conc}	Voltage drop triggered by the concentration losses

E_{cell}	Actual (single cell) operation voltage
$\{x_{it}\}$	i-th input time sequence of ARIMAX
$\mathbb{R}^l$	l-dimensional time steps
$\{y_t\}$	Output time sequence of ARIMAX
μ	Mean vector of ARIMAX output sequence
ε_t	Regression residual sequence of ARIMAX
B	Backshift operator of input time sequence
L_i	i-th lag degree of backshift operator
$\Theta_i(B)$	Moving average polynomial of input time sequence
$\Phi_i(B)$	Autoregressive polynomial of input time sequence
$\theta(B)$	q-order moving average operator
$\phi(B)$	p-order autoregressive operator
a_t	Zero-mean white noise sequence
c_t	Cell state of LSTM
h_t	Hidden state of LSTM/GRU
f_t	Forget gate of LSTM
i_t	Input gate of LSTM
o_t	Output gate of LSTM
$\tilde{c}_t$	Internal state unit of LSTM
x_t	Input of LSTM
$\mathbb{R}^h$	h-dimensional hidden units
$\mathbb{R}^d$	d-dimensional input features
σ	Sigmoid function
tanh	Hyperbolic tangent function
$\circ$	Hadamard (element-wise) product
W_f	Input weight matrix of the forget gate
W_i	Input weight matrix of the input gate
W_o	Input weight matrix of the output gate
W_c	Input weight matrix of the cell state
$\mathbb{R}^{h\times d}$	$h \times d$-dimensional matrix
U_f	Recurrent weight matrix of the forget gate
U_i	Recurrent weight matrix of the input gate
U_o	Recurrent weight matrix of the output gate
U_c	Recurrent weight matrix of the cell state
$\mathbb{R}^{h\times h}$	$h \times h$-dimensional matrix
b_f	Bias of the forget gate
b_i	Bias of the input gate
b_o	Bias of the output gate
b_c	Bias of the cell state
t_0	Operating time at the split point, also prediction starting point
$\{z\}$	Raw training set sequence
$\overline{z}$	Average of raw training set sequence

$\{z_{std}\}$	Standardized training set sequence
$\hat{y}_k^i$	*i*-th predicted value of the *k*-th time step
$\overline{\hat{y}}_k$	Average predicted value of the *k*-th time step
SD_k	Identified standard deviation of the *k*-th time step
CI_k	Confidence interval bounds of the *k*-th time step
$\{\overline{\hat{y}}\}$	Average predicted value sequence, also navigation sequence
$\widehat{EoL}$	Estimated end of life (single failure threshold only)
$\widehat{RUL}$	Estimated remaining useful life (single failure threshold only)
u_j	*j*-th actual observations in the training set
$\hat{u}_j$	*j*-th predicted voltage value
v	Global overpotential
E_{stack}	Actual (stack) operation voltage
R_{dyn}	Dynamic resistance
R_{act}	Activation resistance, also Faradaic resistor
R_{conc}	Concentration resistance, also simplified Warburg element
C_{dl}	Double-layer capacitor
R_r	Ohmic resistance
j	Current density, also imaginary unit
j_{loss}	Crossover current density
j_{exch}	Exchange current density
j_{max}	Limiting current density
R	Molar gas constant (8.3145 J/mol/K)
F	Faraday constant (96485 C/mol)
α_{a+c}	Charge transfer coefficient from two electrodes
β_{a+c}	Mass transfer coefficient from two electrodes
T	Operating temperature (thermodynamic)
R_{equ}	Equivalent resistance
$j(t)$	Continuous-time input (time-varying current density)
$v(t)$	Continuous-time output (time-varying global overpotential)
$H(s)$	System transfer function
s	Complex variable
$J(s)$	Laplace transform of the input
$V(s)$	Laplace transform of the output
p_i	*i*-th Laplace variable of the denominator polynomial
q_i	*i*-th Laplace variable of the numerator polynomial
$L(s)$	Refined choice of filter
$A(s)$	Denominator of the system
$j'(t)$	First order derivatives of the input
$v'(t)$	First order derivatives of the output
$e(t)$	Disturbance of the system
$\varphi(t)$	Vector of variables containing actual output
θ	Parameter vector

$\hat{v}(t)$	Predicted output
$\zeta(t)$	Vector of variables containing predicted output
$\hat{\theta}$	Estimated parameters
X	Historical health indicator sequence for ABBA-LSTM
x_i	i-th element of health indicator
$\mathbb{R}^n$	n-dimensional health indicator
Q_j	j-th segments
$\mathbb{R}^m$	m-dimensional segments
$\tilde{x}_{i_h}$	h-th breakpoint
len_j	j-th time direction increment
inc_j	j-th numerical direction increment
tol	Tolerance parameter
D	Time and numerical increment tuples-set
$\mathbb{R}^{2\times m}$	$2 \times m$-dimensional tuples-set
D_j	j-th tuple of D
ω_{len}	Segment length weight
ω_{inc}	Segment increment weight
$\overline{D}_l$	l-th tuple of scaled set
σ_{len}	Standard deviation of the segment lengths
σ_{inc}	Standard deviation of the segment increments
S_l	l-th cluster
$\arg\min_{x\in S} f(x)$	Arguments x for which $f(x)$ attains its smallest value
$\|\cdot\|^2$	Euclidean norm
$\overline{\mu}_l$	Center of the l-th cluster
L	Alphabet set representing clusters' categories
k	Number of letter symbols in L
A	m-dimensional character series
sy_i	i-th letter symbol of A
B	p-dimensional predicted set of characters
b_j	i-th letter symbol of B
$\widehat{D}$	Predicted increments tuples-set
$l\hat{e}n_j$	j-th predicted time direction increment
$i\hat{n}c_j$	j-th predicted numerical direction increment
$\mathbb{R}^{2\times p}$	$2 \times p$-dimensional predicted tuples-set
Y	Predicted health indicator, also predicted degradation trend
y_i	Predicted health indicator at i-th time step
$\mathbb{R}^q$	q-dimensional predicted time steps
t_{limit}	Extreme point of recoverable fault
t_{end}	Complete failure point or data ending point
t_{a_1}	Expected earliest failure point
FT_i	i-th failure threshold
t_{a_i}	Actual end-of-life at FT_i

$\hat{Y}$	A series of predicted degradation trends at FT_i from multiple ABBA-LSTM models
Y_j	j-th predicted degradation trend
t_{i_j}	j-th predicted end-of-life at FT_i
RUL_i	A series of predicted RUL at FT_i
RUL_{i_j}	Predicted RUL corresponding to Y_j, also j-th element of RUL_i
RUL_{P_i}	Corresponds to the value of the horizontal coordinate of P_i
P_i	Probability density distribution based on RUL_i
$\widetilde{RUL}_i$	Final predicted RUL at FT_i, also the maximum of P_i
$\widehat{RUL}$	Final predicted RUL series at h failure thresholds
RUL_{a_i}	Actual RUL at FT_i
$\text{argmax}_{x \in S} f(x)$	Arguments x for which $f(x)$ attains its largest value
$\hat{E}_{cell}$	Identified/reconstructed single-cell voltage
TA_i	i-th trust area at FT_i
PH_i	i-th prognostics horizon at FT_i
α_{low}	Trust area lower limit tolerance factor
α_{up}	Trust area up limit tolerance factor
t_{1st_i}	Earliest time point after all predicted RULs are within TA_i
HI_i	i-th extracted health indicator
RE_E	Relative error of single-cell voltage
$x(t)$	Input signal of HHT
$e_{max}(t)$	Upper envelope curve
$e_{min}(t)$	Lower envelope curve
$m_{1,1}(t)$	Mean envelope function (first sifting of the first IMF)
$h_{1,j}(t)$	First component obtained at j-th repetition
$c_i(t)$	i-th IMF
$r_i(t)$	i-th residual
$r_n(t)$	Final residual
$\mathcal{H}_i(t)$	Hilbert transform of the residual
PV	Cauchy principal value
$z_i(t)$	Analytical function of $r_i(t)$
$a_i(t)$	Amplitude function
$\phi_i(t)$	Instantaneous phase function
$\omega_i(t)$	Instantaneous frequency
$\varepsilon_i(t)$	Instantaneous energy
ω_i^+	Frequency range upper bound of i-th residual
ω_i^-	Frequency range lower bound of i-th residual
$H(\omega_i, t)$	Hilbert spectrum of i-th residual
$Re[f(x)]$	Extract the real component of the function $f(x)$
h_{t-1}	Previous hidden state of GRU
a_t	Current symbol in the input of GRU
r_t	Reset gate of GRU

z_t	Update gate of GRU
W_r	Input weight matrix of the reset gate
W_z	Input weight matrix of the update gate
W_h	Input weight matrix of the hidden state
U_r	Unit internal weight matrix of the reset gate
U_z	Unit internal weight matrix of update gate
U_h	Unit internal weight matrix of the hidden state
b_r	Bias vector of the reset gate
b_z	Bias vector of the update gate
b_h	Bias vector of the hidden state
$\tilde{h}_t$	Unit internal hidden state vector
T_{FC1}	Operating temperature of FC-1
I_{FC1}	Operating load current of FC-1
$TA_i^{\alpha-\lambda}$	i-th trust area using the $\alpha-\lambda$ performance at FT_i
RA_i	Relative accuracy at i-th failure threshold

Contents

1. Introduction

1.1. Background

Energy, one of the eternal topics of mankind. Fossil fuels such as coal and oil have greatly contributed to the progress of civilization. Along with the rapid leap of economy, the per capita energy demand keeps climbing while non-renewable energy sources are depleting day by day. At the same time, fossil fuels, as carbon-based primary energy sources, inevitably emit greenhouse gases during the energy conversion process, aggravating environmental pollution.

Hydrogen energy, an ideal renewable and clean energy source, has abundant reserves and high combustion calorific value. Proper application of hydrogen energy will be expected to alleviate the shortage of fossil fuels and reduce carbon emissions [1, 2]. As one of the efficient ways to utilize hydrogen energy, Fuel Cells (FC) have been shown to convert chemical energy into electrical energy with efficiencies of 60% to 80%, making them a highly promising power generation device [3-6]. The main types of mass-produced commercial fuel cells include: Proton Exchange Membrane Fuel Cell (PEMFC), Solid Oxide Fuel Cell (SOFC), Phosphoric Acid Fuel Cell (PAFC), Molten Carbonate Fuel Cell (MCFC), Direct Methanol Fuel Cell (DMFC), Alkaline Fuel Cell (AFC), etc. The data in the Fuel Cell Industry Review 2019-2021 published by E4tech, an international consulting firm, shows that the annual shipments of fuel cells (by MW) continue to grow, jumping from less than 300 MW in 2015 to 2,313.1 MW in 2021. As shown in Figure 1.1, the shipments of PEMFC are the largest and growing the most among all types of fuel cells. In 2021 alone, PEMFC shipments have reached 1998.3 MW, which is already more than 86% of the total global fuel cell shipments in that year [7-9].

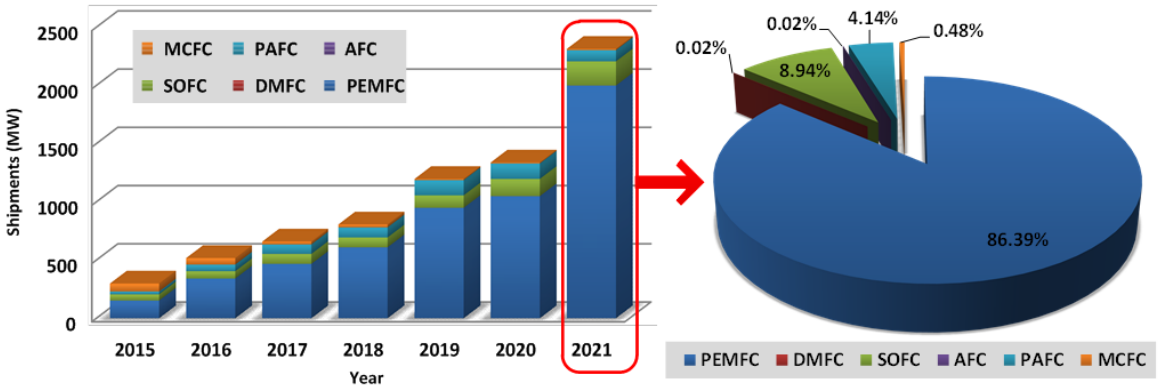

Figure 1.1 Shipments of different types of fuel cells (by megawatt).

The common application types of fuel cells involve transportation, stationary power generation, and portable devices, and as shown in Figure 1.2, fuel cell shipments (by

megawatt) applied to transportation have increased significantly year by year since 2015. By 2021, the share of fuel cell shipments in transportation applications has reached nearly 85%, with most of the contribution coming from proton exchange membrane fuel cells [7-11]. Typically, PEMFCs use hydrogen directly as fuel and their electrochemical reaction products are only water and heat during operation, allowing for zero carbon emissions. In addition, fuel cell power generation systems composed of PEMFC have the advantages of high electrical efficiency, fast start-up, low noise, low operating temperature, and scalable power/capacity. It is expected to be a strong competitor for the replacement of internal combustion engines and has already emerged in different applications in transportation (e.g., hybrid electric vehicles [12, 13], long-haul heavy-duty trucks [2], buses [14], trains [15], ships [16], etc.).

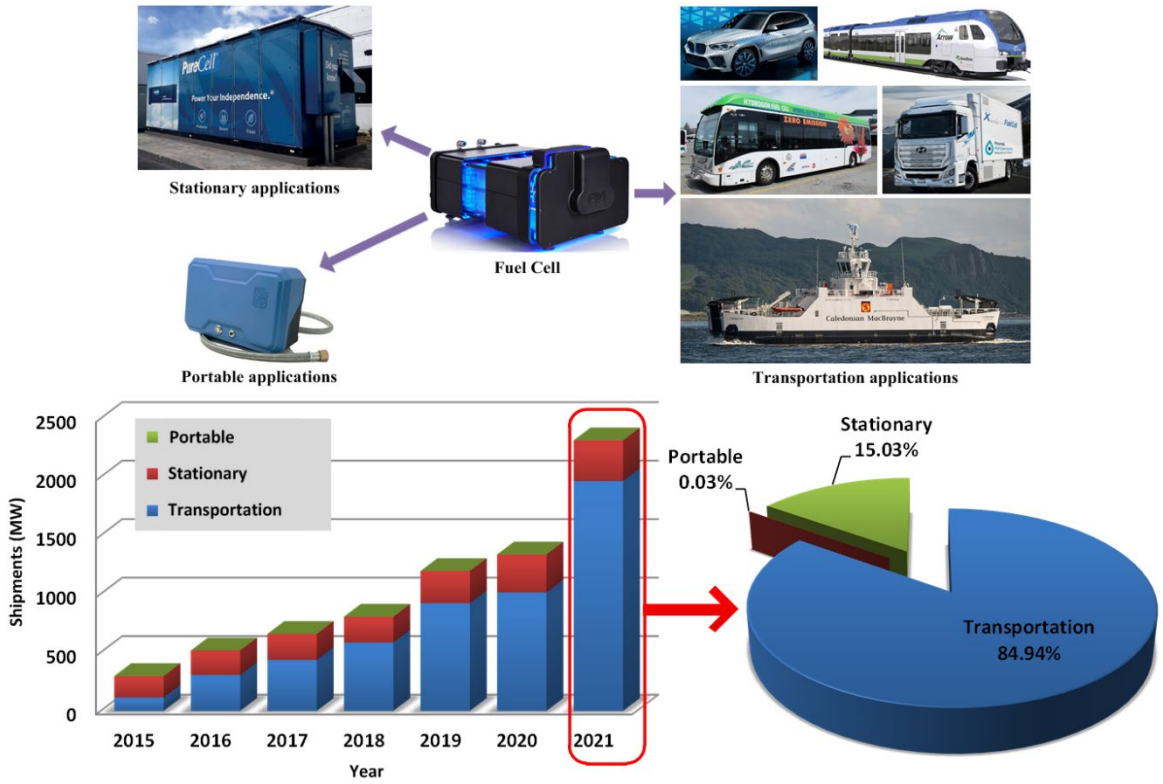

Figure 1.2 Common fuel cell application types and their annual shipments (by megawatt).

At present, insufficient durability and high cost are still the main constraints to achieve further large-scale commercialization of PEMFC. Especially in transportation applications, the actual useful life of PEMFCs is still far below the expected target [17-20]. The United States Department of Energy (DOE) has proposed an ultimate target of 8000 hours for the expected life of the Fuel Cell Electric Vehicle (FCEV), which is equivalent to 150,000 miles (approximately 240,000 km) of low-speed vehicle travel. Data from the report "Fuel Cell Electric Vehicle Durability and Fuel Cell Performance" published by the DOE's National Renewable Energy Laboratory shows that the average fleet durability of FCEVs operating on actual roads is about 2,000 hours and max fleet average durability is about 4,000 hours, both of which fall short of the interim goal set

by the DOE (5,000 hours). Even, some of the stacks of FCEVs operating for more than 5000 hours show up to 30% performance degradation. For on-board fuel cells in buses and long-haul heavy-duty trucks, the expected ultimate durability goal is 25,000 hours, but in practice the average lifetime of the stack is only about half of this goal [2, 4, 18, 21, 22]. PEMFCs are characterized by multi-physics, multi-variables, multi-subsystems, and multi-times/spatial scales, so their degradation triggers are abundant and the performance degradation process is complex [18]. In the transportation field, road conditions, driving styles, and other elements are random, sudden, and idiosyncratic. The actual load of the vehicle also exhibits time-varying characteristics. Usually, the operating condition of fuel cell under time-varying load is called variable load condition. At this situation, the PEMFC output power characteristics are heterogeneous. The water-thermal management and air supply control challenges are intensified, which are very likely to cause performance degradation and even induce abnormal shutdowns and fatal failures, affecting the service life [22-24]. Therefore, the lack of durability has become the core bottleneck problem faced in the promotion of PEMFC in the transportation field.

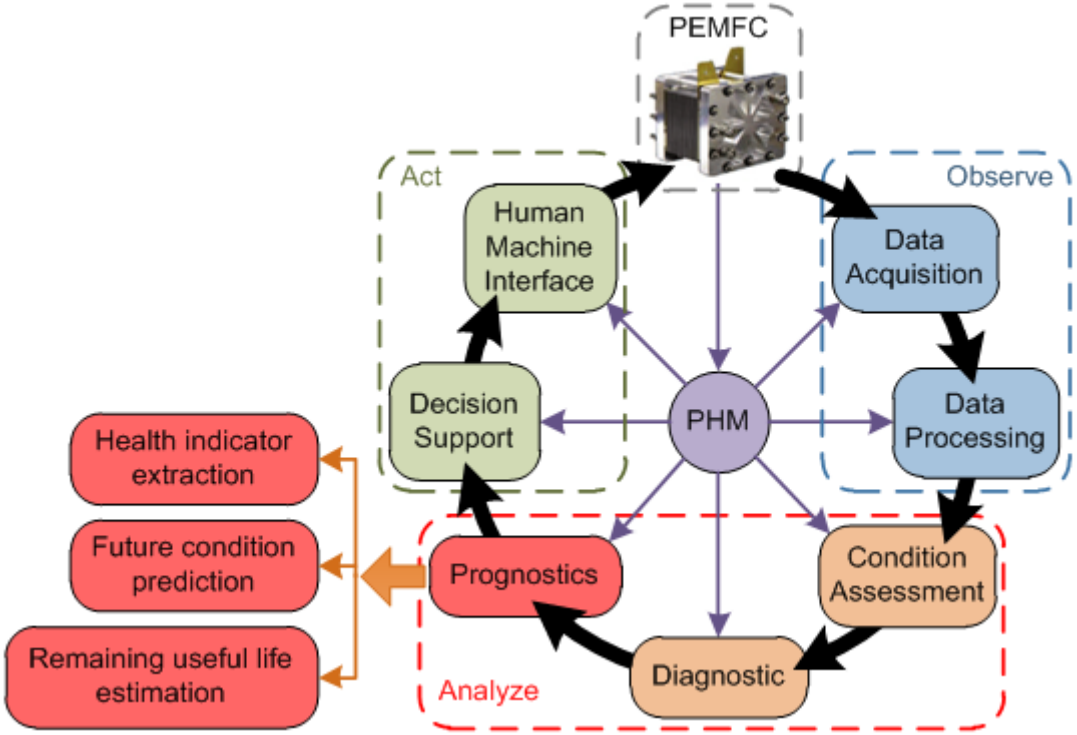

Figure 1.3 Basic architecture of prognostics and health management.

Prognostics and Health Management (PHM) identifies the degradation evolution of engineering equipment, systems and structures. In turn, it predicts potential risks and avoids accidents, ultimately enabling reliable, efficient, economical and safe operation of equipment [25]. In the last decade, PHM technology has flourished and is one of the highly regarded interdisciplinary disciplines in academia and industry. In the fields of aerospace, energy, chemical, transportation, and equipment manufacturing, PHM has gradually become an important driving technology for improving reliability and safety and reducing maintenance costs [26]. For fuel cells, PHM is also one of the promising durability enhancement solutions and has become a hot research topic [27]. The PHM

framework for fuel cells is shown in Figure 1.3, which can be divided into three phases, "Observe", "Analyze", and "Act", and consists of seven steps [28, 29]. By continuously monitoring the fuel cell operation, assessing its State of Health (SoH) based on historical data, diagnosing potential failures, predicting Remaining Useful Life (RUL), and making timely control/maintenance decisions to achieve life extension goals [30].

Prognostics is an important foundation and key support of PHM framework, and its accuracy is related to the timely deployment of control/maintenance decisions, and directly affects the effectiveness of health management. Furthermore, reliable and efficient prognostics is expected to drive the shift from a "scheduled maintenance"-"failure replacement" strategy to a "forecast abnormality"-"condition-based maintenance" strategy. This facilitates to reduce the operation risks and high costs caused by "inadequate maintenance" and "redundant maintenance" [19, 31]. The International Organization for Standardization (ISO) defines prognostics as "analysis of the symptoms of faults to predict future condition and residual life within design parameters" [32]. As a result, the prognostics of PEMFC should cover the following core tasks.

(1) extract Health Indicator (HI) with the capability to characterize the degradation evolution process.
(2) predict future operating conditions and degradation trends.
(3) estimate the remaining useful life.

Under constant load conditions, measurements such as stack voltage can be directly used to assess the degradation evolution of the PEMFC [33-35]. In contrast, under variable load conditions, the frequently changing operating behavior is coupled and superimposed with the inherent degradation evolution of the PEMFC. This contributes to the difficulty of health indicator extraction, the decrease of deterioration trend prediction accuracy/efficiency, and the weakened reliability of remaining life estimation. Therefore, the prognostics issue of PEMFC under variable load conditions is very challenging and needs to be addressed urgently, which is the focus of this dissertation.

1.2. Related work and literature review

Prognostics of fuel cells is an emerging research area in the last decade. In order to comprehensively analyze the current status of PEMFC prognostics research, the relevant research literature are searched in two major databases, Web of Science (WOS) core collection and Scopus, respectively. The search results show that between January 2013 and July 2022, 144 relevant papers are included in the WOS core database and 131 relevant papers are included in the Scopus database. According to the statistics by year of publication as shown in Figure 1.4, the related research work of PEMFC prognostics is gradually attracting wide attention from academia and industry. This section will review and analyze "durability test and health indicator extraction", "degradation condition prediction", and "remaining useful life estimation".

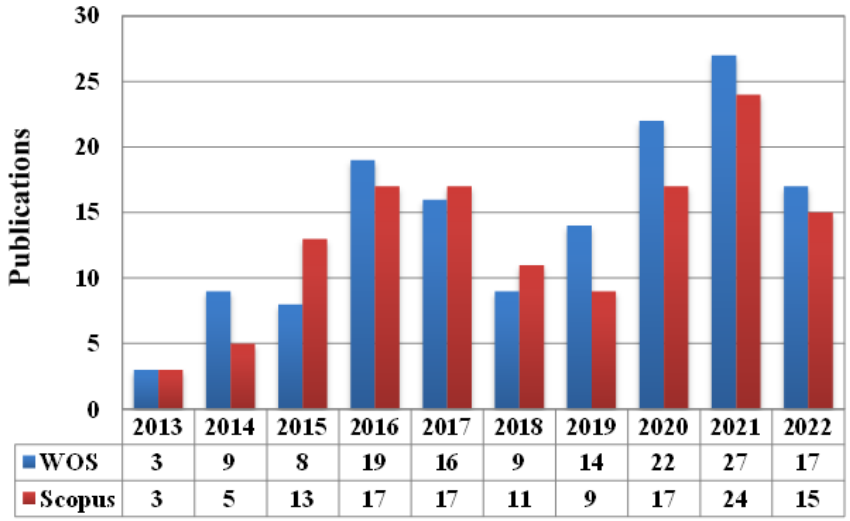

	2013	2014	2015	2016	2017	2018	2019	2020	2021	2022
WOS	3	9	8	19	16	9	14	22	27	17
Scopus	3	5	13	17	17	11	9	17	24	15

Figure 1.4 Literature related to PEMFC prognostics by year of publication.

1.2.1. Long-term durability test

Durability testing is considered as an important tool to analyze the evolution of fuel cell degradation as well as a data base for prognostics. The degradation process of PEMFC involves many time scales from "milliseconds" to "months". Jouin et al. pointed out in the literature [30] that there are different levels of decisions for different time scales, and the time scale corresponding to prognostics should be at least larger than the "hour" level, as shown in Figure 1.5. Generally, the "medium-term prognostics" refer to the prediction time range between one day (24 hours) and one week (168 hours); while the prediction range beyond one week is considered as "long-term prognostics" [11]. The medium and long term prognostics can provide sufficient time for task scheduling optimization and maintenance planning decisions for PEMFC. In view of this, for the medium/long-term prognostics of PEMFC, this dissertation focuses on reviewing the literature with durability test duration longer than 24 hours in the search results.

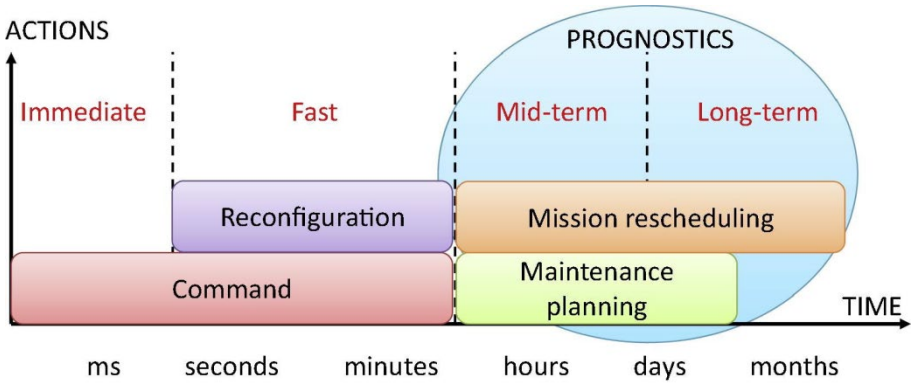

Figure 1.5 Different levels of decision making and association with prognostics [30].

In the long-term prognostics related literature, the involved durability tests can be divided into three categories: constant load condition, quasi-constant load condition and variable load condition.

(1) Constant load condition indicates that the load is always kept constant during the durability test. Specifically, the output current or output power of PEMFC is constant.
(2) Quasi-constant load condition means that the ripple current with fixed amplitude and frequency is superimposed on the current of the constant load condition. To simulate the output behavior of a static converter connected behind the stack.
(3) Variable load condition means that the load current and power show significant changes in a periodic or non-periodic manner during the durability test.

It should be noted that in this dissertation PEMFC performance characterization tests (e.g., polarization curve tests, electrochemical impedance spectroscopy tests, etc.) triggering changes in PEMFC operating parameters are not considered in the variable load category.

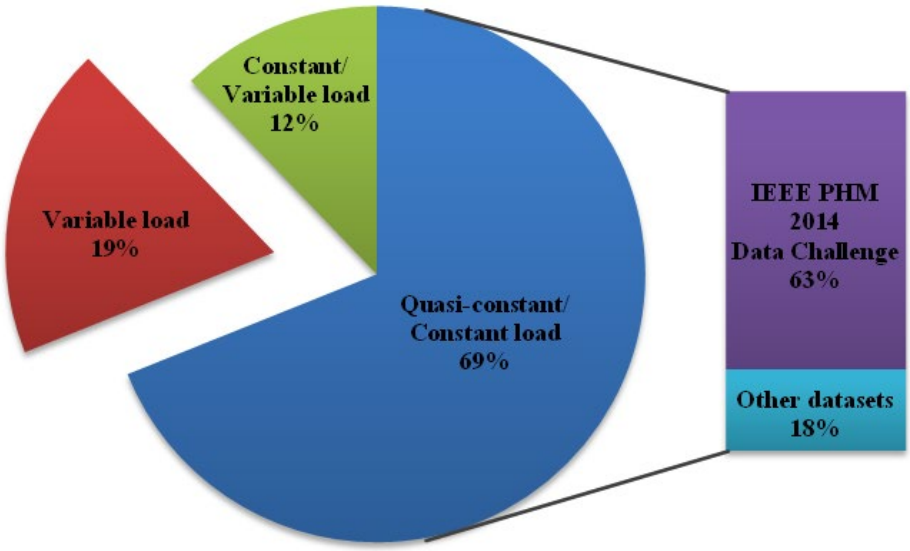

Figure 1.6 Distribution of the types of operating conditions involved in the long-term prognostics related literature.

Compared with the other two operating conditions, the operating behavior and degradation characteristics of PEMFC under quasi-constant load conditions are very close to those under constant load conditions, and the constant load conditions and quasi-constant load conditions are combined in this section to review the literature. Accordingly, the literature related to long-term prognostics is analyzed, and the distribution of various operating conditions is shown in Figure 1.6. Among them, 69% of the literature only conducts research work for constant or quasi-constant load conditions, and 12% of the literature considers long-term prognostics under both constant load conditions and variable load conditions. The durations and corresponding literature for the durability tests under constant/quasi-constant load conditions are shown in Table 1.1. The reported PEMFC stack operation durations ranged from 400 hours10500 hours. The involved minimum current density is 0.08 A/cm^2 [36] and the

maximum current density is 0.8 A/cm² [37]. More than 60% of the research work is centered on the dataset called "IEEE PHM 2014 Data Challenge" [38] (hereinafter referred to as PHM 2014 Challenge). The PHM 2014 Challenge is published by the IEEE Reliability Society, FCLAB, and other scientific institutions. It consists of two durability test data of more than 1000 hours from two PEMFC stacks running in constant load conditions (corresponding to the dataset named FC1) and quasi-constant load conditions (corresponding to the dataset named FC2) [38]. In the literature searched above, all of the work involving quasi-constant load conditions used FC2 aging data from the PHM 2014 Challenge. The total percentage of PEMFC prognostics related research work involving constant/quasi-constant load conditions is over 80%. This seems to result from the fact that the public availability of the PHM 2014 Challenge dataset has greatly contributed to the development of related research. This also coincides with the rapid growth of the relevant literature after 2014 in Figure 1.4.

Test implementer or Stack manufacturer	Duration (hours)	Related literature
PHM 2014 Challenge (Open Source Dataset)	1150 (FC1)	[27, 28, 35, 36, 39-81]
	1000 (FC2)	
Ballard NEXA	400	[36, 47, 50, 82-84]
IEK-14 (High-temperature PEMFC)	1000	[74]
PRAGMA Industries	1700	[77, 85]
ZSW	1750	[27, 41, 86-90]
CEA-LITEN	2000	[91]
Wuhan University of Technology	7000	[37]
Proton Motor 200	10500	[36, 47]

Table 1.1 Long-term durability test under constant load/quasi-constant load conditions.

In different practical applications, the load demand is usually variable. Therefore, it is difficult to fully reveal the degradation behavior of PEMFC by studying the durability tests of constant and quasi-constant loads only. From the statistics in Figure 1.6, less than 20% of the related research works address the long-term prognostics of PEMFC under variable load conditions. This appears to be due to the fact that deploying long-term durability testing under variable load conditions is more challenging. For instance, PEMFCs in transportation applications may have more frequent load changes when dealing with very different road conditions and driving styles. Although accelerated lifetime tests allow to simulate the degradation evolution of automotive PEMFCs to some extent as well as to significantly reduce costs and improve efficiency. However, for durability tests under variable load conditions the available datasets are still relatively scarce [92]. The duration of the durability tests under variable load conditions and the corresponding literature are shown in Table 1.2. The reported PEMFC stack durations range from 80 to 5000 hours and involve maximum current density variations in the range of 0-1.2A/cm² [93]. The load variation modes included in the literature are as follows.

(1) Standby-constant load cycle;
(2) Shutdown-constant load cycle;
(3) Switching between multiple constant-load operating points;
(4) Different combinations of the above three modes.

Test implementer or Stack manufacturer	Duration (hours)	Related literature
MobyPost	80	[52, 59, 60, 69, 94, 95]
Tongji University	425	[93]
	505	
Fuel Cell Bus (Beijing, China)	280	[14]
Proton Motor 200	450	[36, 72]
CEA-LITEN	1000	[27, 42, 80, 96-99]
	1400	[91]
Wuhan New Energy Co., Ltd (open source dataset)	1008	[100]
SAPPHIRE	1200	[101]
Fuel Cell Bus (Zhangjiagang, China)	1200	[102]
PRAGMA Industries	1500	[85, 103]
H2SYS AIRCELL	5000	[104]

Table 1.2 Long-term durability test under variable load conditions.

In addition, there are individual differences in fuel cells, and the degradation behavior is not entirely consistent even for the same type and/or batch of products. In the durability test, the performance of the fuel cell can be partially recovered after the downtime for maintenance, but it is difficult to recover completely. Furthermore, abnormalities in the operating auxiliary devices such as the gas supply unit and temperature regulation component of the fuel cell can also affect the degradation evolution. It is difficult to guarantee that the stack and peripheral auxiliary equipment operate in the same state in each long-term test. These factors make it difficult to reproduce the long-term durability test of fuel cells. Although the long-term deterioration evolution of PEMFC has some commonalities, stack specificity cannot be ignored. Further, the shortage of durability test data is not conducive to fully investigate the specificity of stack degradation. In summary, the long-term durability tests of fuel cells have the following characteristics.

(1) Durability test is difficult to implement and almost impossible to fully reproduce.
(2) Durability test is inadequate and publicly available dataset is scarce.
(3) PEMFC prognostics is highly dependent on the durability test dataset.

1.2.2. Fuel cell health indicators extraction

The health indicator is proposed to scientifically, accurately and reliably characterize the SoH of the PEMFC. For the PEMFC operating under constant/quasi-constant load conditions, the load current is always the same or fluctuates less. For the PEMFC operating under constant/quasi-constant load conditions, the load current is always the same or fluctuates less. At this case, the measurements of output voltage/power etc. will gradually decrease with the increase of operation time, as shown in Figure 1.7. Therefore, under constant/quasi-constant load conditions, the measured stack voltage/power, etc. is sufficient to indicate the degradation state of the PEMFC. As shown in Table 1.3, most of the related works, directly choose the stack voltage or power as the health indicator for PEMFC under constant/quasi-constant load operating conditions. Besides, scholars are also exploring model-based methods to extract health indicators, which are mostly based on fuel cell degradation mechanism models or empirical models. The health indicators obtained by model-based extraction methods can be divided into two categories.

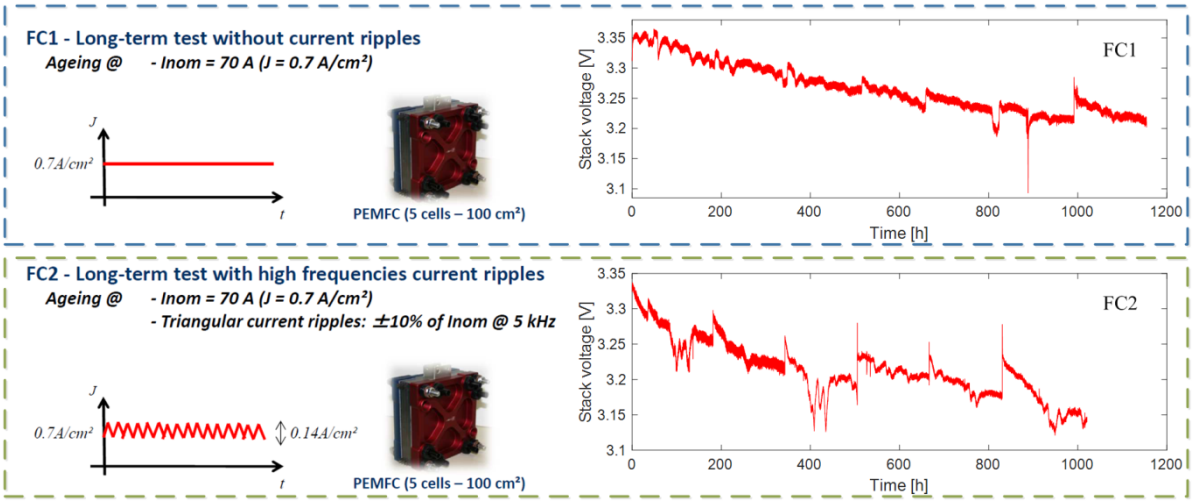

Figure 1.7 Durability test conditions of PHM 2014 challenge: FC1 for constant load; FC2 for quasi-constant load (adapted from [38]).

(1) Certain parameters in the model are used as health indicators.

Such parameters have the ability to reflect the degradation trend or rate, but are not physical quantities per se. In [88], Bressel et al. extracted health indicators related to internal resistance and limiting current (referred to as "aging/degradation factor α" in [88]) by linearly fitting a PEMFC degradation model. Similar health indicators are used by Jha et al. in [42] and Ma et al. in [72].

(2) The physical quantities reconstructed by the model or the fused multi-physical quantities are used as health indicators.

Chen et al. in [44] utilize a degradation model to extract the PEMFC internal resistance and fuse it with voltage and power as a health indicator. In [53], Liu et al. propose multi-scale health indicator based on different

degradation models such as platinum (catalyst) particle radius, electrochemical surface area, and membrane thickness. Jouin et al. in [27] propose a PEMFC degradation model for the health state evolution and use the extracted "reconstructed power" as a health indicator.

Health indicators	Measurements (voltage, power)	Model parameters	Reconstructed physical quantities
Extraction method	None	Model-based	Model-based
Related literature	[28, 35-37, 39-41, 43, 45-52, 54-87, 89-91]	[42, 72, 88]	[27, 44, 53]

Table 1.3 Extraction of health indicators under constant load/quasi-constant load conditions.

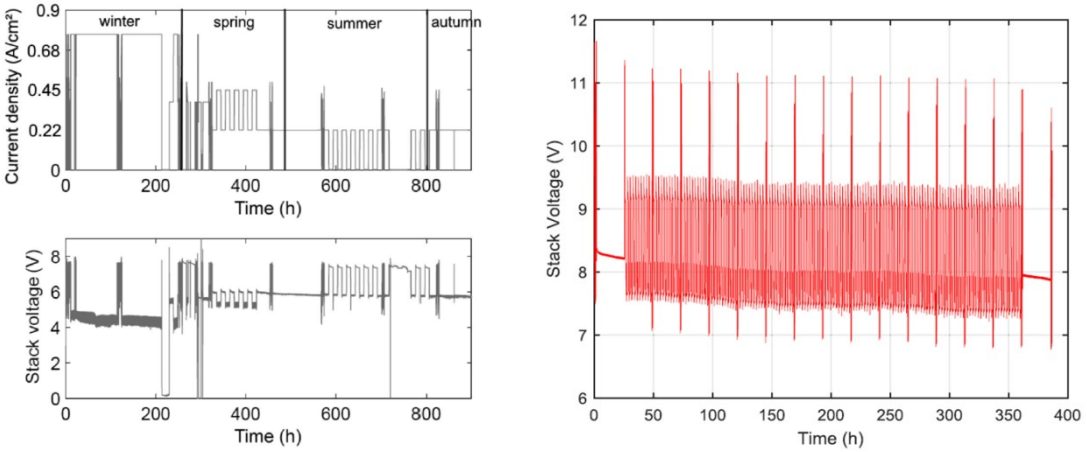

(a) (b)

Figure 1.8 Samples of durability tests of PEMFC under variable load conditions: (a) simulated combined heat and power scenario [96]; (b) simulated load dynamic cycling scenario [72].

Under variable load conditions, the time-varying operating conditions not only affect the transient response performance of the PEMFC, but also result in measurements such as voltage that are no longer suitable as health indicators for direct assessment of degradation behavior [24]. The durability tests of the PEMFC under two variable load conditions are illustrated in Figure 1.8. Among them, Figure 1.8 (a) characterizes the variable load operation of a PEMFC in a micro combined heat and power system for different seasons [96]. While, Figure 1.8(b) is used to simulate the operation with high (100A), medium (70A), and low (20A) load cycles [72]. In comparison with Figure 1.7, under variable load conditions, the PEMFC is not only affected by the inherent degradation evolution, but also by the superimposed time-varying operating conditions and highly dynamic loads. Therefore the stack voltage/power is no longer able to visualize its long-term degradation trend. As in Table 1.4, there are limited studies related to the direct use of measured values as health indicators under variable load

conditions. Mezzi et al. in [101] assume a constant effect of the operating conditions of the PEMFC system. The periodically varying voltage is filtered and used as a health indicator after removing its variable load instantaneous dynamics. However, the assumed conditions somewhat limit its generalizability.

Besides this, most of the research works related to variable load conditions are carried out by extracting new health indicators to replace the measurements. However, dynamic operating conditions and load variations are often operator-dependent and stochastic, making the PEMFC internal parameters (e.g., internal resistance) more complex to estimate. The extracted health indicators can be classified into "model parameters" and "reconstructed physical quantities", and the extraction methods can be classified into model-based and data-based categories.

(1) Model parameters are extracted as health indicators by model-based methods.

Bressel et al. in [96] and Ma et al. in [72] use the extended Kalman filter to estimate the actual SoH and degradation dynamics. In turn, the degradation model parameters are selected as health indicators. Yue et al. employ the multiplicative feature decomposition method in [105], and the same authors use a nonlinear regression method combined with a polarization model in [103] to extract model parameters as health indicators by segmental fitting of the measured voltage.

(2) Reconstructed physical quantities are extracted as health indicators by model-based methods.

In [27] and [30], Jouin et al. discuss the possibility of extracting power or cumulative energy as a PEMFC health indicator based on a polarization curve model under variable load conditions. However, the cumulative energy seems to be plagued with error accumulation. Li et al. use a linear parameter varying model to simulate the dynamics of the PEMFC and extract the virtual steady state voltage as a health indicator [85, 106]. Hua et al. deploy a polarization test at the start of the available lifetime of the PEMFC and propose the relative power-loss rate as a health indicator based on the observed power [98].

(3) Reconstructed physical quantities are directly extracted based on the data as health indicators.

This type of extraction method uses resampling, filtering, etc. to select a certain part of the measured physical quantities as reconstructed health indicators. Some operating condition is cyclic switching between nominal power operating point and shutdown. For this case, Vichard et al. in [104] remove the data corresponding to the shutdown operating condition from the stack voltage. In turn, the reconstructed voltage is used as a health indicator. The same approach is used by Chen et al. in [52, 59, 60, 69, 94, 95]. The variable load conditions mentioned by Ou et al. in [93] and Zuo et al. in [100] involve more voltage operating points. The authors selected a certain load current and extracted its corresponding stack voltage by a

resampling-like approach. The virtual constant-load voltage reconstructed accordingly is used as a health indicator.

Health indicators	Measurements (voltage)	Model parameters	Reconstructed physical quantities	
Extraction method	None	Model-based	Model-based	Data-based
Related literature	[101]	[72, 96, 102, 103]	[14, 27, 30, 72, 80, 85, 98, 99, 102]	[52, 59, 60, 69, 93-95, 100, 104]

Table 1.4 Extraction of health indicators under variable load conditions.

In summary, for constant/quasi-constant load conditions, it is well accepted to use measurements such as voltage/power as the health indicator. For variable load conditions, the measurements with superimposed operational behavior are no longer suitable as health indicators. Extracting reliable and physically interpretable health indicators from the effects of complex operating conditions and frequent load switching remains extremely challenging. Most of the related methods that have been proposed by scholars suffer from: requiring additional downtime testing of the PEMFC, difficulty in tracking the load change transient dynamics, and high computational cost. As a result, how to extract a suitable health indicator for characterizing the degradation evolution is the core task for the long-term prognostics of PEMFC under variable load conditions.

1.2.3. Fuel cell degradation condition prediction and RUL estimation

The ultimate goal of prognostics is to predict the future conditions and lifetime of the fuel cell. Among them, the future condition, also known as the future degradation condition, mainly includes the short-term operational behavior and long-term degradation trend associated with the fuel cell performance decrease. In the model training phase, the prediction model is trained using historical health indicator data. While updating the model in the prediction phase, different models rely on future operational monitoring data to different extents. Accordingly, the prediction modes can be classified into two categories: single-step and multi-step prediction.

(1) Single-step prediction mode.

During the prediction process, fuel cell operation data are required continuously to update the well-trained prediction model, as shown in Figure 1.9. This mode is suitable for tracking short-term degradation behavior and has a strong ability to portray the detailed changes of health indicators. It is conducive to identifying short-term abnormalities and can provide support for real-time fuel cell control and operation monitoring. Nevertheless, it is difficult to be used for remaining useful life prediction

because of its strong dependence on real-time operation data and short prediction range (typically less than 1 day).

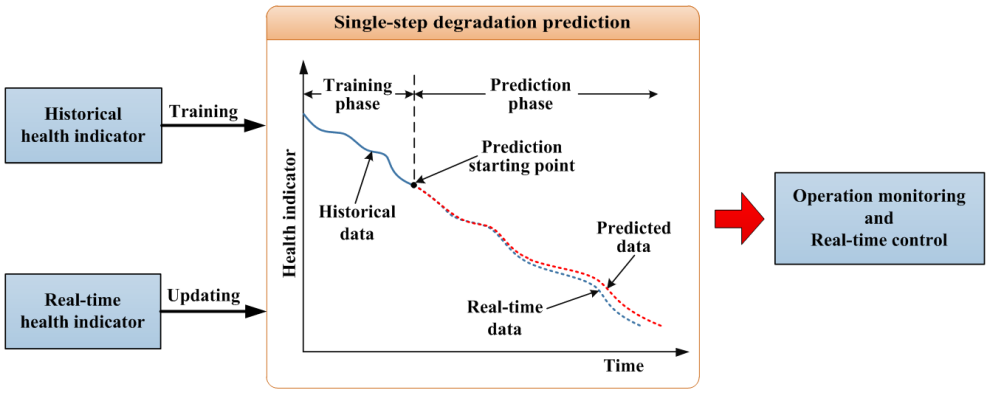

Figure 1.9 Single-step degradation prediction mode.

(2) Multi-step prediction mode.

Multi-step prediction is usually built on a single-step prediction, and the model is updated using the predicted data from the previous step to achieve continuous prediction iteratively, as shown in Figure 1.10. This mode is designed to predict future long-term degradation trends over a prediction range of tens to hundreds of hours, which in turn allows for the remaining useful life estimation by setting a failure threshold. It does not rely on real-time operational data during the prediction phase. Nevertheless, updating the model using only the predicted data has the potential to accumulate errors, which results in the prediction accuracy decreasing as the prediction range increases.

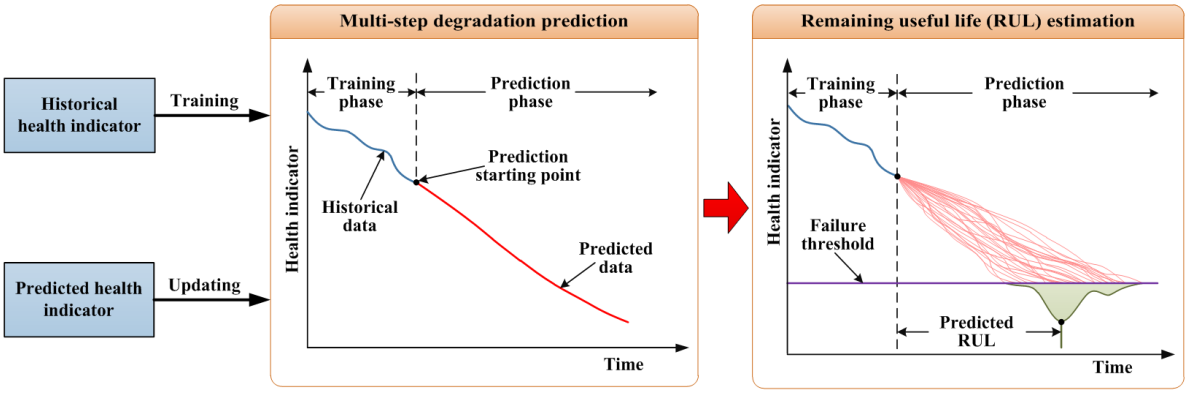

Figure 1.10 Multi-step degradation prediction and remaining useful life prediction.

Accordingly, this dissertation reviews the literature related to PEMFC long-term prognostics. The distribution share of each type of prediction model in the searched literature is shown in Figure 1.11. Among them, the percentage of literature focusing only on the identification and extraction of health indicators (without performing the prediction task) is 4%. Approaches involving single-step degradation prediction account for about 46% of the literature, and almost none of them estimate the RUL due to the limitation of the prediction range. About half of the literature used multi-step

degradation prediction mode, and most of these estimated RUL. From the distribution of the literature, single-step degradation prediction and multi-step degradation prediction receive comparable attention. While more scholars prefer to achieve RUL prediction in multi-step degradation prediction. For variable-load conditions, the degradation evolution of PEMFC is coupled with the operational behavior, which makes predicting both long-term degradation trends and RULs very challenging. Several scholars have attempted to deploy single-step degradation prediction under variable load conditions [95, 100, 101], achieving high accuracy prediction in a shorter range, which would support real-time detection and operational control of fuel cells [107]. In contrast, the multi-step degradation prediction mode provides a longer prediction range and calculates the RUL at a preset failure threshold. Furthermore, by improving the prediction accuracy and extending the prediction range, it will facilitate the development of maintenance plans to provide sufficient time for avoiding fatal failures [11].

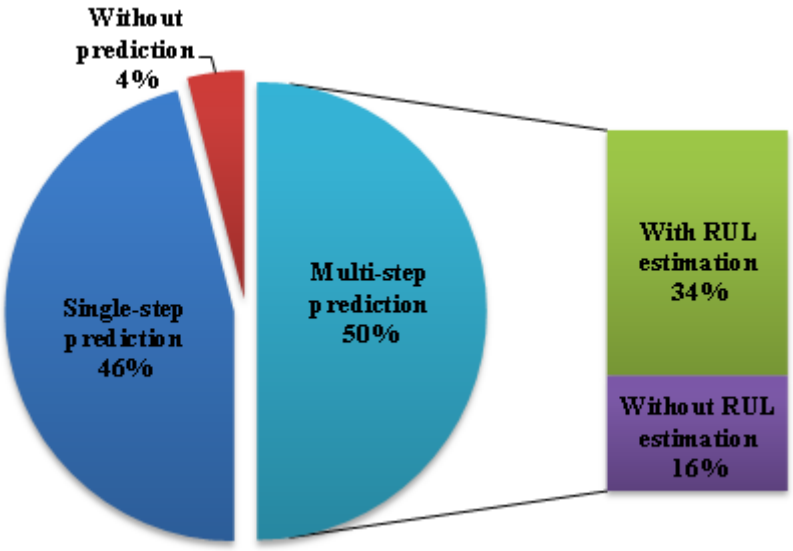

Figure 1.11 Distribution of literature involved in degradation prediction and remaining useful life (RUL) estimation.

Besides, common prediction methods involved in prognostics can be divided into three categories: data-driven, model-driven, and hybrid methods [19]. Among them, the model-driven method describes the degradation process by constructing physical models of the fuel cell. In cases where the physical degradation model is accurate enough, this type of method is beneficial to improve the prediction accuracy. Hu et al. propose a reconstructed prediction method for fuel cell city buses in [14]. By analyzing different operating conditions of the city bus, a fuel cell stack voltage degradation model is constructed. However, in that work only short-term predictions (less than one hour) are analyzed and do not estimate the RUL. The authors of the literature [108], Liu et al. propose a PEMFC prognostics model based on an adaptive unscented Kalman filter. Currently, most scholars seem to believe that the fuel cell degradation process is very complex and its degradation mechanism has not been fully revealed, making it difficult

to build a physical degradation model with sufficient fidelity. Moreover, purely model-driven methods are often accompanied by strong assumptions for fuel cell parameters, leading to limited model generalization performance.

Data-driven (e.g., [34, 36, 41, 65, 101]) and hybrid methods (e.g., [27, 28, 30, 33, 48, 54, 101]) have attracted more widespread attention than model-driven methods. This is due to the ability of these methods to proficiently learn and predict trend characteristics of health indicators [10, 31]. In the literature [41], Javed et al. propose an algorithm based on summation wavelet extreme learning machine which is capable of long-term degradation trend prediction and RUL estimation. It is worth mentioning that the robustness and adaptability of the prediction methods are discussed in that work, which has become one of the thorny issues faced by most prognostic methods. In [28], Jouin et al. propose a hybrid method based on particle filter framework and degradation behavior model , it also estimates the RUL.

Inspired by the remarkable recent advances in Deep Neural Network (DNN), scholars have paid particular attention to the development of data-driven prediction tools by configuring and training different DNN structures. The literature [62, 85, 106] uses the Echo State Network (ESN) framework for prediction. Among them, Li et al. in [85, 106] conducted long-term aging experiments on a compact fuel cell system and used the Linear Parameter Varying (LPV) model to extract the virtual steady-state voltage of the fuel cell under variable load conditions and further used the ESN to predict the degradation trend of the voltage and estimate the RUL. Similar to the literature [28], the method focuses more on the long-term variation trend rather than capturing local details.

Among the data-driven methods in the DNN framework, the prediction models based on Long Short-term Memory (LSTM) networks possess powerful time series processing capabilities. Therefore, PEMFC prognostics methods applying LSTM networks have received much attention in recent years [34, 36, 65]. Nevertheless, the training and learning of classical LSTM models strongly depend on historical data (training set). To achieve accurate prediction beyond the training data value scale then becomes a difficult task [109]. Meanwhile, to enable RUL estimation, multi-step degradation prediction with long prediction ranges typically needs to be deployed. However, the performance of the classical LSTM becomes unsatisfactory with the extension of the prediction range in the multi-step degradation prediction mode. Interestingly, the reason for this phenomenon may be due to the powerful "memory" ability of the LSTM itself, which incorrectly records irrelevant features in the training set. To cope with this issue, Ma et al. in [33] propose a hybrid model consisting of an Autoregressive Integrated Moving Average (ARIMA) model combined with the LSTM. Overall, LSTM network-based prediction models still need improvement in long-term prediction cases, while related studies are extremely limited.

As a summary of the above, among the two prognostics modes, single-step and multi-step prediction have their own focus in different demand scenarios. Limited by the unknown future operation monitoring data, the multi-step prediction mode is more

susceptible to cumulative errors, making it more difficult to predict. On the other hand, among the three types of prognostics methods.

(1) model-driven methods exhibit high prediction accuracy, but are complex in configuration and inadequate in generalization performance.
(2) Data-driven methods do not require the acquisition of a priori physical knowledge, are efficient, and possess favorable transferability. However, the prediction accuracy is easily constrained by the size of the training set data.
(3) Hybrid methods combine the advantages of physical models and data-driven methods, but also tend to merge the shortcomings of both.

Moreover, there are very limited studies related to the failure threshold and evaluation criteria in RUL estimation. Therefore, the core challenges that need to be addressed in fuel cell degradation condition prediction and remaining useful life prediction can be summarized as follows: improving the prediction accuracy under multi-step prediction mode, enhancing the shortcomings of prediction methods, and providing reasonable RUL evaluation criteria.

1.3. Dissertation organization structure

The remainder of the dissertation is organized as follows.

Chapter 2 introduces the basic concepts, performance indicators, and characterization of fuel cells. Specifically, the development of fuel cells is briefly introduced, and the basic principles of fuel cell are given. Furthermore, a detailed description of how to measure the fuel cell global performance using the "Current density-Voltage" (C-V) curve is presented. Then, four on-site characterization methods commonly used for fuel cells are provided. It concludes with a discussion of the challenges posed by variable load conditions, the inadequacy of characterization methods, and the necessity of deep learning-based prognostics.

Chapter 3 presents a prognostics strategy based on the fusion of a statistical approach and a deep learning model. Specifically, an Autoregressive Integrated Moving Average Model with Exogenous Variables (ARIMAX) is used to generate navigation sequences and to navigate the LSTM network model during prediction. The proposed prognostics strategy is able to optimize multi-step prediction for long-term degradation trends and RUL.

Chapter 4 proposes an electrochemical mechanism-based model for extracting fuel cell HI under dynamic mission profiles. In addition, the historical operational data are processed using the Adaptive Brownian Bridge-based Aggregation (ABBA) method to further extract the inherent degradation feature information in HI via compression and dimensionality reduction. The processed symbolic sequences are used to improve the long-term prediction performance of the LSTM.

Chapter 5 suggests a data-driven prognostics approach based on time-frequency analysis and symbolic-based Gated Recurrent Unit (GRU). A modified Hilbert-Huang Transform (HHT) method is used to extract HI from historical operational data. Subsequently, symbolic-based GRU is used for long-term degradation condition

prediction and RUL estimation. Finally, the hybrid prognostics performance is evaluated multiple times over the interval of possible failure thresholds, instead of using only a single failure threshold. The approach allows for an effective reduction in computational costs.

Eventually, the main contributions and potential future research aspects of this dissertation are summarized and discussed in Chapter 6.

2. Preliminary

2.1. History of fuel cells

Fuel cells are generally considered to be devices that convert the chemical energy contained in fuels and oxidizers into electrical energy through chemical reactions. Recently, the term fuel cell seems to be used specifically to describe a reactor that uses hydrogen as a fuel. Hydrogen has been used as a fuel for automobiles for a long history. For instance, hydrogen was used as a fuel in internal combustion engines 200 years ago, similar to how fuels such as gasoline work in internal combustion engines today. Nevertheless, at that time, hydrogen was subject to many technical limitations in terms of production, storage and transfer compared to gasoline. Therefore, hydrogen has not shown superiority as a fuel for internal combustion engines.

A simple history timeline of the fuel cell is shown in Figure 2.1. In 1839, the German-Swiss chemist Christian Friedrich Schönbein first publishes the principle of the fuel cell in the Philosophical Magazine. Three years later, British physicist William Robert Grove develops the first fuel cell, also known as the gas voltaic battery. In 1958, General Electric Company, invents the platinum-deposited ion exchange membrane. The fuel cell improved by this technology is considered the first PEMFC, also known as the Grubb-Niedrach fuel cell. In 1965, NASA replaces chemical cells with fuel cells in Project Gemini, which is the first commercial application of fuel cells. Thanks to fuel cells that can generate enough electricity to power longer missions, the Gemini V completes more than a week of manned space flight. Furthermore, PEMFC produces water during the power generation process, which is expected to contribute to the astronauts' drinking water storage expansion. In 1966, General Motors presentes the world's first fuel cell automobile, named Electrovan.

After the 1970s, the energy crisis prompts an accelerated consideration of alternatives to fossil fuels. As a result, hydrogen fuel cells are also gaining new opportunities for development. In addition, fuel cells also show advantages in some special cases, such as in the military, where Siemens AG of Germany designs a fuel cell-based air-independent propulsion system and applies it to the Type 212 submarine in 1998. Especially, unlike internal combustion engines, fuel cell stacks do not contain reciprocating mechanical structures. As a result, it operates at a lower noise level, which is conducive to the submarine's survivability.

As we enter the 21st century, the development of fuel cells applied to electric vehicles is attracting much attention. In 2015, Toyota launches Mirai, the first mass-produced fuel cell electric vehicle. In 2018, Hyundai presentes its crossover SUV powered by fuel cells, called NEXO. Two years later, Toyota launches the second generation Mirai with a range being updated to over 647 km.

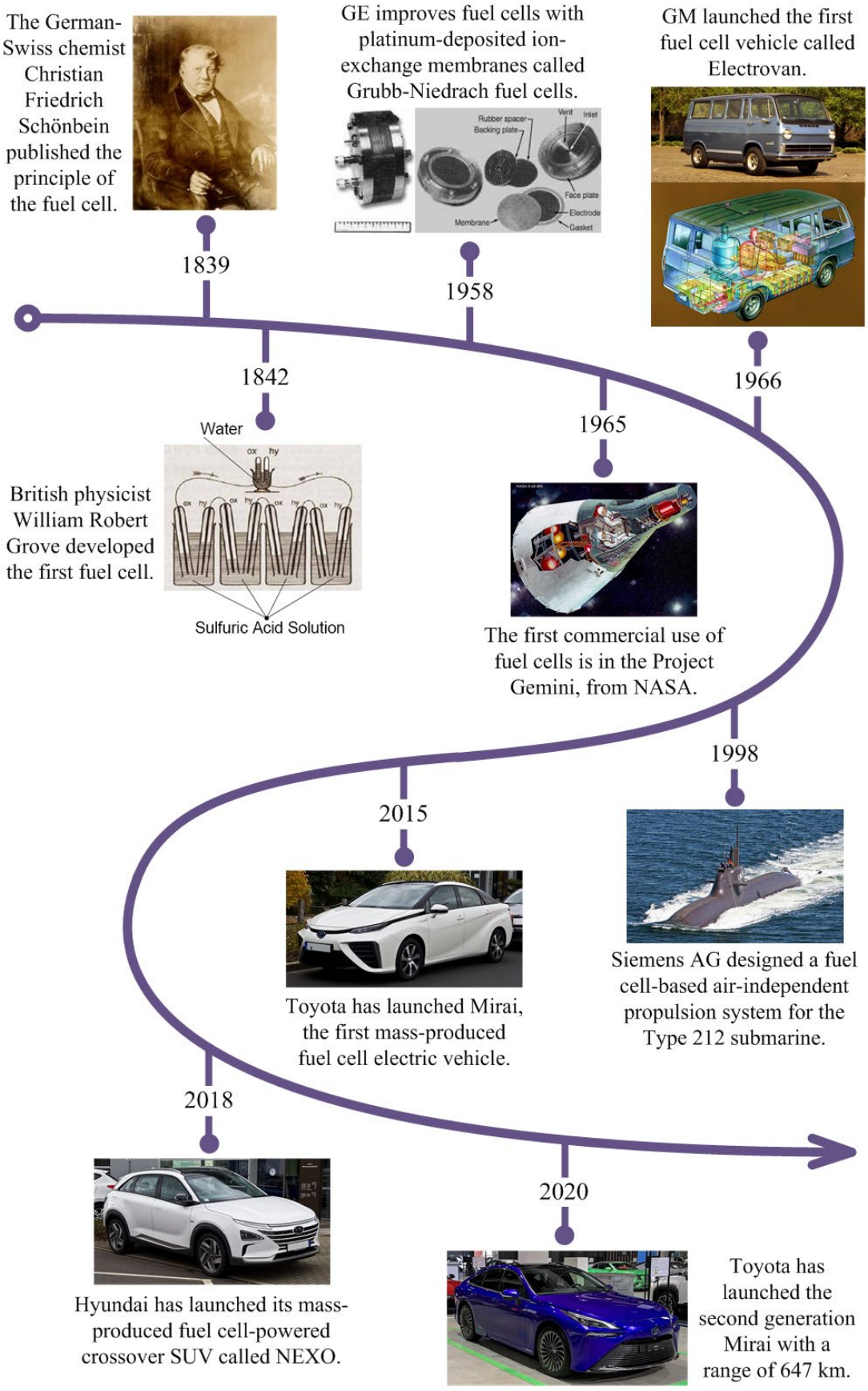

Figure 2.1 History of fuel cell development.

2.2. Basic principle of fuel cell

Hydrogen releases energy when it undergoes an oxidation reaction. A simple and direct way is "combustion", as in the following reaction equation.

$$2H_2 + O_2 \rightarrow 2H_2O \tag{2.1}$$

This "combustion" is rapid and violent, releasing a large amount of "heat energy". If we want to obtain electrical energy, it is required to convert thermal energy into mechanical energy first, and then mechanical energy into electrical energy. This is similar to driving a generator set with an internal combustion engine, which involves a complex energy conversion process and can easily lead to undesirable energy losses.

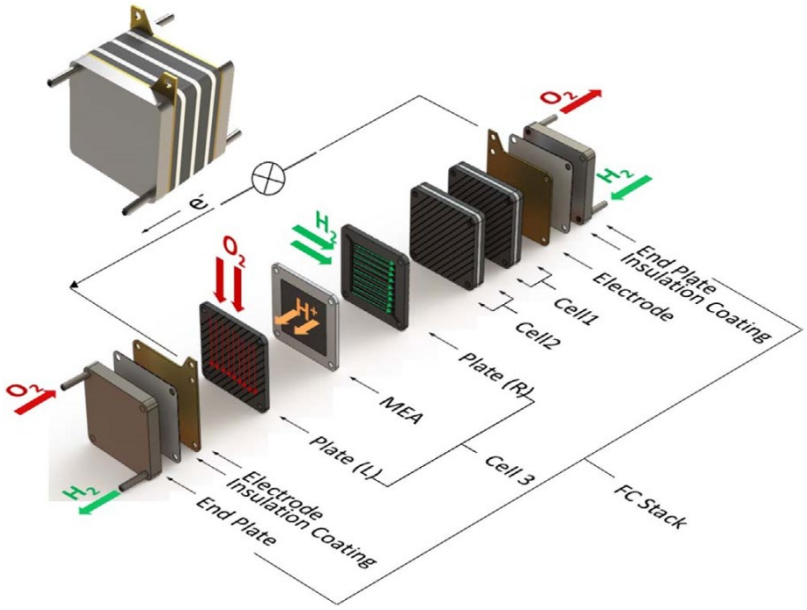

Figure 2.2 Structure diagram of fuel cell stack and components [19].

In contrast, in the current fuel cell technology, hydrogen is not burned directly, but is converted to electricity by reacting with oxygen. To achieve this process, an electrolyte is required to spatially isolate the fuel from the oxidizer. In fact, the electrolyte allows the passage of ions while blocking electrons. Figure 2.2 shows the structure diagram of the fuel cell components, single cells and stacks. A cathode and anode are installed on the left and right sides of the electrolyte, respectively. In this case, the anode (right) side is fed with hydrogen gas, which is then ionized into hydrogen ions (or protons) and electrons, as in the following equation.

$$H_2 \rightarrow 2H^+ + 2e^- \tag{2.2}$$

Subsequently, hydrogen ions will transfer to the cathode through the electrolyte. And electrons flow through the circuit to drive the load (e.g. motor), after which they also arrive at the cathode. At the same time, the following reaction occurs with the cathode side being fed with oxygen (or air).

$$\frac{1}{2}O_2 + 2e^- + 2H^+ \rightarrow H_2O \tag{2.3}$$

The oxidation reaction that occurs here seems to be similar to the "combustion" in equation (2.1). The main difference is that the reaction process in the fuel cell involves the flow of electrons and directly generates an electric current. Meanwhile, less "heat energy" is released.

2.3. Performance of fuel cell

The fuel cell output current is directly proportional to the hydrogen consumption. If the fuel supply and output current are kept fixed, when the output voltage drops, the electrical power produced by the fuel cell also falls. Therefore, the output voltage can be used to measure the efficiency and performance of the fuel cell. Based on this, how to obtain a high output voltage under high current load is significant for the power increase of fuel cells. To achieve this goal, however, is undoubtedly challenging. This is due to the fact that fuel cells, like other power generation devices, are accompanied by power losses when generating electricity. Moreover, this power loss will vary depending on the load current level.

One possible way to better quantify the fuel cell performance is to utilize a "Current density-Voltage" (C-V) curve. It is worth noting that "current density" is used here instead of "current". This is because the reaction interface area (electrolyte surface area) varies greatly from one scale of fuel cell to another, even leading to order of magnitude differences in output current. In order to get more appropriate performance measurements, it is necessary to normalize the current based on surface area. Figure 2.3 shows the C-V curves for a single cell of a hypothetical low-temperature PEMFC, containing six curves in total.

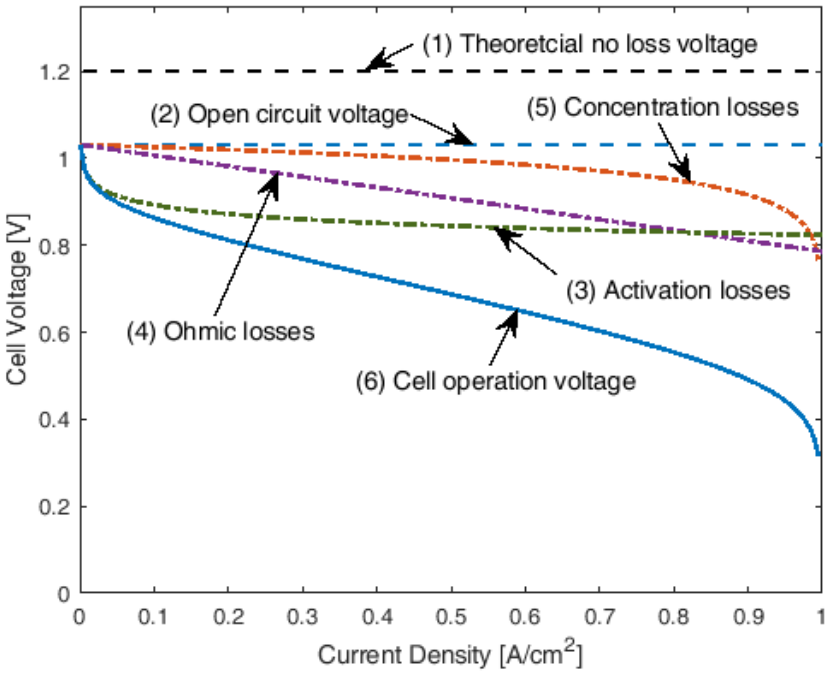

Figure 2.3 Voltage drops of fuel cell.

(1) Theoretical voltage of fuel cell

Ideally, the voltage value is obtained by theoretical (thermodynamics) calculation , which is considered as "no loss". In addition, it seems to be very difficult to obtain the theoretical voltage by practical measurement.

(2) Open-circuit voltage of fuel cell

Obviously, in this case the open-circuit voltage is lower than the theoretical voltage. One possible explanation is due to the internal current, which flows in the opposite direction to the load current. The electrolyte may allow a very few electrons to pass through, or the fuel (hydrogen) may flow abnormally to the cathode, both of which may trigger internal currents. In addition, the open-circuit voltage can be physically measured.

(3) Voltage drop due to activation losses

Activation losses are caused by electrochemical reaction kinetics. Some energy is inevitably consumed during the start-up of the fuel cell, which is specifically reflected in the drop of output voltage. Actually, the activation losses, which are the most important reason for the irreversibility and voltage drop of low temperature fuel cells, occur mainly at the cathode. It is observed that the "activation losses" curve in Figure 2.3 drops rapidly at the initial stage, and then the voltage drop behavior becomes gradually moderated with the increase of the load current. This curve can be expressed by the following equation.

$$E_{act} = E_{rev} - V_{act} \tag{2.4}$$

Where, E_{act} is the operation voltage of the fuel cell when only the activation losses are considered, E_{rev} is the open-circuit voltage of the fuel cell, and V_{act} represents the voltage drop triggered by the activation losses.

(4) Voltage drop due to Ohmic losses

Ohmic losses are voltage drops caused by the resistance existing in the electrodes and electrolyte. As shown in Figure 2.3, the "Ohmic losses" curve demonstrates the linear drop in output voltage that accompanies the increase in current load. This can be calculated using the following equation.

$$E_r = E_{rev} - V_r \tag{2.5}$$

Where, E_r is the operating voltage of the fuel cell when only Ohmic losses are considered, and V_r represents the voltage drop induced by Ohmic losses.

(5) Voltage drop due to concentration losses

When the fuel (and/or oxidizer) is supplied in gaseous form, the hydrogen (or oxygen) at the electrodes is drawn off by the operating fuel cell, causing a slight reduction in gas concentration. This triggers a drop in the fuel cell output voltage, called the concentration losses (also known as mass transfer losses). Obviously, the higher the load current is, the greater will be the effect of such concentration losses, as shown in Figure 2.3. The

operating voltage E_{conc} considering only the concentration losses can be calculated as follows.

$$E_{conc} = E_{rev} - V_{conc} \tag{2.6}$$

Where, V_{conc} represents the voltage drop triggered by the concentration losses. It shows a rapid drop in the high current density region, in contrast to the insignificant drop at low current loads.

(6) Operation voltage of fuel cell

Practically, the fuel cell output voltage takes into account the effects of activation, Ohmic, and concentration losses at the same time. The actual (single cell) operation voltage (E_{cell}) calculation equation is as follow.

$$E_{cell} = E_{rev} - V_{act} - V_r - V_{conc} \tag{2.7}$$

The trend of the operation voltage also inherits the characteristics of these three losses, dropping rapidly at the beginning (mainly activation losses), then showing a similar linear fall (mainly Ohmic losses), and finally dropping rapidly again at high load currents (mainly concentration losses).

In summary, the performance of the fuel cell can be regarded as the ability to sustain the output voltage under the premise that the load current meets the demand setting. For fuel cells, the actual output voltage is generally lower than the theoretical voltage, even if the open-circuit voltage is also the case. Once a fuel cell starts to operate, the operation voltage drops with the increase of load current due to the combined effect of several factors. As a result, it becomes more challenging to evaluate the fuel cell performance under variable load conditions.

2.4. Characterization of fuel cell

Characterization is a way to portray the performance of fuel cells in different dimensions by experimental measurements. Even the SoH degradation evolution of fuel cells can be revealed by continuous characterization tests. It is undeniable that the performance losses caused by different components of a fuel cell are also very various. Performance evaluation at the component level of a fuel cell is usually based on an off-site characterization model. The off-site model is interested in the physical structure (e.g., catalyst surface area, porosity, permeability, and even microstructure) , as well as the chemical properties, of the components. This does allow for a deeper exploration of the fact that fuel cell performance is degraded. However, the off-site mode usually requires the fuel cell to be shut down and the components to be disassembled for testing. In this case, the characterization has to ignore the effects of actual operation conditions, even accompanied by destructive testing of the components. Moreover, these components will incur additional performance losses upon integration. Therefore, it is essential to deploy stack (and/or system) level characterization of fuel cells under actual operation conditions.

In contrast, the on-site Characterization model aims to quantify the performance of the fuel cell under actual operation conditions. On-site mode focuses on time-dependent

electrochemical variables (e.g., voltage, current, etc.), and is therefore also referred to as Electrochemical Characterization. Four common types of on-site characterization are as follows.

(1) Polarization curve method

As described in Section 2.3, current density-voltage curve (also called polarization curve) can quantify the overall performance of a fuel cell. In this case, obtaining polarization curves from experimental measurements is one of the on-site characterization methods. It should be noted that the polarization curve measurement is based on the premise that the fuel cell is kept in steady-state operation. Recalling Figure 2.3, it is easy to see that the current densities involved in the polarization curves are diverse. Typically, it is sufficient to plot the polarization curve by measuring the operation voltage at 10 to 20 different load currents. The polarization curve test needs to last for several or even tens of hours.

(2) Current interrupt method

When switching between two different load currents, the operation voltage of the fuel cell is slow to reach the new steady state, as shown in Figure 2.4. This is due to the fact that a change in load will inevitably affect the reactant concentration and stack temperature. The fuel cell needs time to reach a new balance. Briefly, the current interrupt method is used to record the duration it takes for the operation voltage to regain steady state. The transient change in voltage is generally considered to correspond to the Ohmic losses of the fuel cell, while the slowly changing part corresponds to the non-Ohmic losses. The current interrupt method is a fast characterization oriented to dynamic performance evaluation. It can be easily deployed whenever load switching exists.

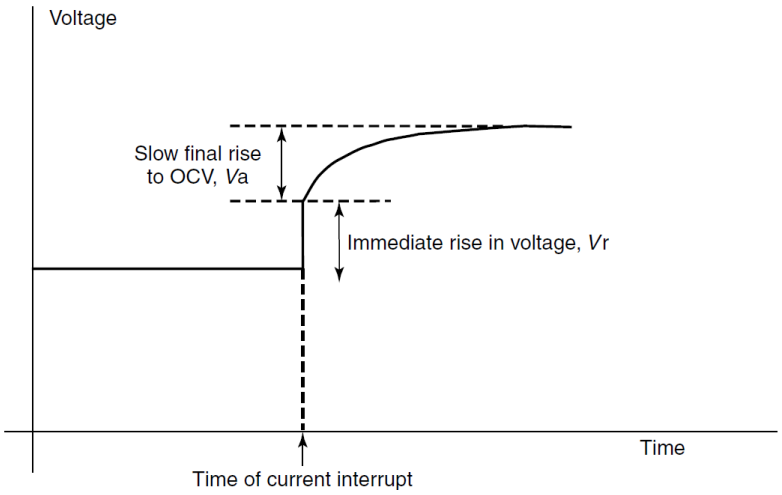

Figure 2.4 Voltage against time for a fuel cell after a current interrupt [110].

(3) Cyclic voltammetry

Cyclic voltammetry (CV) is designed to characterize the performance of fuel cell catalysts, such as Electrochemcial Active Surface Area (ECSA).

Specifically, the operation voltage of the fuel cell is linearly scanned between two preset voltage values repeatedly. The corresponding current density change is recorded and the resulting curve is shown in Figure 2.5. Repeated voltage scans make the CV test time consuming. In addition, the fuel cell needs to be specially configured, for instance to provide extra types of test gases.

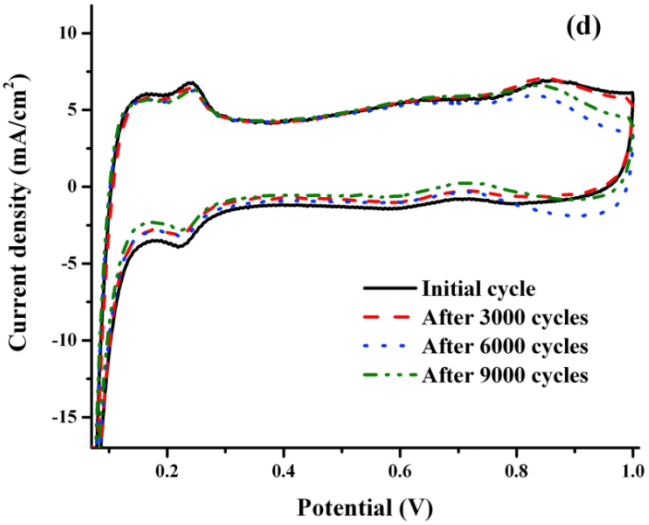

Figure 2.5 A cyclic voltammetry sample [111].

(4) lectrochemical impedance spectroscopy

Electrochemical Impedance Spectroscopy (EIS) is the behavior of superimposing a small amplitude sinusoidal interference signal on the operation voltage and observing the current response. In turn, Nyquist plots are drawn to characterize the impedance characteristics of the fuel cell, as in Figure 2.6.

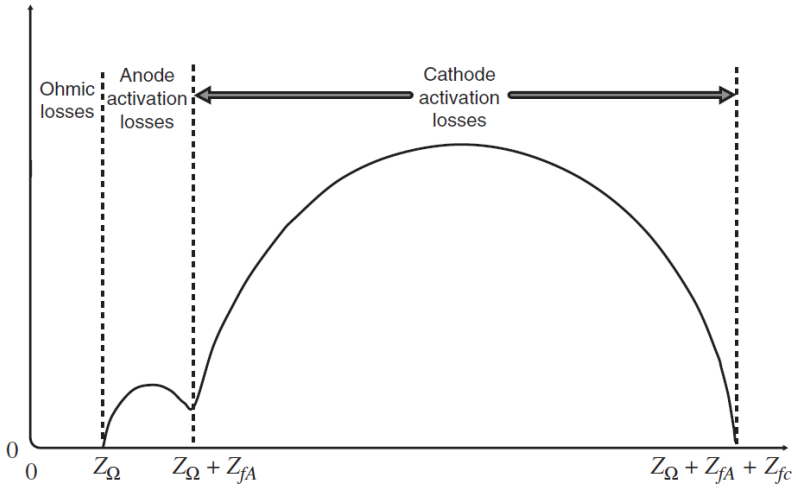

Figure 2.6 Example Nyquist plot from a hypothetical fuel cell.[112].

In fact, combined with the assumption of equivalent circuits, EIS facilitates the independent characterization of the three voltage losses mentioned in Section 2.3. However, impedance measurements need to be performed at

dozens of different frequencies, hence the EIS is also time-consuming. In addition, the assumed equivalent circuit may be complex in order to fit the measurement results as accurately as possible.

In summary, the off-site characterization of fuel cells focuses on component level, or even deeper, performance quantification. While it can reveal some degradation facts, it is also accompanied by stack shutdown or component damage. At the same time, the off-site mode inevitably lacks comprehensive consideration of inter-component integration, actual operation conditions, and other factors. Comparatively, on-site methods are able to characterize the performance of well-integrated fuel cells. Nevertheless, it also suffers, to varying degrees, from being time-consuming, complex, and requiring extra configuration.

2.5. Discussion

In this chapter, the history, fundamentals, performance and characterization of fuel cells are reviewed. Specifically, for factors affecting the operating voltage, it is closely related to the magnitude and variability of the load or not. Under variable load conditions, fuel cells suffer from switching and superposition of different components of overpotential. This makes it exceptionally difficult to identify these overpotential components. On the other hand, most of the different characterization methods interfere with the fuel cell operation. For instance, it requires shutdown or running at a specific load current to achieve performance tests. This is not only inconvenient, but also tends to cause additional damage to the fuel cell. Further, it is doubtful whether the characterization results obtained in isolation from the actual operating operation can represent the true performance of the fuel cell. Moreover, the characterization techniques mentioned above cannot explain the deterioration of fuel cells at a deeper level. The degradation process of the platinum catalyst particles in the core components of the fuel cell, e.g., the membrane electrode assembly, is difficult to observe online.

In conclusion, the degradation process of fuel cells is complex and becomes more difficult to be identified under the influence of variable loads. It is important to seek a performance evaluation method that does not rely on characterization techniques, or does not require shutdowns and additional testing procedures. With this in mind, this thesis will be devoted to the evaluation of fuel cell performance, especially long-term degradation behavior and remaining lifetime, using deep learning-based methods.

3. Fusion prognostics strategy based on statistical method and deep learning

3.1. Introduction

In order to better understand the degradation mechanisms of PEMFC, and shorten the time/cost of durability tests, it is essential to estimate the degradation trend and RUL as accurately as possible. It has been widely known that the FC degradation process is complicated and complex. It is usually difficult to establish an analytical degradation model with sufficient fidelity. Data-based methods and hybrid methods have therefore been attracting wider attention compared with model-based ones.

Recently, long short-term memory, a Recurrent Neural Network (RNN) paradigm, has been considered as a potentially effective tool to handle time series prediction problems. In most cases, based on raw LSTM, the degradation trend can be effectively predicted only for a short horizon of a few hours. To achieve RUL estimation, multi-step prediction with long prediction horizon is required, particularly for the prognostics of aging degradation. However, several issues arise as the prediction horizon is extended.

(1) The prediction error is accumulated when well-trained LSTM models are fed with the output in previous-step prediction iteratively.
(2) The FC degradation behavior is disturbed and influenced by the time-varying operations and recoverable faults, which poses difficulties for tracing the intrinsic degradation trend.
(3) The prognostic models built only on the historical data usually suffer from the model epistemic uncertainty. The predicted results are hardly beyond the numerical interval of the historical-based training set.

This Chapter is devoted to tackling the afore-mentioned issues and make LSTM model more appropriate for long-term prognostic use. Basically, the above issues are due to the lack of reliable data or information in the prediction zone. As one potential solution, an approximate trend sequence, inherited from the training data, can be pre-generated for the prediction zone. The pre-generated sequence can then be used to guide the LSTM model in order to avoid the afore-mentioned undesired predictive behaviors. Specifically, in this Chapter, an autoregressive integrated moving average model with exogenous variables is proposed to generate a Navigation Sequence (NS) to guide LSTM for multi-step prediction. As a consequence, a novel Navigation Sequence Driven LSTM (NSD-LSTM) prognostic strategy design is proposed. The strategy is then tested using different fuel cell long-term aging datasets, including those obtained in both static and dynamic operating conditions. The enhanced multi-step prediction capability and RUL estimation performance are then highlighted by comparing the proposed NSD-LSTM

with two state-of-the-art data-driven prognostic models, namely, Nonlinear Autoregressive Exogenous (NARX) [113] and ESN.

The remaining organization of this Chapter is as follows. In Section 3.2, the principles of LSTM and ARIMAX are briefly introduced. The prognostic strategy of NSD-LSTM is also presented in the same section. In Section 3.3, FC aging experiments and data preprocessing are introduced. Then, the proposed prognostic strategy is tested and compared with NARX and ESN models in Section 3.4. Finally, the Section 3.5 is the summary and discussion.

3.2. NSD-LSTM based prognostics strategy

3.2.1. ARIMAX model

The ARIMAX model is one of the most commonly used time series analysis models [114], which can be used to explain the relationship between system variables. In literature [115], the author applies several artificial intelligence models and ARIMAX to predict time series. Compared with other state-of-the-art models, thanks to the addition of Exogenous Sequences (XS), the ARIMAX model is considered to be a useful method for predicting time series.

Assuming that k input variable sequences ($\{x_{1t}\}, \{x_{2t}\}, \dots, \{x_{kt}\}$), including the XS and the historical HI sequence, are stationary, where $t \in \mathbb{R}^l$ corresponds to l time steps. The regression model between the output variable sequence $\{y_t\}$ and the input variable sequences is as follows:

$$y_t = \mu + \sum_{i=1}^{k} [\Theta_i(B)/\Phi_i(B)]\, B^{L_i} x_{it} + \varepsilon_t \tag{3.1}$$

where μ is the mean vector of $\{y_t\}$, and $\{\varepsilon_t\}$ represents regression residual sequence. $\{x_{it}\}$ is the i-th ($i = 1, 2, \dots, k$) input variable sequence. L_i represents the i-th lag degree. B is backshift operator such as $B^{L_i} x_{it} = x_{it-L_i}$. $\Theta_i(B) = \Theta_0^i - \sum_{j=1}^{q} \Theta_j^i B^j$ denotes q-order moving average polynomial of $\{x_{it}\}$, and $\Phi_i(B) = \Phi_0^i - \sum_{j=1}^{p} \Phi_j^i B^j$ denotes p-order autoregressive polynomial of $\{x_{it}\}$.

Since both $\{y_t\}$ and $\{x_{it}\}$ are stationary sequences, the $\{\varepsilon_t\}$ is also stationary:

$$\varepsilon_t = y_t - \left\{\mu + \sum_{i=1}^{k} [\Theta_i(B)/\Phi_i(B)]\, B^{L_i} x_{it}\right\} \tag{3.2}$$

Assuming that $\{\varepsilon_t\}$ is a non-white noise sequence, the autoregressive moving average model is then used to extract the information. The final fitted model is:

$$\begin{cases} y_t = \mu + \sum_{i=1}^{k} [\Theta_i(B)/\Phi_i(B)]\, B^{L_i} x_{it} + \varepsilon_t \\ \varepsilon_t = [\theta(B)/\phi(B)] a_t \end{cases} \tag{3.3}$$

where $\theta(B) = 1 - \sum_{j=1}^{q} \theta_j B^j$ is the q-order moving average operator, and $\phi(B) = 1 - \sum_{j=1}^{p} \phi_j B^j$ is the p-order autoregressive operator. $\{a_t\}$ is a zero-mean white noise sequence [114]. The specific process of generating NS using the ARIMAX model will be described in detail in Section 3.2.3.

3.2.2. LSTM structure

The aging degradation process of FC generally lasts thousands to tens of thousands of hours. LSTM can selectively store the intrinsic information of long-term data and capture the long time-scale correlation between time series data. In fact, as in [36, 56, 75], the LSTM-based prognostics framework is demonstrated to be capable of predicting the short-term PEMFC degradation behavior. Specifically, the basic network configuration of the LSTM contains three layers, namely the input layer, the single LSTM layer, and the output layer, as in Figure 3.1 (a).

To eliminate the risk of gradient disappearance or explosion in RNN, the LSTM creates a path that allows the gradient to flow continuously for a long time through an ingenious controllable self-circulation [36]. Specifically, in a single LSTM layer, h hidden units are connected sequentially to form a chain, which allows the cell state ($c_t \in \mathbb{R}^h$) and the hidden state ($h_t \in \mathbb{R}^h$) to be continuously passed, as in Figure 3.1 (b). The $x_t \in \mathbb{R}^d$ (the superscript d refers to the number of input features) from the input layer enters the hidden unit along with the previous unit outputs (c_{t-1} and h_{t-1}). The new outputs (c_t and h_t) are generated with the collaboration of forget gate ($f_t \in \mathbb{R}^h$), input gate ($i_t \in \mathbb{R}^h$), output gate ($o_t \in \mathbb{R}^h$), and the internal state unit ($\tilde{c}_t \in \mathbb{R}^h$) [56].

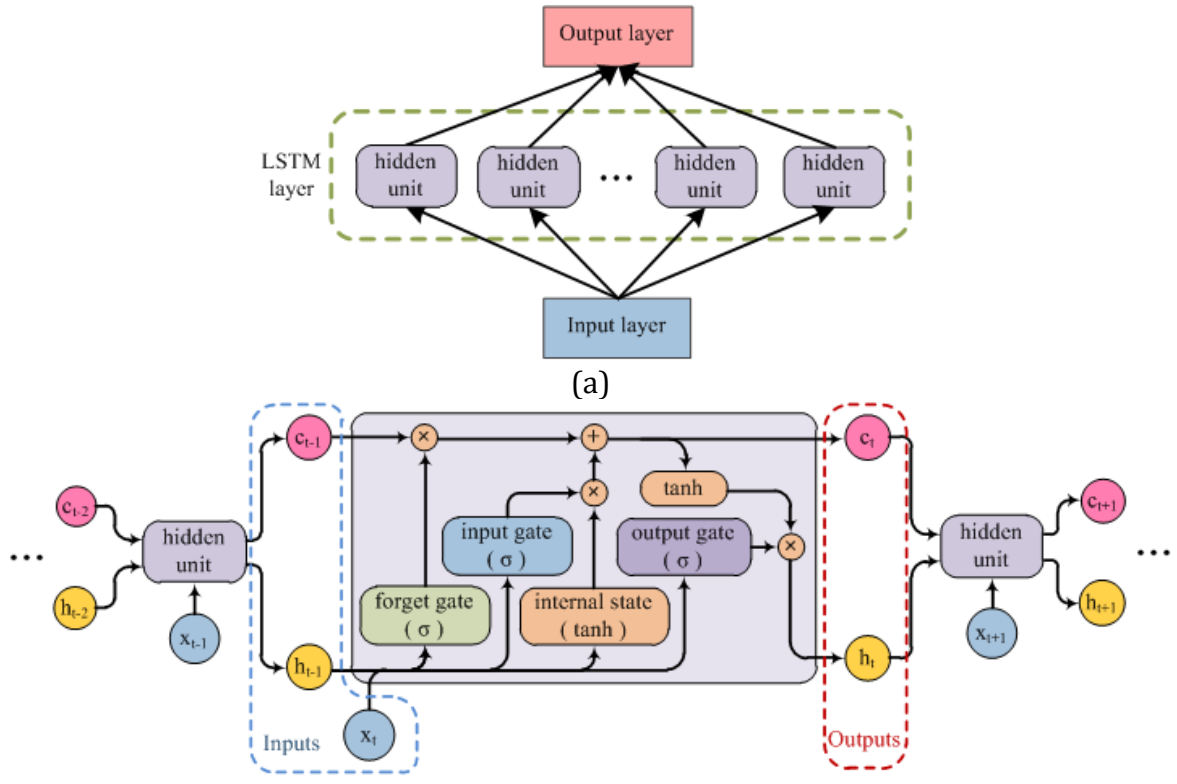

Figure 3.1 Illustration of LSTM model: (a) LSTM (single-layer) network configuration; (b) hidden unit chain and individual unit structure.

Equations (3.4) to (3.9) show the functional equations of LSTM

$$f_t = \sigma\left(W_f x_t + U_f h_{t-1} + b_f\right) \tag{3.4}$$

$$i_t = \sigma(W_i x_t + U_i h_{t-1} + b_i) \tag{3.5}$$

$$o_t = \sigma(W_o x_t + U_o h_{t-1} + b_o) \tag{3.6}$$

$$\tilde{c}_t = \tanh(W_c x_t + U_c h_{t-1} + b_c) \tag{3.7}$$

$$c_t = f_t \circ c_{t-1} + i_t \circ \tilde{c}_t \tag{3.8}$$

$$h_t = o_t \circ \tanh(c_t) \tag{3.9}$$

where the matrices $W_q \in \mathbb{R}^{h \times d}$ and $U_q \in \mathbb{R}^{h \times h}$ contain, respectively, the weights of the input and recurrent connections, where the subscript q can be either the input gate i, output gate o, the forget gate f or the cell state c. Similarly, the vectors $b_q \in \mathbb{R}^h$, such as b_f, b_i, b_o and b_c, are the bias of each component [56]. The gate activation function σ is the sigmoid function with "S"-shaped curve characteristics. It can be defined by the following equation.

$$\sigma(x) = \frac{1}{1 + e^{-x}} \tag{3.10}$$

And the internal state activation function tanh is hyperbolic tangent function. It can be defined by the following equation.

$$\tanh(x) = \frac{e^{x} - e^{-x}}{e^{x} + e^{-x}} \tag{3.11}$$

While, the operator "$\circ$" denotes the Hadamard (element-wise) product, which is a binary operation[36]. The Hadamard product operation between two matrices, both of $m \times n$ dimensions, is defined as follows.

$$\begin{bmatrix} a_{11} & a_{12} & \cdots & a_{1n} \\ a_{21} & a_{22} & \cdots & a_{2n} \\ \vdots & \vdots & \ddots & \vdots \\ a_{m1} & a_{m2} & \cdots & a_{mn} \end{bmatrix} \circ \begin{bmatrix} b_{11} & b_{12} & \cdots & b_{1n} \\ b_{21} & b_{22} & \cdots & b_{2n} \\ \vdots & \vdots & \ddots & \vdots \\ b_{m1} & b_{m2} & \cdots & b_{mn} \end{bmatrix} = \begin{bmatrix} a_{11}b_{11} & a_{12}b_{12} & \cdots & a_{1n}b_{1n} \\ a_{21}b_{21} & a_{22}b_{22} & \cdots & a_{2n}b_{2n} \\ \vdots & \vdots & \ddots & \vdots \\ a_{m1}b_{m1} & a_{m2}b_{m2} & \cdots & a_{mn}b_{mn} \end{bmatrix} \tag{3.12}$$

3.2.3. NSD-LSTM model architecture

FC operation involves coupled multi-physics processes. The aging degradation of FC is time-varying, highly uncertain and correlated to these processes. This leads to the prognostics, supposed to predict the intrinsic FC degradation evolution, is disturbed. Moreover, the prognostics model built on the historical data of the identical FC also suffers from the epistemic uncertainty as the predicted data evolve within an unseen quantity interval. In order to handle the disturbances from both the system operation/degradation and model uncertainties, the LSTM based prognostics model should be trained so as to trace the intrinsic degradation evolution. With this in mind, this Chapter proposes a novel prognostics strategy based on NSD-LSTM, which takes into account the characteristics of LSTM and ARIMAX. The overall NSD-LSTM based prognostics strategy is shown in Figure 3.2. The strategy is divided into three parts: dataset preprocessing, offline phase and online phase.

3.2.3.1. Dataset preprocessing

The upper left frame of Figure 3.2 shows the dataset preprocessing phase of the strategy. The purpose of this phase is to adjust the HI sequence to make it suitable for prognostics. The HI can be the stack voltage sequence from the aging experiment, or the virtual nominal stack voltage mentioned in the literature [85].

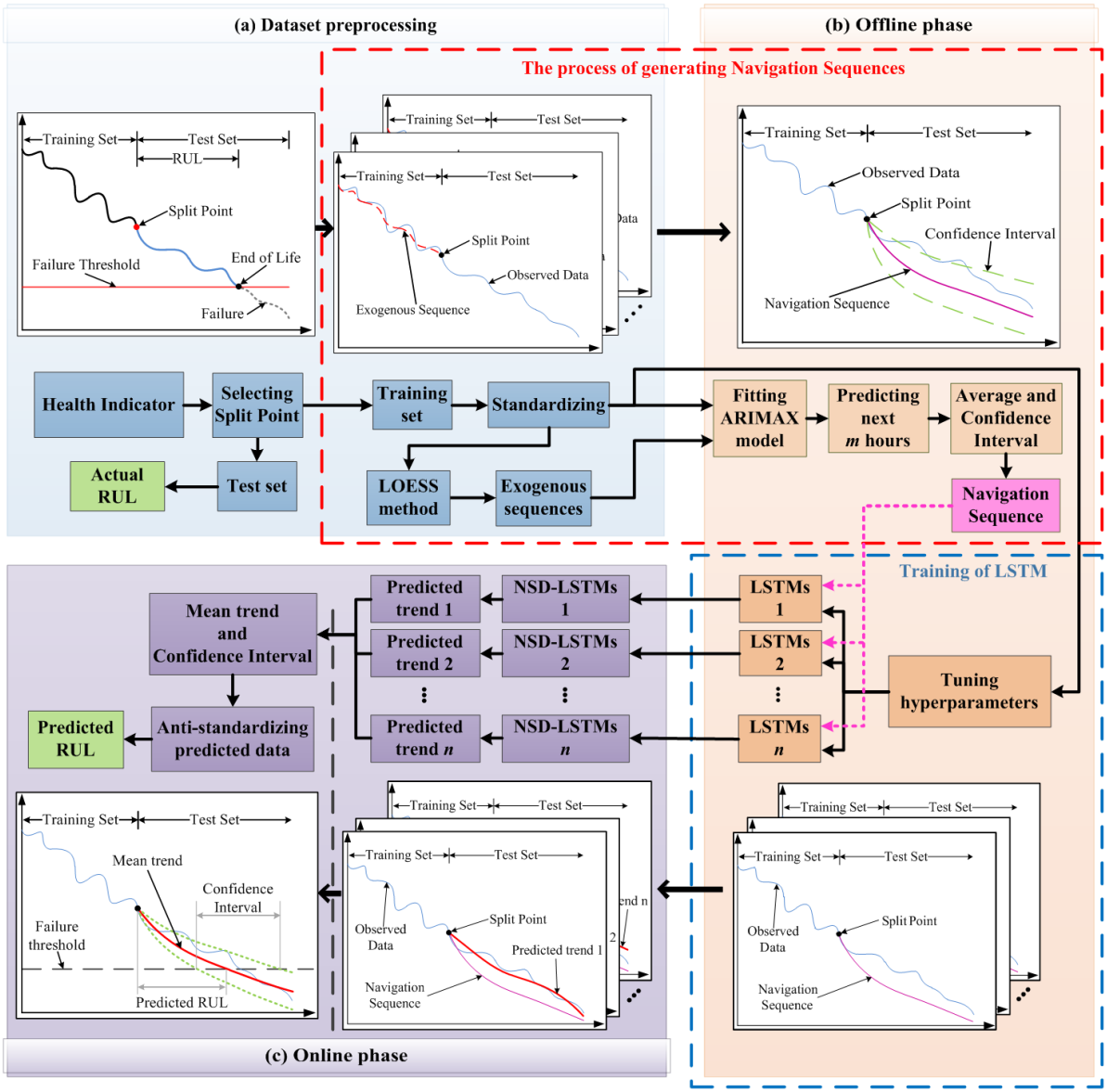

Figure 3.2 The prognostics process based on NSD-LSTM. (a) Dataset preprocessing: datasets segmentation, standardization, exogenous sequences generation; (b) Offline phase: navigation sequence generation, training of LSTM; (c) Online phase: long-term degradation trends prediction, RUL prediction.

The first step is to select the split point (also known as the prediction starting point). The split point can divide the HI sequence into a training set and a test set. Further, the test set can be used to calculate the real RUL. Subsequently, it is necessary to select the Failure Threshold (FT), and determine the actual End of Life (EoL) according to FT. Then the actual RUL is calculated as

$$RUL = EoL - t_0 \tag{3.13}$$

where t_0 is the operating time at the split point. It is worth mentioning that the test set is considered unknown in both offline and online phases, in order to avoid data leakage, as in practical conditions.

The second step is to standardize the training set using:

$$z_{std} = (z - \overline{z})/SD \tag{3.14}$$

where $\{z\}$ is the raw training set sequence, $\overline{z}$ is the average, SD is the standard deviation, and $\{z_{std}\}$ is the standardized training set sequence.

The third step is to generate multiple XS for the ARIMAX model. The XS are introduced to better retain the main trends in the raw training set while filtering out anomalous and meaningless data fluctuations. Specifically, by adjusting the smoothing coefficient in the Locally Estimated Scatterplot Smoothing (LOESS) method [56], multiple XS with different smoothing levels can be obtained. These different smoothing levels facilitate diversified exogenous information for ARIMAX to prevent the impact by uncertainty disturbances. Moreover, each XS can eliminate some fluctuations mainly due to the system operation while retaining the long-term degradation trend.

3.2.3.2. Offline phase

The offline phase is displayed on the right frame of Figure 3.2. This phase contains two parts: generating NS and training LSTM.

1) Generating NS

The NS generation process is shown in the red dashed box in Figure 3.2. The training set and XS generated in the preprocessing phase will be used to fit the ARIMAX model. Specifically, a series of ARIMAX models are fitted using multiple (here n) different XS. Based on these models n candidate sequences for NS can be predicted. Then, at the k-th predicted instance after the split point, the average predicted value and the Confidence Interval (CI) can be calculated respectively, as

$$\overline{\hat{y}}_k = \frac{\sum_{i=1}^{n} \hat{y}_k^i}{n} \tag{3.15}$$

$$CI_k = \overline{\hat{y}}_k \pm 1.96 SD_k \tag{3.16}$$

Where $\hat{y}_k^i$ is the i-th $(i \in \{1,2,\dots,n\})$ predicted value, $\overline{\hat{y}}_k$ represents the average predicted value of the k-th time step, and SD_k denotes the identified standard deviation. The constant 1.96 means 95% CI. The CI_k are the confidence interval bounds. The average predicted value sequence $\{\overline{\hat{y}}\}$ is considered as the NS.

2) Training LSTM

In the training LSTM stage , Adam is utilized as an optimizer to facilitate hyperparameters tuning, because it is computationally efficient and has little memory requirements [116]. This drives the model to converge to the minimum generalization error in a stable and rapid manner. Meanwhile, Adam is proven to be suitable for training LSTM [35, 56]. Different settings of hyperparameters and initialized weight matrices can bring diversity to the LSTM model. This variation of model is not fully

controllable for the prediction phase. Any well-trained LSTM model can be considered to perform effectively in the training set, yet there is often a significant difference in its performance in the test set. Setting the multiple initialization weight matrixes of hidden units randomly, multiple LSTM can be trained to generate multiple prognostics models, such as LSTM 1, LSTM 2, ..., LSTM *n* shown in the blue dashed box in Figure 3.2. The multiple LSTM setting benefits to provide diverse prediction results, which will be used further to improve the model epistemic uncertainty.

3.2.3.3. Online phase

As shown in the right frame in Figure 3.2, the HI trend prediction and the RUL estimation are completed in the online phase.

(1) Predicting degradation trends

Multi-step prediction is achieved by deploying well-trained LSTM iteratively for single-step prediction. Specifically, in order to break the historical numerical interval and mitigate the cumulative single-step prediction error, the NSD-LSTM model uses NS rather than the previous step prediction value as model input. Corresponding to multiple well-trained LSTM models in the offline phase, a series of NSD-LSTM models (NSD-LSTM 1, ... , NSD-LSTM *n*) will be formed in the online phase. These NSD-LSTM models will give *n* different HI degradation prediction results. Assuming that the *n* predicted degradation trends follow the standard Gaussian distribution, which can be tested by hypothesis testing, the mean trend composed of the average of these predicted values is regarded as the final predicted HI degradation trend, and the CI is configured as a 95% probability interval using Equation (3.16).

(2) RUL estimation

The estimated end of life ($\widehat{EoL}$) is considered to be the operating time when the mean trend first-time reaches the FT. The estimated remaining useful life ($\widehat{RUL}$) is calculated according to equation:

$$\widehat{RUL} = \widehat{EoL} - t_0 \tag{3.17}$$

Additionally, the computing cost of the NSD-LSTM model will be discussed in Section 3.4.

3.3. Long-term FC aging tests and prognostics data sets

3.3.1. FC aging experiments

In view of the FC lifetime data scarcity limitations and the operating conditions influences. In this Chapter, two long-term FC aging experiments are conducted under constant and dynamic-load conditions, respectively.

3.3.1.1. Constant-load aging experiment

The first FC aging experiment in constant-load operating condition is completed on a 1kW Proton Motor 200 fuel cell. In this experiment, the Proton Motor 200 FC stack with 96 cells is tested under the operating conditions shown in Table 3.1 [36].

Operating mode	Constant-load
Air supply	Air blower & filter
Cooling system	Deionized-water/glycol
Fuel gas supply	99.99% dry H_2@1.5 bar
Number of cells	96
Operating hours	10430 h
Stack temperature	58 °C
Current density	0.64 A/cm^2

Table 3.1 Constant-load aging experiment operating condition.

3.3.1.2. Dynamic-load aging experiment

In the dynamic-load aging experiment, the concerned FC stack is of an open cathode and a dead-end anode structure. Some operating conditions are shown in Table 3.2. One 24 V DC-fan realizes the functions of air supply and temperature adjustment. The pressure of hydrogen as fuel is fixed at about 1.35 bar. In addition, FC is self-humidifying and a purge lasting for 0.5 seconds is activated every 30 seconds. In order to get closer to the dynamic operating conditions of FC in electric vehicle applications, a programmable electronic DC load is used to set the output current in the experiment [85].

Operating mode	Dynamic-load
FC type	Open cathode/Dead-end anode
Active surface	33.63 cm^2
Number of cells	15
Nominal output power	73.5 W
Operating temperature	corresponding to current
Maximum temperature	75 °C
Maximum current	13.45 A
Lowest permitted stack voltage	7.5 V
Pressure interval at hydrogen inlet	0.10 to 0.40 bar

Table 3.2 Dynamic-load aging experiment operating condition.

3.3.2. Datasets for prognostics

The observed/virtual average cell voltages are specified as HI sequences to verify the reliability and generalization of the prognostics strategy. Through the data set preprocessing method mentioned in Section 3.2, the HI sequences are processed to be suitable for prognostics. Figure 3.3 shows the pre-processed datasets.

(1) Constant-load dataset

The constant-load dataset is the average cell voltage, which comes from the actual stack voltage measured in the Proton Motor 200 aging experiment. In the dataset, the highest voltage is 0.654 V and the lowest

voltage is 0.523 V. The average initial voltage is 0.650 V, and the failure threshold is set to 0.533 V. The actual EoL corresponding to this failure threshold is 8583.3 h. As shown in Figure 3.3 (a), there are three obvious voltage fluctuations, which are caused by the failures of auxiliary components such as the air blower or the cooling system. In the experiment to verify the prognostics strategy, a series of split points are selected. From point A (5261.1 h) to point B (7378.2 h), 21 split points are set at equal intervals. Among them, between points A and B, four points are selected for comparison experiment: point 1 (5580.5 h), point 2 (6078.3 h), point 3 (6573.2 h), and point 4 (7151.6 h).

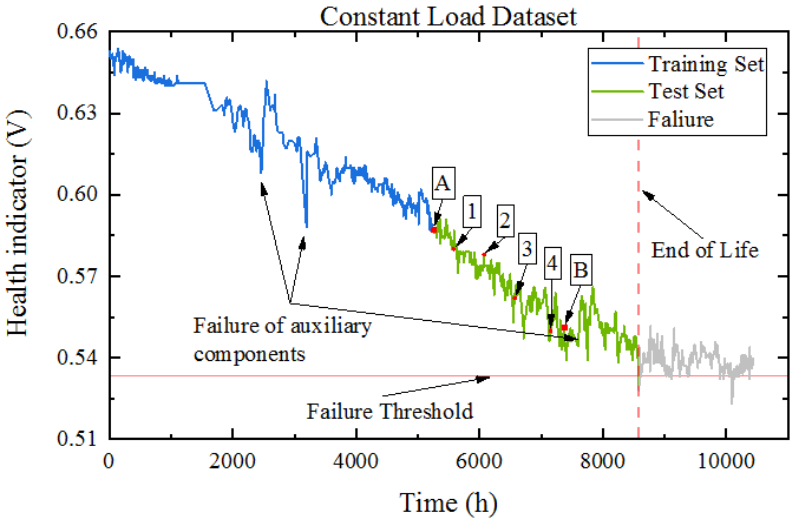

(a)

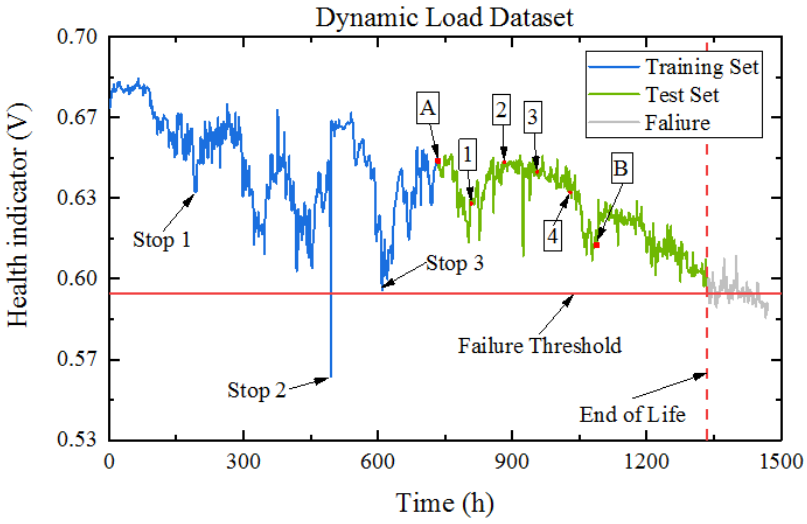

(b)

Figure 3.3 Fuel cell aging experimental datasets: (a) average cell voltage in the constant-load, (b) virtual nominal average cell voltage in the dynamic-load.

(2) Dynamic-load dataset

The dynamic-load dataset is about a HI extracted using the same method proposed in the literature [85]. The HI can be considered as the nominal

average cell voltage of the concerned stack. In the dynamic-load dataset, the highest voltage is 0.683 V and the lowest voltage is 0.559 V. The average initial voltage is 0.676 V, and the failure threshold is set to 0.595 V. The actual EoL corresponding to this failure threshold is 1335 h. As shown in Figure 3.3 (b), there are three abnormal stops. Among them, the most obvious voltage fluctuation is near to stop 2 which is related to an unexpected system stop of hydrogen depletion. In the experiment to verify the prognostics strategy, a series of split points are selected. From point A (735 h) to point B (1087.5 h), 25 split points are set at equal intervals. Among them, between points A and B, four points are selected for comparison experiment: point 1 (808.5 h), point 2 (882 h), point 3 (955.5 h), and point 4 (1029 h).

3.4. Evaluation of prognostics strategy

3.4.1. Evaluation criteria

This Chapter sets two evaluation criteria: the Root-mean-square Error (RMSE) and the Relative Error (RE). The RMSE evaluates the single-step prediction performance, and the RE is used in the online phase to evaluate the accuracy of the estimated RUL from the prognostics strategy. The mathematical description of RMSE and RE are given by:

$$RMSE = \sqrt{\frac{\sum_{j=1}^{m}\left(u_j - \hat{u}_j\right)^2}{m}} \tag{3.18}$$

$$RE = \frac{|x - \hat{x}|}{x} \times 100\% \tag{3.19}$$

where, u_j is the actual stack voltage observation value in the training set; $\hat{u}_j$ is the predicted voltage value by the well-trained LSTM and/or ARIMAX model in the offline phase; m is the sample number under evaluation. x can be the actual remaining useful life (RUL); $\hat{x}$ corresponds to the predicted remaining useful life ($\widehat{RUL}$).

3.4.2. Prognostics experiment and discussion

The programs used in the FC prognostics experiment are developed in a Matlab R2019b environment. Even with the help of Adam, some hyperparameters configuration and tuning still rely on manual adjustment. The following are part of the hyperparameters configured and tuned in this Chapter: the number of hidden units is set to 200 to ensure prediction accuracy and regulate model complexity; the dynamic learning rate is set to 0.001 initially and becomes smaller by 80% after 100 epochs to avoid training loss oscillation, overfitting, or slow convergence; the maximum training epoch is set to 150 based on the data characteristics of the training sets; the gradient threshold is set to 1 for avoiding gradient explosion.

3.4.2.1. Single-step prediction performance comparison test between LSTM and ARIMAX

In this Chapter, long-term/multi-step prediction is achieved by deploying single-step prediction iteratively. Therefore, it is essential to evaluate the credibility of the single-step prediction. Specifically, this evaluation uses the test set as input to evaluate the well-trained LSTM model in the NSD-LSTM. Moreover, in order to more comprehensively evaluate the single-step prediction performance, a comparison test between the ARIMAX model and the well-trained LSTM model is utilized. The results of the tests performed at point A of the two different load datasets are shown in Figure 3.4, Figure 3.5 and Table 3.3. The results show that the ARIMAX model tends to be more trend-holding, while the LSTM is better at describing degradation behavior in detail. The LSTM predicted values match the test set well, and the RMSEs (as in Table 3.3) are slightly better than ARIMAX under different loads. However, it is undeniable that the error of LSTM gradually increases as the prediction continues, especially in the dataset with dynamic-load.

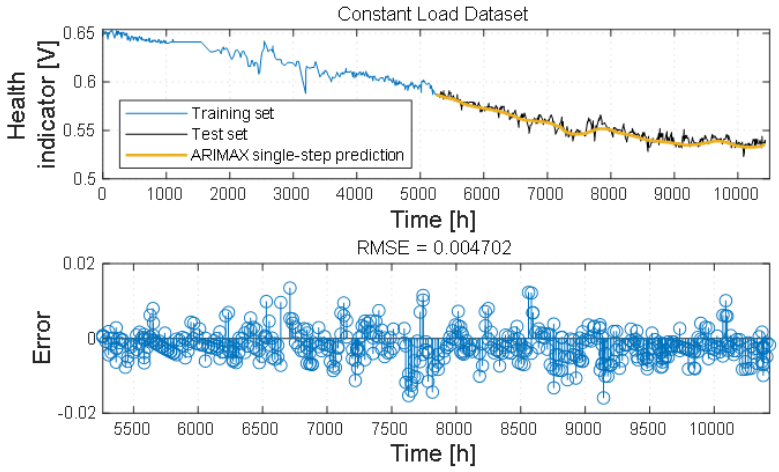

(a)

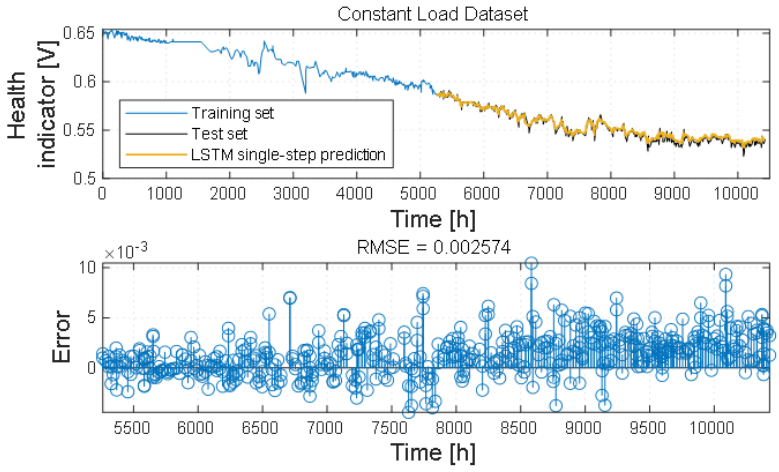

(b)

Figure 3.4 Single-step prediction at split point A of constant-load dataset, (a) ARIMAX model; (b) LSTM model.

Dataset	Model	RMSE	Error (range)	Note
Constant-load	ARIMAX	0.004702	-0.0158 to 0.0135	Figure 3.4 (a)
	LSTM	0.002574	-0.0044 to 0.0105	Figure 3.4 (b)
Dynamic-load	ARIMAX	0.006095	-0.0129 to 0.0334	Figure 3.5 (a)
	LSTM	0.005577	-0.0072 to 0.0135	Figure 3.5 (b)

Table 3.3 Comparison experiments of single-step prediction performance.

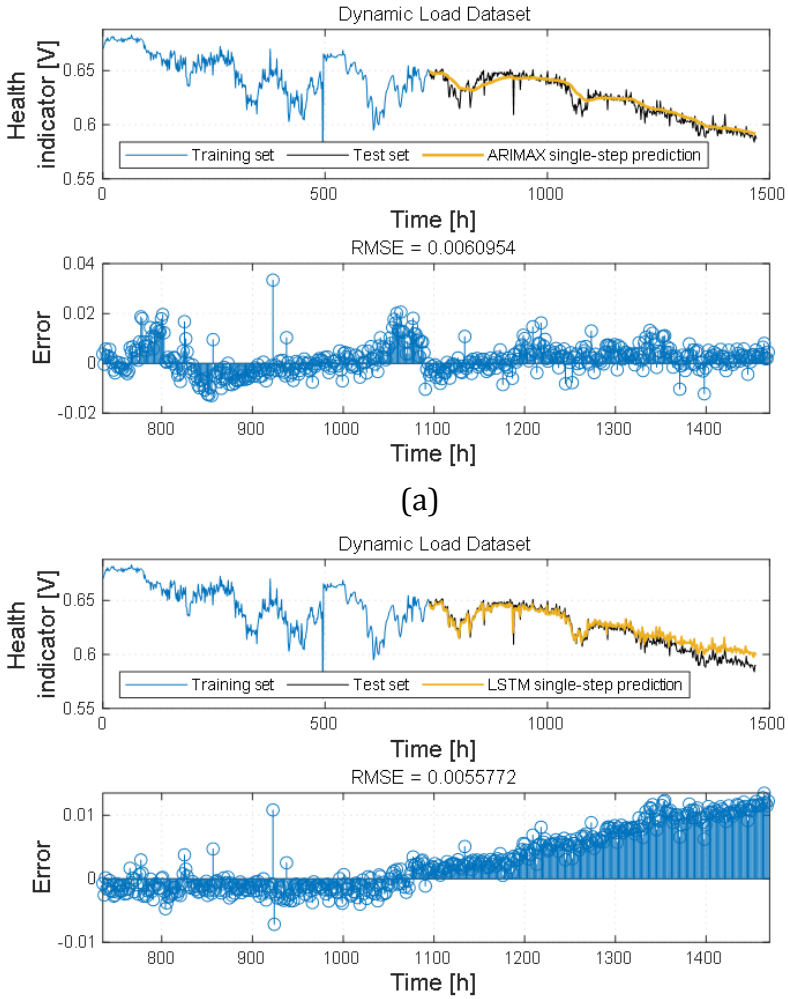

Figure 3.5 Single-step prediction at split point A of dynamic-load dataset, (a) ARIMAX model; (b) LSTM model.

In addition, the errors of LSTM are almost always positive when the errors become progressively larger, which confirms that the LSTM is limited by the historical data. Not to be neglected, the above single-step prediction results depend on future observations (test set). In case of observation scarcity, single-step predictions cannot provide long-term RUL estimates due to the prediction length limitation. Meanwhile, prediction results that reflect positive errors tend to provide lifetime valuations larger than the actual RUL, which further leads to the risk of fatal failures before maintenance. In

summary, LSTM outperforms ARIMAX in single-step prediction, but still relies on multi-step prediction to achieve long-term prognostics.

Specifically, it should be noted that (1) Section 3.4.2.1 is devoted to discuss the single-step prediction capability of well-trained LSTM models in NSD-LSTM. (2) In the actual deployment of NSD-LSTM, the single-step prediction performance is considered to be fully optimized through the training phase. (3) In practice, highly accurate single-step prediction is more meaningful in real-time controlling fuel cell applications.

3.4.2.2. Evaluating the multi-step prediction performance

Multi-step prediction provides a longer prediction range and is the prerequisite for estimating RUL. To properly evaluate the multi-step prediction capability of the NSD-LSTM, 20 trend predictions are performed at each split point between points A and B. The mean trend is calculated as the multi-step prediction result and then compared with the ARIMAX and LSTM.

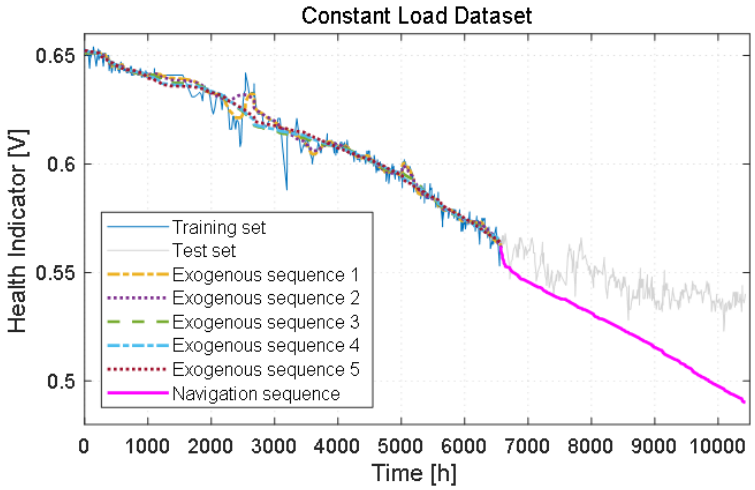

(a)

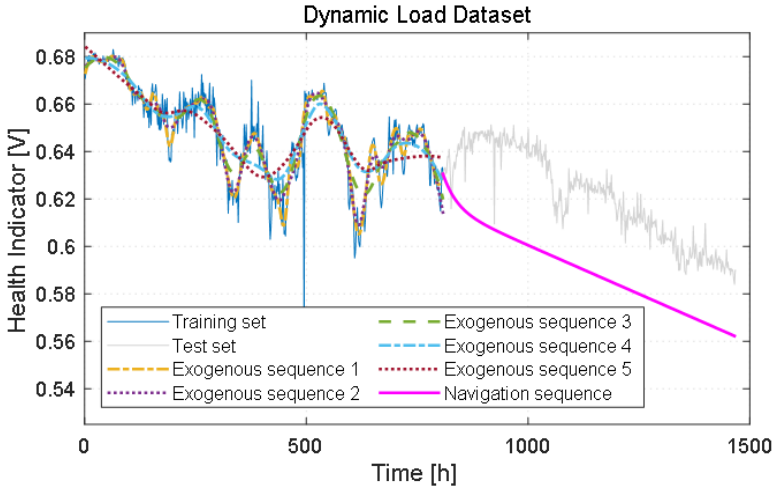

(b)

Figure 3.6 At split point 3 of constant-load dataset, (a) 5 different exogenous sequences (XS); At split point 1 of dynamic-load dataset, (b) 5 different exogenous sequences (XS).

Firstly, as in Figure 3.6 (a) and (b), various XS are generated in the data preprocessing phase by setting five different smoothing levels. Subsequently, in the offline phase, NS is generated by using ARIMAX model. The generated NS can maintain the historical potential trends in the HI, which facilitates to guide the NSD-LSTM during long-term degradation prediction.

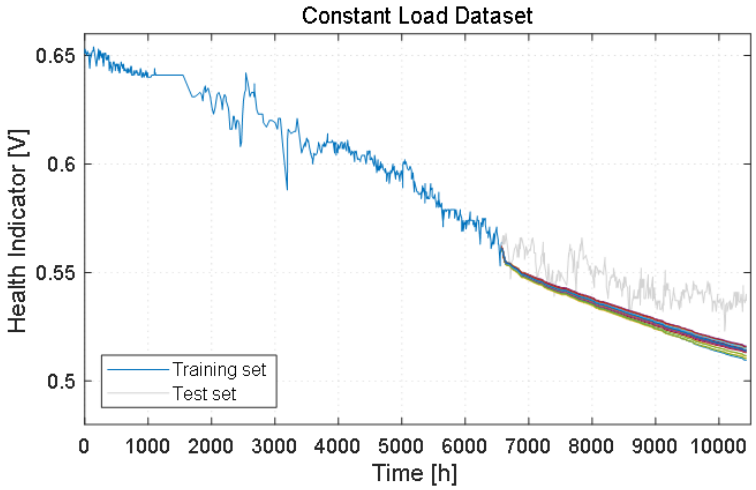

(a)

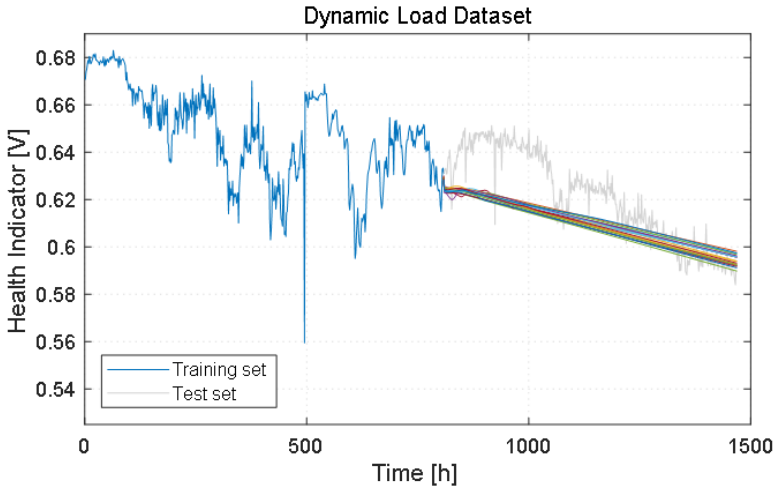

(b)

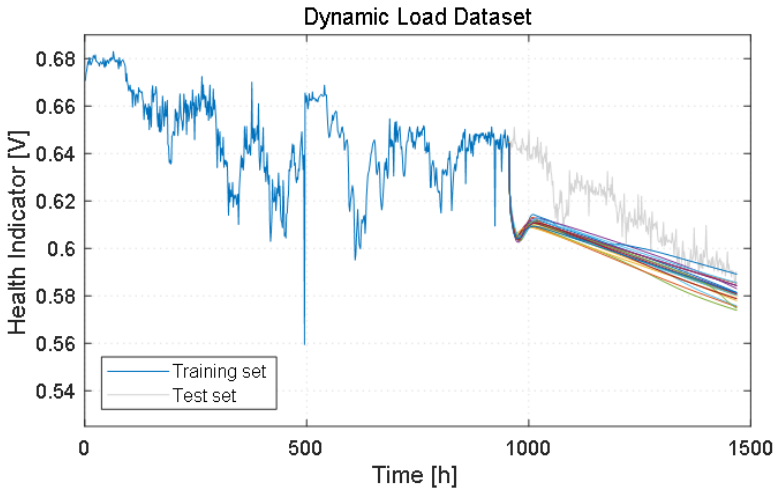

(c)

Figure 3.7 At split point 3 of constant-load dataset, (a) 20 predicted degradation trends (the colorful lines); At split point 1 of dynamic-load dataset, (b) 20 predicted degradation trends (the colorful lines); At split point 3 of dynamic-load dataset, (c) 20 predicted degradation trends (the colorful lines).

Secondly, the HI degradation trends (as the colorful lines in Figure 3.7 (a), (b) and (c)) predicted by NSD-LSTM remain consistent across the different load data sets. Meanwhile, the predicted trends are slightly lower than the test set in most cases. This helps to avoid estimating larger RULs and is expected to provide further maintenance recommendations with redundancy.

Thirdly, the prediction results of LSTM eventually converge to a horizontal line as the prediction time increases, as in Figure 3.8 (a), (b) and (c). This is reminiscent of the prevalent positive errors in the single-step predictions mentioned in Section 3.4.2.1 (Figure 3.4 (b) and Figure 3.5 (b)). It is confirms that LSTM is difficult to break the historical numerical interval, as well as the lack of long-term prediction ability. Further, the prediction results of ARIMAX retain partially historical trend information, but are generally much lower than the test set. This can cause the estimated RUL to be too small, triggering maintenance prematurely and increasing the cost. In contrast, NSD-LSTM gives more appropriate predictions.

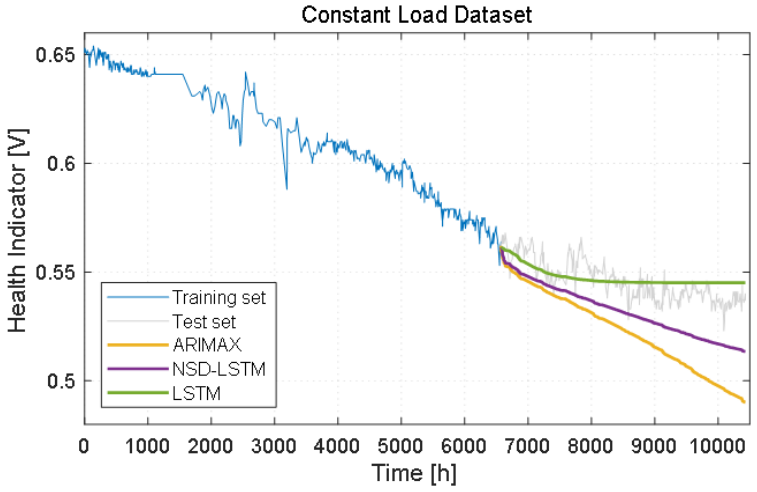

(a)

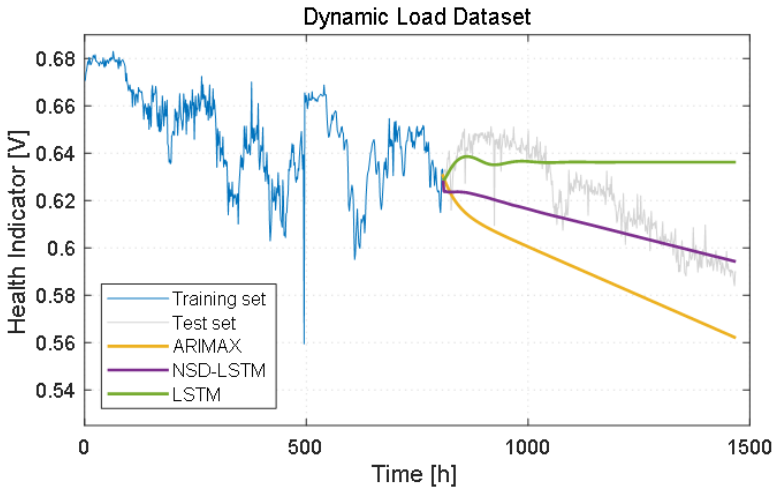

(b)

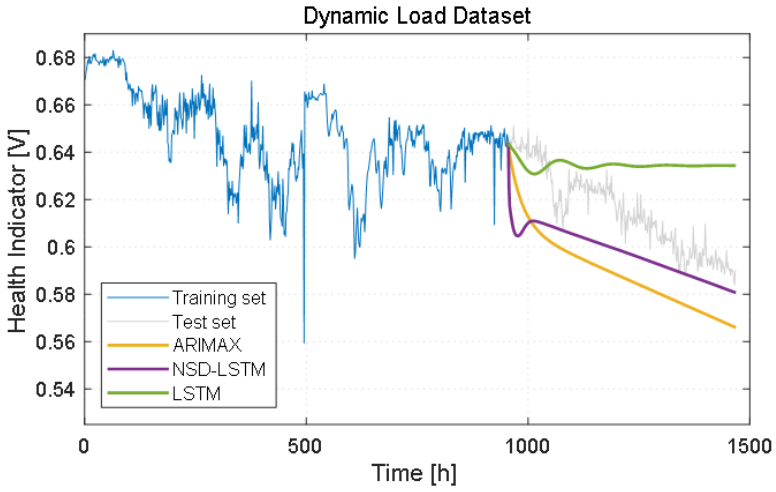

(c)

Figure 3.8 At split point 3 of constant-load dataset, (a) multi-step prediction results comparison. At split point 1 of dynamic-load dataset, (b) multi-step prediction results comparison. At split point 3 of dynamic-load dataset, (c) multi-step prediction results comparison.

Another interesting feature of the proposed NSD-LSTM model is that both short-term voltage fluctuations and long-term voltage evolution in the historical data can be captured and reflected in the prediction results. As in Figure 3.7 (c) and Figure 3.8 (c), the predicted degradation trends appear to be quite different from the previous ones. The predicted trends show a clear and rapid decline at the beginning of the prediction horizon, and then gradually restored a quasi-linear decline. Among them, the obvious rapid decline in the early stage of the prediction is due to the fact that the relatively abnormal voltage drop before the split point is captured by the NSD-LSTM model. The abnormal voltage drop may indicate that the fuel cell is undergoing changes in operating conditions or encountering the failure of auxiliary equipment. These factors will lead to the changes in the HI degradation trend in the future, so it is meaningful to consider such abnormal voltage drops in the long-term prognostics. Subsequently, the predicted trend returns to a state similar to a quasi-linear decline, and continues to maintain the global downward trend contained in the training set. Therefore, the prediction based on NSD-LSTM model not only considers the abnormal HI changes that may affect the trend evolution, but also adjusts the prediction results in a relatively short time to retain the global degradation trend shown in the training set. Such prediction property highlights the robustness of NSD-LSTM against the disturbances from system operations and recoverable faults.

Furthermore, on a regular personal computer, the CPU is used for model training and prediction. As in Table 3.4, the computing costs of the three models are compared. In the training/fitting (offline) phase, the computing cost of NSD-LSTM is slightly higher than that of LSTM, and ARIMAX performs the best. In the offline phase, there is usually ample time for model training and hyperparameter tuning, so this is acceptable. More interestingly, the computing cost of the all models is almost as well during prediction. It indicates that NSD-LSTM has the ability to implement online prediction. Specifically, the

term “robustness” mentioned in this Chapter mainly refers to an ability of the proposed prognostics method to counteract abnormal fluctuations in health indicators and to keep the predicted results in line with the inherent degradation trend of the fuel cell.

Dataset	Split point	Training/fitting time (s)			Predicting time (s)		
		ARIMAX	LSTM	NSD-LSTM	ARIMAX	LSTM	NSD-LSTM
Constant-load	3	3.85	57.27	64.45	1.53	1.37	1.44
Dynamic-load	1	3.75	36.70	43.56	1.71	1.57	1.59
	3	3.76	43.83	50.47	1.75	1.33	1.26

Table 3.4 Comparison of computing costs.

3.4.2.3. Evaluating RUL estimation

Thanks to the HI degradation trends predicted by the NSD-LSTM model, RUL can be estimated before the fuel cell failure. In order to evaluate the estimated RUL, multiple tests are performed between the split points A and B for both datasets.

Figure 3.9 (a) and (b) show the results of 21 RUL estimations and REs for the constant-load dataset. In this case, Figure 3.9 (a) has a dual y-axis. Among them, the left green y-axis represents the health indicator with unit V, corresponding to the green curve of the dataset. The right red y-axis represents RUL with unit h, corresponding to the red curve of the estimated RULs and the blue curve of the real RULs. The estimated RULs from the split point A to point B as a whole exhibit a phenomenon that fluctuates around the real RULs. It can be observed that the predicted fluctuations of RULs are consistent with those of the dataset. Specifically, the predicted RULs from split point A to split point 1 gradually approach the real RULs. This is because the training set near the split point shows an increasingly steep downward trend, which makes the predicted RULs tend from overestimation to the real RULs. The estimated RUL drops significantly after split point 1. This is because NSD-LSTM takes into account the abnormal drop in HI near the split point. Then the estimated RUL near split point 2 tends to maintain the same trend of the dataset. It is worth mentioning that there are several short-term HI drops between points 2 and 3 whose effects are not obviously reflected in the RUL estimation. The prognostics model tends to maintain the prediction consistency during this period. As there is a significant HI drop in the short period before point 3, the estimated RUL also drops significantly. Between split point 3 and split point 4, there are obvious fluctuations in the dataset, and the estimated RULs also exhibit similar fluctuations. Between split point 4 and split point B, the estimated RULs are very close to the real RULs. In Figure 3.9 (b), the REs of the estimated RULs are shown. The maximum RE is 77.73%, the minimum is 0.01%, and the average is 32.28%. In 21 tests, 17 REs are less than 50%, and this is considered to be acceptable for long-term prognostics. It should be noted that from split point A to split point B, the real RUL ranges from 3322.2 h to 1205.1 h, which means that NSD-LSTM need to perform RUL estimation for thousands of hours when the test set is unknown. In summary, for the constant-load

dataset, the estimated RULs fluctuate near the real RULs, and the fluctuation of the estimated RULs is consistent with the evolution trend of the dataset.

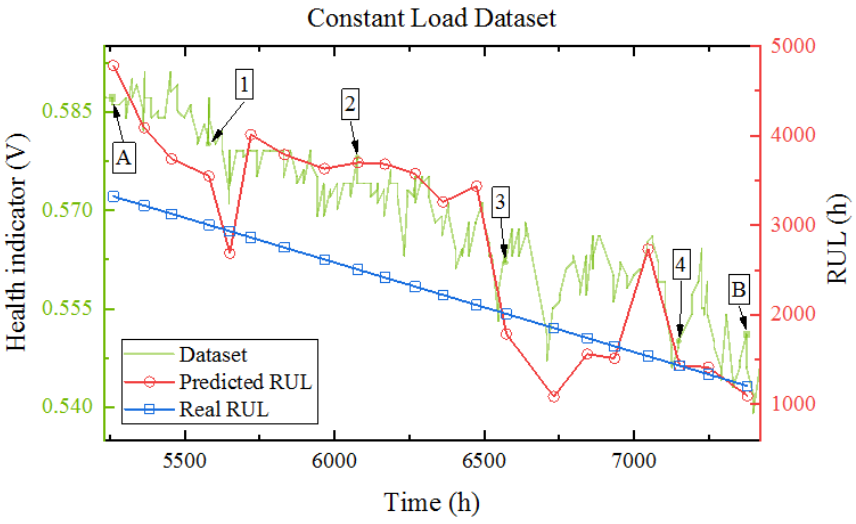

(a)

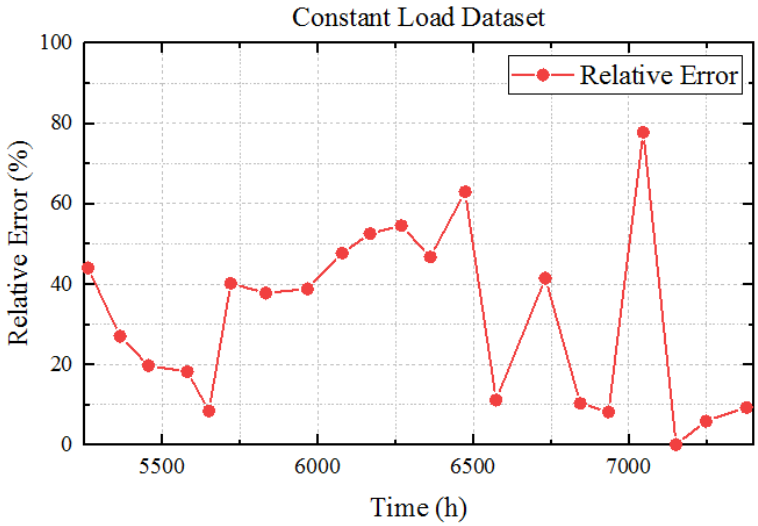

(b)

Figure 3.9 RUL estimation results from split point A to B for the constant-load dataset, (a) 21 estimated RULs versus real RULs and dataset; (b) 21 relative errors.

Figure 3.10 (a) and (b) shows the 25 RUL estimation results and the REs for the dynamic-load dataset. The axis significance is the same as in Figure 3.9 (a) and (b). Between split point A and split point 2, the estimated RULs are generally higher than the real RULs; and between split point 2 and split point B, the estimated RULs fluctuate near the real RULs. The estimated RULs are generally consistent with the dataset in terms of fluctuation trends. For instance, the estimated RULs rise slightly after point A, which is due to the HI increase related to the recovery from an abnormal stop of the fuel cell before point A ("stop 3" in Figure 3.3 (b)). Following that as far as split point 1, the dataset exhibits a significant HI drop and a recovery behavior. The estimated RULs also show a lagged similar evolution trend. It is worth noting that there are several "sags" in the dataset, such as the part between split point A and split point 3. These "sags" can be

understood as some recoverable faults or abnormal operating conditions [85]. From the results, the NSD-LSTM model can comprehensively consider the long-term and short-term degradation behaviors. In Figure 3.10 (b), the REs of the 25 estimated RULs are shown. The maximum value of REs is 72%, the minimum value is 0.9%, and the average value is 26.3%. In 25 tests, 22 REs are lower than 40%, which is considered to be acceptable for the prognostics under dynamic operating conditions. It should be noted that the real RUL range from split point A to split point B is 600 h to 247.5 h, which means that when the test set is unknown, the NSD-LSTM model needs to perform hundreds of hours of long-term RUL estimation. In summary, for the dynamic-load dataset, the estimated RULs can track the changes in the degradation behavior, and provide consistent and robust RUL estimates in the long-term prognostics.

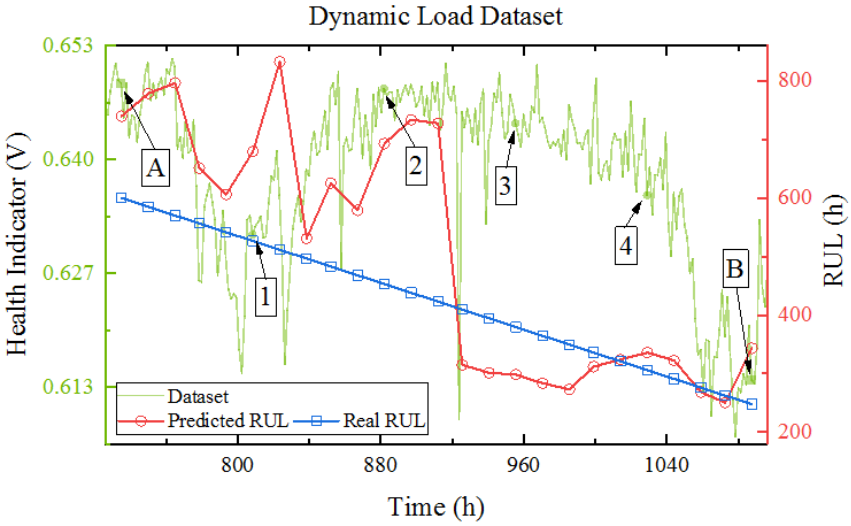

(a)

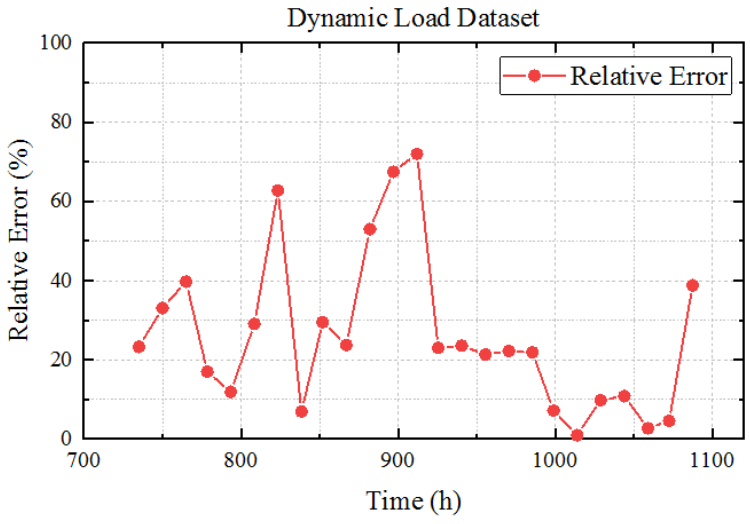

(b)

Figure 3.10 RUL estimation results from split point A to B for the dynamic-load dataset, (a) 25 estimated RULs versus real RULs and dataset; (b) 25 relative errors.

3.4.2.4. Comparison experiments

In order to further evaluate the consistency and robustness of the proposed prognostics strategy, comparison experiments are designed at split points 1, 2, 3 and 4 of the dynamic-load dataset. It should be pointed out that in these comparison experiments, the NARX model uses the same NS of the NSD-LSTM model as the exogenous variable. This will help reveal the guiding role of NS and highlight the LSTM performance. In addition, the ESN model in the comparison experiments is from [85].

As in Figure 3.11, the degradation trends predicted by the ESN at each of the four split points are different. Especially at split points 3 and 4, the trends predicted by ESN are close to the horizontal line. Compared with the ESN model, the trends predicted by the NARX model have better consistency at the four split points. However, as the prediction time increases, the trends predicted by NARX model gradually become flat.

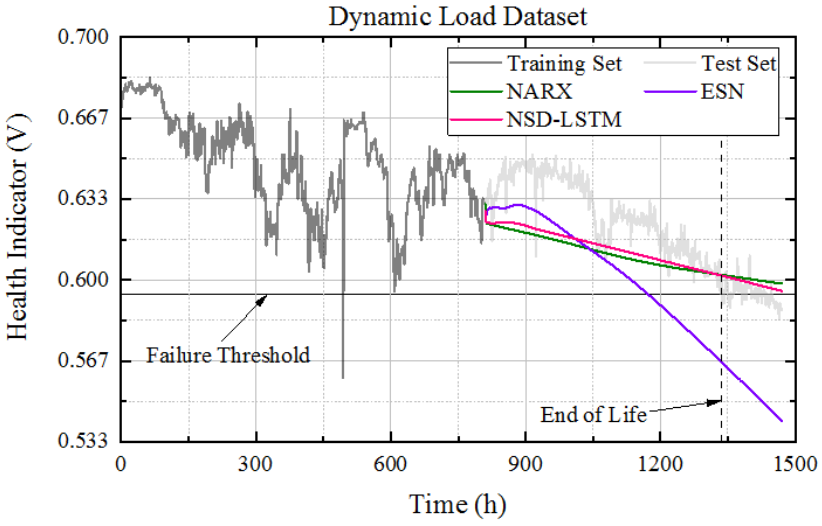

(a)

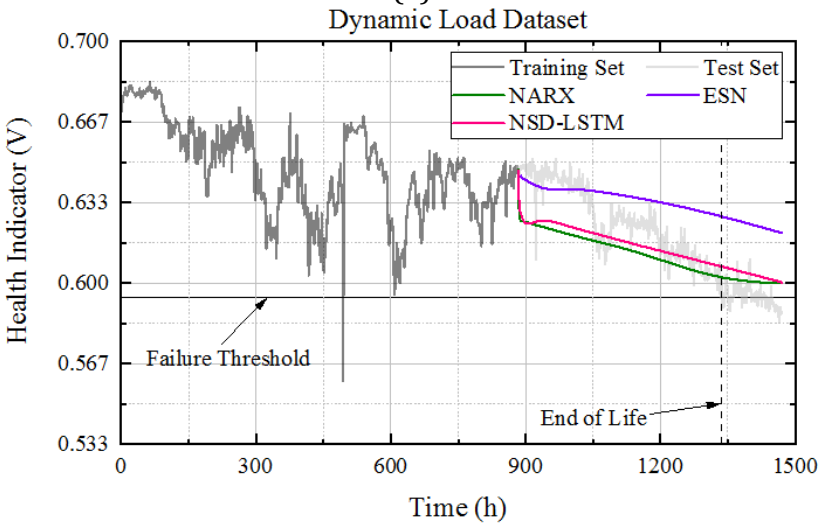

(b)

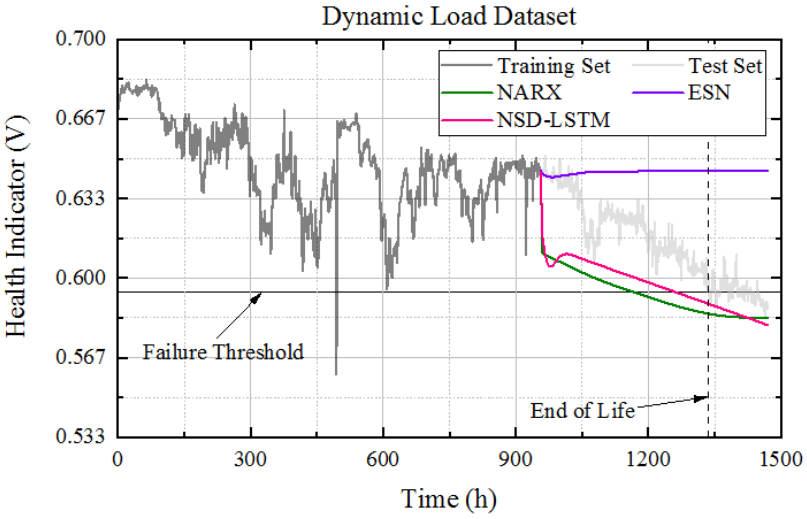

(c)

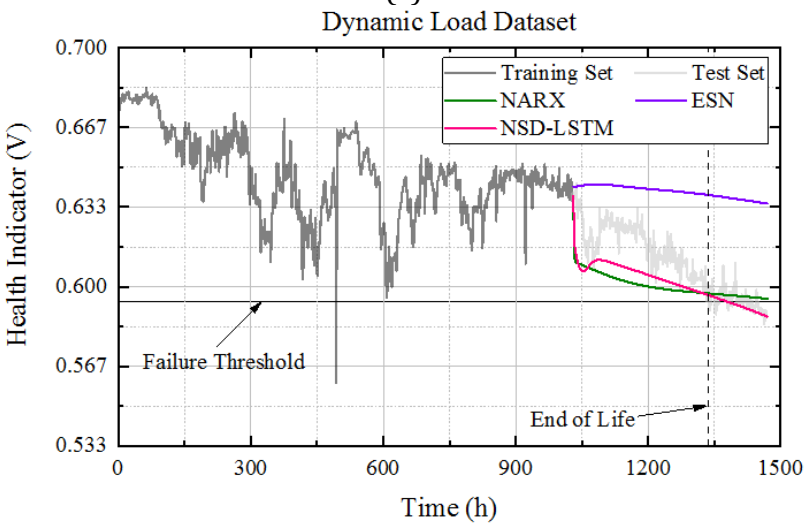

(d)

Figure 3.11 Comparison experiment of degradation trend predictions in the dynamic-load dataset, among them, (a), (b), (c) and (d) represent the results of split points 1, 2, 3, and 4, respectively.

This phenomenon is more pronounced at split points 3 and 4. Compared with the previous two models, the prediction results of the NSD-LSTM model show the best consistency and are closest to the test set. Especially at split points 3 and 4, the predicted trends of NARX and NSD-LSTM seems to be similar in the early stage of prediction, and both show a rapid decline thanks to the guidance of the NS. Then, the well-trained LSTM in NSD-LSTM provides more “long-term memory” information about the degradation trend for the prediction process, which enables NSD-LSTM to maintain stable and consistent trend prediction performance.

In the comparison experiment on the constant-load dataset, as shown in Table 3.5 and Figure 3.12 (a) and (b), the consistency of the NARX model is the worst, the consistency of the NSD-LSTM model is better. It is of interest that the ESN model performs slightly better than the NSD-LSTM model in terms of consistency, but unfortunately, the prediction accuracy of the ESN model does not decrease as expected

as the operating time increases. Specifically, at split point 1, the RE performances of the NARX and NSD-LSTM model are similar, while ESN model performs better. At split point 2, the prediction performance of all three models decreases, with the NARX model being the worst. At split point 3 and split point 4, both the NARX model and the NSD-LSTM model show a trend of gradually improving prediction accuracy, with the NSD-LSTM being more significant. Comparatively, the ESN model performs poorly.

Split point	Operating time (h)	RUL (h)				RE (%)		
		Actual	NARX	ESN	NSD-LSTM	NARX	ESN	NSD-LSTM
1	5580.5	3002.8	2369.8	2778.8	3549.9	21.08	7.46	18.22
2	6078.3	2505.0	4645.9	2024.5	3699.8	85.47	19.18	47.70
3	6573.2	2010.1	3271.9	1462.3	1786.2	62.77	27.25	11.14
4	7151.6	1431.7	1252.6	1052.6	1431.9	12.51	26.48	0.01

Table 3.5 Comparison experiments in the constant-load.

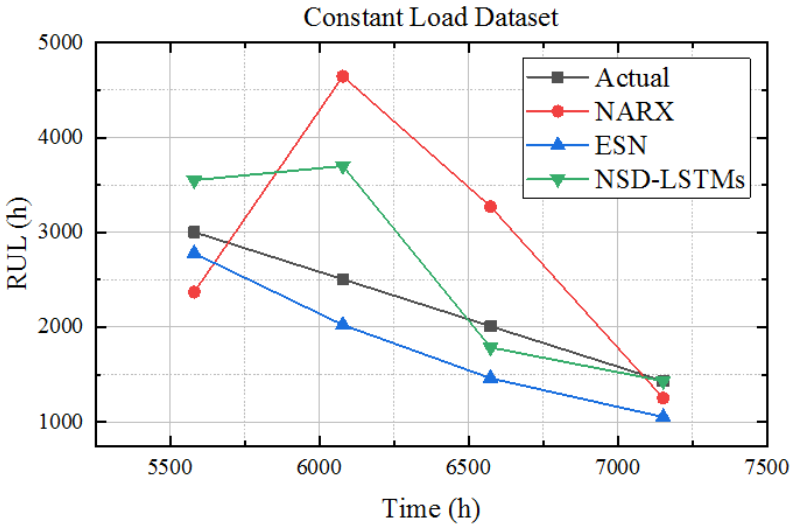

(a)

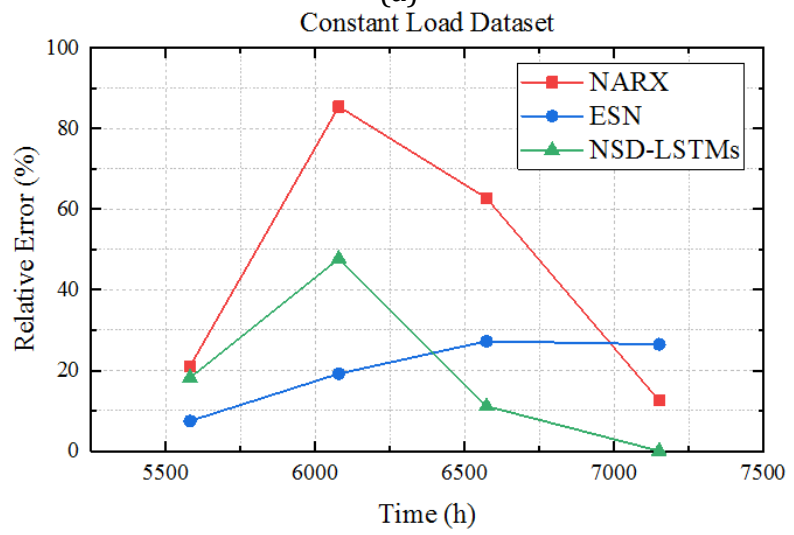

(b)

Figure 3.12 Comparison experiment of RUL estimations in the constant-load dataset, (a) estimated RULs; (b) relative errors.

In the comparison experiment on the dynamic-load dataset, as shown in Table 3.6 and Figure 3.13 (a) and (b), the consistency of the ESN model is the worst, the consistency of the NARX model is slightly better, and the consistency of the NSD-LSTM model is the best. Specifically, at split point 1, the performances of the three models are similar. At split point 2, the RUL estimated by the ESN model has increased significantly, and the RE has exceeded 130%. What is more serious is that at split point 3 and split point 4, the REs of the ESN model have exceeded 590% and 410%, respectively. In contrast, the RULs estimated by the NARX and NSD-LSTM models fluctuate close to the real RULs. The NARX model performs worse than the NSD-LSTM model at all four split points. Especially at split point 2, the RE of NARX exceeds 200%. In summary, compared with the other two models, the NSD-LSTM model is capable of reproducing the short-term and long-term degradation behaviors and provides a more consistent prediction of the degradation trends. The RULs estimated by the NSD-LSTM model are more reliable, with enhanced robustness.

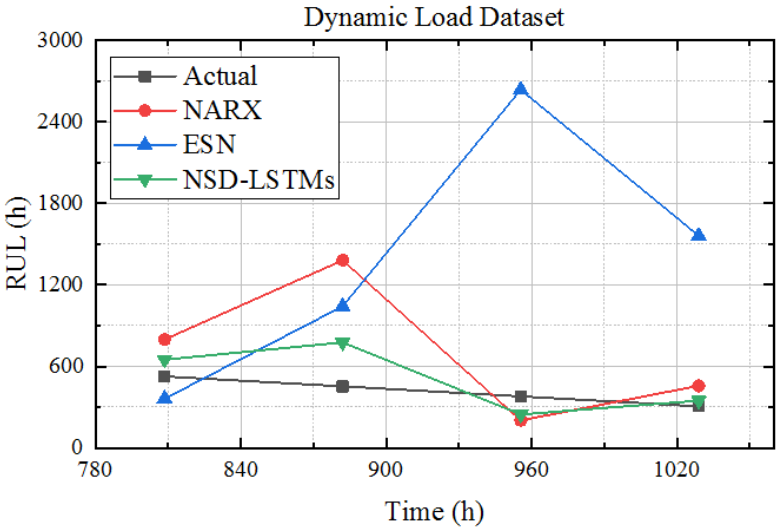

(a)

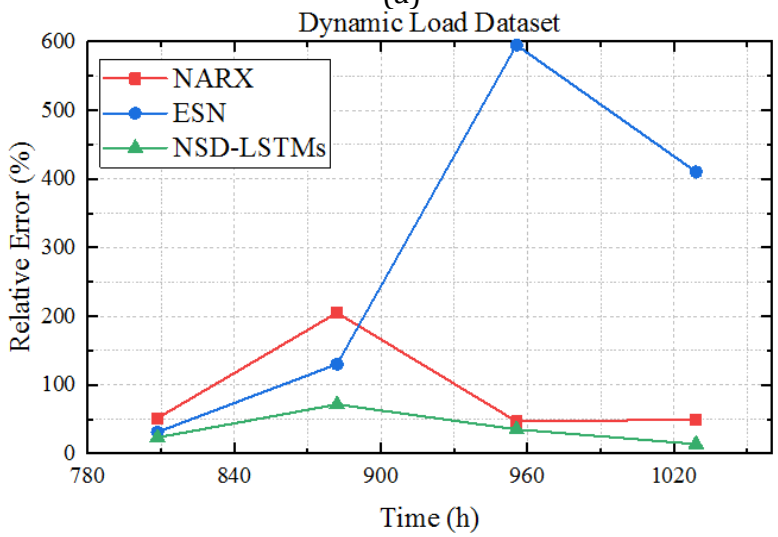

(b)

Figure 3.13 Comparison experiment of RUL estimations in the dynamic-load dataset, (a) estimated RULs; (b) relative errors.

Split Point	Operating time (h)	RUL (h)				RE (%)		
		Actual	NARX	ESN	NSD-LSTM	NARX	ESN	NSD-LSTM
1	808.5	526.5	798.0	361.5	649.5	51.57	31.34	23.36
2	882.0	453.0	1381.5	1042.5	777.0	204.97	130.13	71.52
3	955.5	379.5	202.5	2637.0	246.0	46.64	594.86	35.18
4	1029.0	306.0	457.5	1561.5	348.0	49.51	410.29	13.73

Table 3.6 Comparison experiments in the dynamic-load.

3.5. Discussion

In this Chapter, the fuel cell prognostics are discussed and the proposed NSD-LSTM model shows a satisfactory prediction performance. Especially, it outperforms other state-of-the-art prognostics methods in some cases, which can be considered to arise from the following factors.

(1) In comparison experiments, the ESN model effectively identifies a part of the degradation trend, especially 100-200 hours before the prediction starting point. However, due to the effect of system disturbances/recoverable faults, a short-term trend may differ significantly from the inherent degradation trend. This results in poor prediction performance, especially in the dynamic load dataset.

(2) In the comparison experiments, the NARX model predicts similar degradation trends as the NSD-LSTM model. This is due to the fact that both use the same NS, which also illustrates the availability and consistency of NS in guiding predictions.

(3) The prediction accuracy of the NARX model is slightly lower, which is due to the influence of the historical data interval on its prediction range. Especially, the phenomenon is more significant in Figure 3.11 (d). Along with the prediction time (step), the degradation trend predicted by NARX gradually converges to the horizontal line, which leads to the predicted RUL abnormally higher. In contrast, the NSD-LSTM can “remember” and “inherit” the historical degradation trend to break the numerical interval limitation.

In summary, the navigation sequence generated by the ARIMAX model is fed into the well-trained LSTM to reinforce the performance of long-term degradation trend prediction and RUL estimation. From the comparison experiment results, the main contributions are summarized as follows.

(1) Compared with the existing LSTM-based prognostics models, the NSD-LSTM model achieves credible degradation prediction with longer prediction horizons. Based on the long-term prediction, RUL estimation is further realized.

(2) Thanks to the guidance and improvement of navigation sequence, the NSD-LSTM gains the ability to break the numerical interval of historical-based training set, and the predicted long-term degradation trends are consistent.

(3) Both the long-term and the short-term degradation behaviors are considered comprehensively in the fuel cell prognostics. Due to this property, better degradation prediction and RUL estimation results are obtained compared to several state-of-the-art methods.

Furthermore, it is worth noting that average cell voltage is to some extent not the optimal health indicator. Especially for the case of variable load conditions, it is necessary to extract reliable health indicators, e.g., physically interpretable, monotonic, with significant trends. Meanwhile, the accuracy and horizon of the prognostics deserve to be enhanced.

4. Hybrid prognostics based on degradation behavior model and symbolic-LSTM

4.1. Introduction

PHM has the ability to improve FC durability and is considered as one of the superior solutions [27]. In PHM, the accuracy of prognostics plays a deterministic role in the timing of maintenance/control deployment and affects the effectiveness of health management. Prognostics provides the basis for the "Predict"–"Maintain" strategy considered as an alternative of the "Failure"-"Replace" strategy [31]. The former is considered to be better not only to improve the durability but also to reduce the maintenance cost [19]. Accordingly, for FC ageing prognostics, the core task involves refining the HI, predicting the SoH and/or the RUL [10]. For FC operating in constant conditions, some measurements (such as stack voltage [33, 35]) can be directly assigned as HI. On the other hand, dynamic operating conditions not only affect the transient response of PEMFC performance [24], but also make it difficult to evaluate directly the degradation from measurements. As a result, a suitable HI needs to be extracted for long-term ageing prognostics under dynamic conditions. Whereas, facing the complex operating conditions in transportation applications, it is still challenging to effectively decouple the system dynamics from the ageing effects and obtain physically interpretable HI.

In the phase of SoH/RUL prediction, the performance of model-free or data-driven based methods is encouraging. This is due to the fact that such methods adeptly learn and predict the trend characteristics of HI [31]. In particular, methods in LSTM framework have demonstrated their strong performance in short-term SoH prediction. However, LSTM performance becomes unsatisfactory with increased prediction horizon length which is observed and indicated in previous Chapter. Interestingly, the cause of this issue may stem from the powerful "memory" ability of the LSTM, which incorrectly records irrelevant features in the training set. In general, the LSTM based prognostics model still need to be improved in HI long-term prediction.

Another key challenge for developing credible FC prognostics tools, especially for PEMFC applied in transportation, is the scarcity of long-term ageing data. A recent review [92] comprehensively reports state-of-the-art durability experimental methods for vehicle-oriented PEMFC. The use of the Accelerated Stress Test (AST) not only enables the assessment of FC lifetime, but also effectively reduces the experimental cost and time.

To tackle the above issues, this Chapter proposes a hybrid prognostics strategy for PEMFC in transportation applications, consisting of model-based HI extraction and

model-free RUL prediction. Specifically, a time-varying degradation model based on the FC electrochemical mechanism is developed to track the load dynamics. The model parameters are identified in variable width intervals, specifying the equivalent resistance and the reconstructed virtual-constant power as HIs, respectively. In the phase of RUL prediction, a reduced-dimensional symbolic representation based LSTM model is used to predict the possible trends of HI. Subsequently, a series of predicted trends form a probability density distribution and RUL is calculated. Finally, the proposed method is validated using a vehicle application-oriented long-term AST dataset.

The remainder of this Chapter is as follows: Section 4.2 presents the proposed degradation mechanism model. In Section 4.3, the RUL prediction model and the hybrid prognostics strategy are talked about. The experiments used to validate the method are described in Section 4.4. Section 4.5 summarizes the prognostics results. The Chapter is finally concluded in Section 4.6.

4.2. Model-based dynamics health indicator extraction

4.2.1. Degradation mechanism model

Utilizing electrochemical mechanisms such as the models based on polarization curves has been recognized as effective to explain FC voltage losses [117]. The polarization curve model contains the voltage losses due to activation (V_{act}), ohmic (V_r), and concentration (V_{conc}), and is generally expressed as

$$E_{cell} = E_{rev} - v = E_{rev} - V_{act} - V_r - V_{conc} \tag{4.1}$$

where E_{cell} is the cell voltage, E_{rev} is the reversible open-circuit voltage, v is the global overpotential. A typical polarization curve model is for single cell modelling and generalizes to an n-cell stack level ($E_{stack} = n \cdot E_{cell}$) ignoring inter-cell differences. However, this model is generally suitable for portraying a PEMFC voltage response to static operating conditions and is unable to track transient voltage evolutions in dynamic conditions.

A typical electrochemical reaction interface is depicted in Figure 4.1. The electrochemical characteristics of the reaction interface are represented by using a resistor (R_{dyn}) and a capacitor (C_{dl}) in parallel, as in Figure 4.1 (a). Here, R_{dyn} is called the dynamic resistor to quantify the electrochemical reaction dynamic characteristics. Generally, these dynamics include not only the charge transport caused by electrochemical reaction kinetics, but also the mass transport due to reactant/product concentration differences. Further R_{dyn} can be decomposed into two resistors R_{act} and R_{conc}. In this case, R_{act} (a. k. a., Faradaic resistor) models the charge transport, which corresponds to the linear part of the activation overpotential. Similarly, R_{conc} is used to simplify the Warburg element to simulate the mass transport, which corresponds to the

linear part of the concentration overpotential. R_r is the resistor corresponding to ohmic losses.

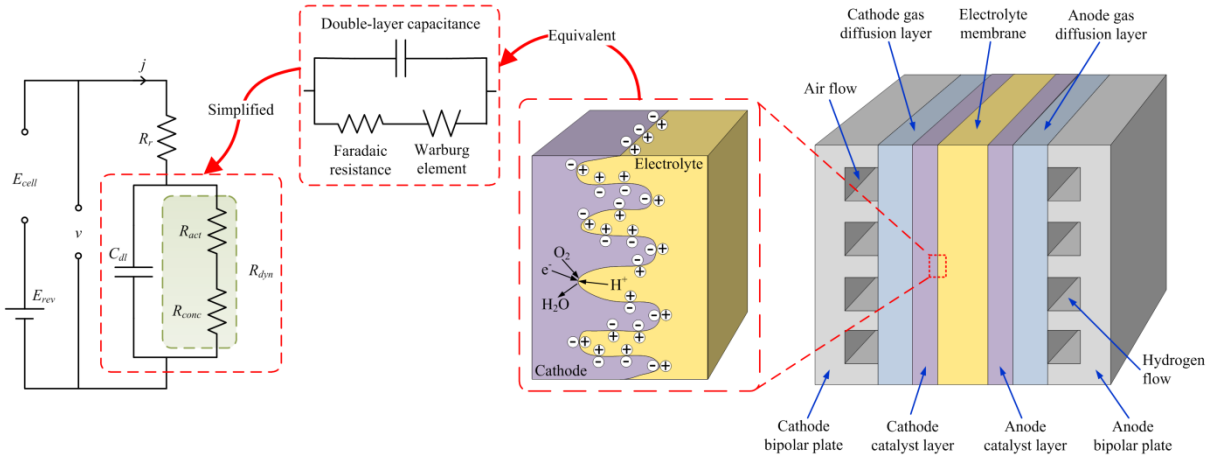

(a) (b)

Figure 4.1 PEMFC electrochemical mechanism schematic: (a) equivalent circuit model; (b) physical representation of an electrochemical reaction interface.

Based on this, the three voltage losses can be refined by using the following equations,

$$\begin{cases} V_{act} = \overbrace{jR_{act}}^{\text{linear}} + \overbrace{\dfrac{RT}{\alpha_{a+c}F} ln\left(\dfrac{j+j_{loss}}{j_{exch}}\right)}^{\text{non-linear}} \\ V_R = jR_r \\ V_{conc} = \underbrace{jR_{conc}}_{\text{linear}} - \underbrace{\dfrac{RT}{\beta_{a+c}F} ln\left(\dfrac{j_{max}-j}{j_{max}}\right)}_{\text{non-linear}} \end{cases} \tag{4.2}$$

where, j is the stack current density, j_{loss} is the crossover current density, j_{exch} is the exchange current density; j_{max} is limiting current density. R is Molar gas constant (8.3145 J/mol/K), F is Faraday constant (96485 C/mol). α_{a+c} is the transfer coefficient, β_{a+c} is a parameter related to the number of electrons transferred in the overall reaction. Both α_{a+c} and β_{a+c} combine the effects of the anode and the cathode. T is the operating temperature (thermodynamic temperature) of the cell. Further, R_r and R_{dyn} are combined as the equivalent resistance (R_{equ}), which represents the overall resistance of the cell, as

$$R_r + R_{act} + R_{conc} = R_r + R_{dyn} = R_{equ} \tag{4.3}$$

In addition, C_{dl} is called the double-layer capacitor, which corresponds to the capacitance characteristics of the reaction interface. As in Figure 4.1 (b), in the electrochemical reaction, significant charge separation occurs at the reaction interface, with electrons and ions accumulating respectively on the electrode and electrolyte sides. The reaction interface behaves like a capacitor due to the charge separation phenomenon. As shown in the figure, the electrode/electrolyte interface is not smooth, which makes C_{dl} evident and not ignorable [112].

In general, the output voltage/power shows decreases along with the PEMFC degradation. In the case of the equivalent circuit modelling, as in Figure 4.1(a), the

decrease in E_{cell} can be attributed to the effect of time-varying parameters such as R_r, R_{dyn}, C_{dl} and E_{rev}. These parameters can be candidates for health indicators in Section 4.2.2. There are diverse methods to achieve degradation model parameter identification, such as polarization curve-fitting. The direct use of classical polarization curve-fitting is reliable at constant load conditions. This Chapter aims to identify the dynamic behaviour of the fuel cell, especially at load switching moments. Thus, to identify the time-varying dynamics of the equivalent circuit in Figure 4.1(a), the following equation is utilized.

$$v(t) + R_{dyn}C_{dl}\frac{dv(t)}{dt} = \left(R_r + R_{dyn}\right)j(t) + R_rR_{dyn}C_{dl}\frac{dj(t)}{dt} \tag{4.4}$$

Further, the one-sided Laplace transform of the left and right sides of equation (4.4) can be done to obtain the system transfer function, as

$$H(s) = \frac{V(s)}{J(s)} = \frac{R_r s + \left(R_r + R_{dyn}\right)/\left(R_{dyn}C_{dl}\right)}{s + 1/\left(R_{dyn}C_{dl}\right)} = \frac{q_1 s + q_2}{s + p_1} \tag{4.5}$$

where $H(s)$ is considered as a single-input, single-output system. p_1 represents the Laplace variable of the denominator polynomial, and q_1 and q_2 represent the Laplace variables of the numerator polynomial. By feeding the data of both temporal input $j(t)$ and output $v(t)$, the model parameters p_1, q_1 and q_2 can be identified. The model parameters R_r, R_{dyn}, C_{dl} and E_{rev} can further be deduced. The parameter identification process is summarized as follows.

In general, the refined choice of filter $L(s)$ is used to cope with the disturbances embedded in the system when estimating the system variables [118].

$$L(s) = \frac{1}{A(s)} \tag{4.6}$$

In fact, $A(s)$ is the denominator of $H(s)$, for which the unknown part is replaced by the estimated value. Based on this, the following equation is obtained after filtering equation (4.4).

$$\begin{aligned} L(s)v'(t) &= -p_1L(s)v(t) + q_1L(s)j'(t) + q_2L(s)j(t) + L(s)e(t) \\ &= \varphi^T(t)\theta + L(s)e(t) \end{aligned} \tag{4.7}$$

where $v'(t)$ and $j'(t)$ correspond to the first order derivatives of the variables, $e(t)$ is the disturbance of the system, and $\varphi(t)$ and θ are as follows,

$$\begin{cases} \varphi(t) = [-L(s)v(t)\ ,\ \ L(s)j'(t)\ ,\ \ L(s)j(t)]^T \\ \theta = [p_1\ ,\ \ q_1\ ,\ \ q_2]^T \end{cases} \tag{4.8}$$

Considering that typically $e(t)$ is not necessarily white noise, the Instrumental Variable (IV) method is chosen in order to reduce the estimation bias. The predicted output $\hat{v}(t)$ will constitute the instrument vector $\zeta(t)$,

$$\zeta^T(t) = [-L(s)\hat{v}(t)\ ,\ \ L(s)j'(t)\ ,\ \ L(s)j(t)] \tag{4.9}$$

The parameters are subsequently estimated using the following equation,

$$\hat{\theta} = \left[\sum_{i=1}^{N}\zeta^T(t_i)\varphi(t_i)\right]^{-1}\sum_{i=1}^{N}\zeta^T(t_i)[L(s)v'(t_i)] \tag{4.10}$$

where $\hat{\theta}$ represents the estimated parameters [118].

4.2.2. Health indicator extraction based on variable width division

The electrochemical mechanism-based degradation model described above has the ability to characterize the short-term dynamics. Concerning the long-term ageing, the electrochemical characteristics of FC change over time and some ageing-related parameters can be used to reflect the FC long-term evolution. A HI extraction method based on variable width division is therefore proposed in this Chapter, as in Figure 4.2. Specifically, the samples of current density, cell temperature and cell voltage within a time slot are set as inputs, while the degradation model parameters are set as model identification outputs among which health indicators are further selected. It is worth mentioning that cell temperature has a relationship with the thermal characteristics, and affects the power output performance/degradation behaviour of the stack/system [119]. Considering the generalization of the method, several of the measurements are difficult to obtain in some cases (e.g., dead-ended mode). Moreover, at this moment, air pressure and stoichiometry are highly coupled to temperature [120]. Therefore, the use of cell temperature as an input variable is beneficial to profile the factors affecting durability that are not covered by the electrochemical mechanistic model.

In general, all parameters in Equations (4.1) to (4.3) are time-varying except for the Molar gas constant (R) and Faraday constant (F). Identifying all time-varying parameters is beneficial to model fuel cells comprehensively, but leads to higher computational costs and difficulty in practical deployment. One potential solution is to simplify appropriately the model by making some of the variable parameters constant and considering the ageing effects using the remaining variable parameters.

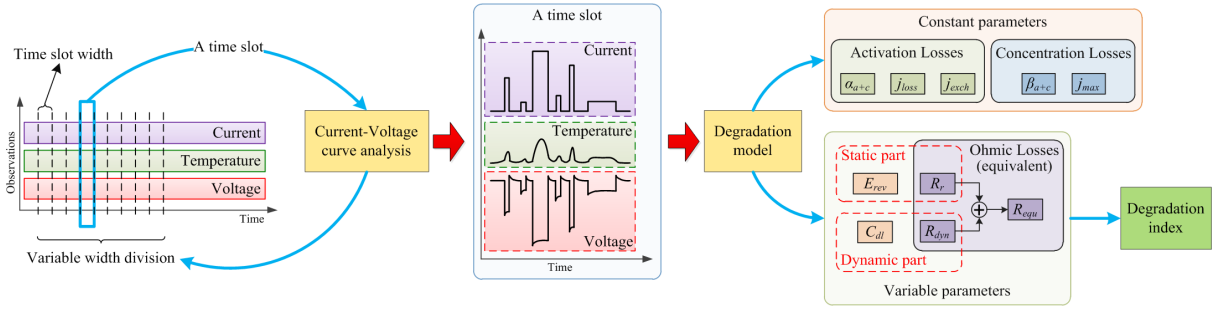

Figure 4.2 Schematic of variable width division-based health indicator extraction.

As the FC ageing is relatively slow, the ageing-related parameters can be considered constant in short-term time slots (hourly level). The time slot width should be set in the way that the data within the time slot contain sufficient system dynamics for model identification. As shown on the right side of Figure 4.2, the variable parameters, i.e., E_{rev}, C_{dl}, R_r, and R_{equ} are identified in each time slot via the model identification procedure presented in Equations (4.6) to (4.10). It is worth mentioning that in some studies (e.g., [27]), the constant parameters considered in this Chapter are also used to indicate degradation. Nevertheless, most of them are difficult to model precisely or can be considered combined in variable parameters to simplify the model properly. For

instance, the impact of degradation on j_{loss} can be reflected and quantified using E_{rev}. Thus, j_{loss} is considered as a constant while E_{rev} is set as a variable parameter.

Once identified, the parameters that demonstrate evident time-varying characteristics can be considered as the candidates for HI. By further analyzing the trendiness/smoothness of the candidates, the HI suitable for prognostics is selected. In addition, it is possible to consider bringing all the identified parameters into Equations (4.1)-(4.3) and replacing the original dynamic operating current density with a virtual constant current. Accordingly, the virtual steady-state voltage and power can be calculated. It is thus possible to analyze the output power drop as HI at different loads, especially at nominal power/full load.

4.3. Model-free remaining useful life prediction

4.3.1. Symbolic-based fuel cell health indicator conversion

The fuel cell health indicator conversion method used in this Chapter, called adaptive Brownian bridge-based aggregation, allows the representation and reconstruction of a health indicator. ABBA uses increments in time and value coordinates to capture data trends in health indicator without preprocessing [121]. The implementation of the representation consists of two stages: compression and digitization.

The core of compression is to divide the n-dimensional health indicator $X = (x_1, x_2, \cdots, x_n) \in \mathbb{R}^n$ into m segments $Q = (Q_1, Q_2, \cdots, Q_m) \in \mathbb{R}^m$. Then the compression is achieved by approximating X with straight polygonal chain. To do this, ABBA selects $m+1$ breakpoints $\left(\tilde{x}_{i_1} = x_1 < \tilde{x}_{i_2} < \cdots < \tilde{x}_{i_{m+1}} = x_n\right)$ in X. The i_h is the time index corresponding to the h-th $(h = 1,2,\cdots,m+1)$ breakpoint. So the j-th $(j = 1,2,\cdots,m)$ segment can be written as $Q_j = \left(\tilde{x}_{i_j}, \tilde{x}_{i_j+1}, \cdots, \tilde{x}_{i_{j+1}}\right)$. In this segment, time direction increment and numerical direction increment are $len_j = i_{j+1} - i_j$ and $inc_j = \tilde{x}_{i_{j+1}} - \tilde{x}_{i_j}$ respectively. Further, the squared Euclidean distance of the values in Q_j from the polygonal chain is bounded by $\left(len_j - 1\right) \cdot tol^2$, as

$$\sum_{i=i_j}^{i_{j+1}} \left(\underbrace{\tilde{x}_{i_j} + inc_j \cdot \frac{i - i_j}{len_j}}_{\text{linear approximation}} - \underbrace{x_i}_{\substack{\text{actual} \\ \text{value}}} \right)^2 \leq \left(len_j - 1\right) \cdot tol^2 \tag{4.11}$$

From the inequation, the compression rate which is represented by len_j can be regulated by setting the tolerance parameter tol. Usually, this value ranges from 0.05 to 0.5 and a large tol indicates a coarser compression process [121].

Subsequently, the appropriate time and value increments form a tuple $D_j = \left(len_j, inc_j\right)$. Thus, the time series X is represented by $2 \times m$-dimensional tuples-set D as

$$X = (x_1, x_2, \cdots, x_n) \Rightarrow D = [(len_1, inc_1), (len_2, inc_2), \cdots, (len_m, inc_m)] \tag{4.12}$$

Before implementing digitization, each tuple needs to be standardized and scaled. Specifically, the scaling factors ω_{len} and ω_{inc} are introduced, which represent the length and incremental weights, respectively. Both can take values between 0 and 1 and satisfy $\omega_{len} + \omega_{inc} = 1$. The scaled set of tuples $\overline{D}$ can be calculated by

$$\overline{D} = \begin{bmatrix} \left(\omega_{len} \cdot \frac{len_1}{\sigma_{len}}, \omega_{inc} \cdot \frac{inc_1}{\sigma_{inc}}\right), \left(\omega_{len} \cdot \frac{len_2}{\sigma_{len}}, \omega_{inc} \cdot \frac{inc_2}{\sigma_{inc}}\right), \\ \cdots, \left(\omega_{len} \cdot \frac{len_m}{\sigma_{len}}, \omega_{inc} \cdot \frac{inc_m}{\sigma_{inc}}\right) \end{bmatrix} \tag{4.13}$$

where σ_{len} and σ_{inc} are the standard deviation of the segment lengths and the segment increments, respectively.

The first step of digitization is to further assign $\overline{D}$ to k clusters $S = (S_1, S_2, \cdots, S_k)$ by minimizing the Within-cluster Sum of Squares (WCSS)

$$WCSS = \arg\min_{\overline{D}_l \in S} \sum_{l=1}^{k} \sum_{\overline{D}_l \in S_l} \left\| \overline{D}_l - \overline{\mu}_l \right\|^2 \tag{4.14}$$

where, the "$\arg\min_{x \in S} f(x)$" represent arguments x for which $f(x)$ attains its smallest value. The $\|\cdot\|^2$ denotes the Euclidean norm, and $\overline{\mu}_l$ is the center of the l-th ($l = 1,2, \cdots, k$) cluster S_l. Further, as in Equation (4.15), k letter symbols can be used to represent each cluster separately. In practical deployments, the value of k can be specified manually, as will be discussed in detail in the subsequent numerical example.

$$\overline{D} \Rightarrow S = (S_1, S_2, \cdots, S_k) \Rightarrow L = \underbrace{(a, b, c, \cdots, k)}_{k \text{ symbols}} \tag{4.15}$$

The second step of the digitization is to use the letters in L to replace the tuples in the corresponding clusters in D so that a string A can be obtained:

$$D \Rightarrow A = (sy_1, sy_2, \cdots, sy_m) \tag{4.16}$$

where $sy_j \in L$. So far ABBA converts an n-dimensional health indicator into an m-letter one. The digitalized data maintains meaningful information in the original health indicator and is more lightweight, which is beneficial for the rapid deployment of a neural network in the following step. On the other hand, in contrast to the representation, the reconstruction means that ABBA converts symbolic string back to a health indicator. Reconstruction can be considered as the inverse process of representation and applies a similar mathematical approach [121].

A numerical example is shown in Figure 4.3, using ABBA to represent the fuel cell health indicator. $tol = 0.1$ is set in the compression phase and ABBA divides the health indicator into 21 segments. Subsequently, $\omega_{len} = \omega_{inc} = 0.5$, i.e., the segment lengths and segment increments are weighted equally. Two clusters ($k = 2$) are used in Figure 4.3 (a), and the obtained symbols are represented as "abbbbbbbbbbbbbbabbbbb". Then, three clusters ($k = 3$) are used in Figure 4.3 (b), and the obtained symbols are represented as "cdedededdedededcdeded". Figure 4.3 (c) shows the process of ABBA implementation when $k = 3$. It is seen that more detailed features can be depicted with a bigger k value.

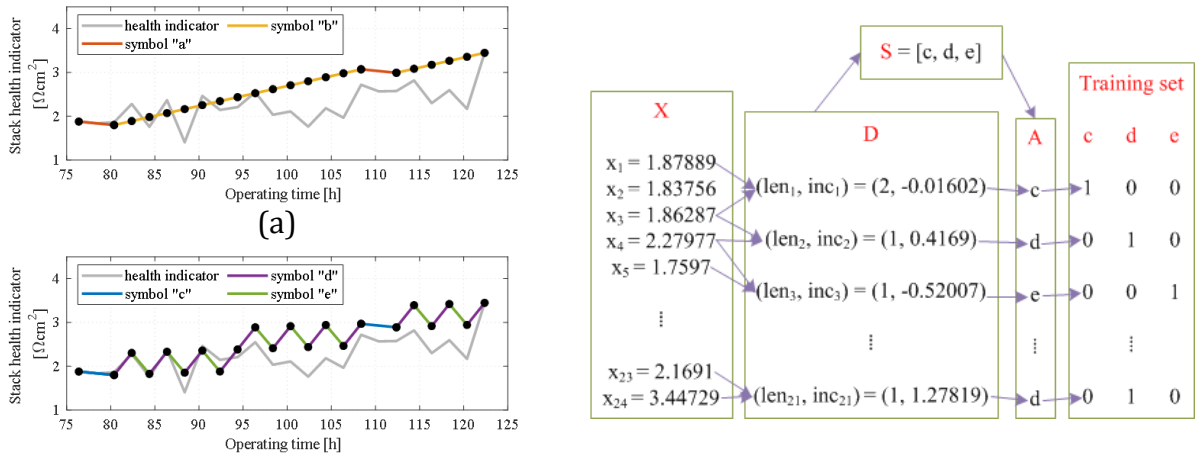

Figure 4.3 Symbolic representation of the time series, (a) setting to k=2 (2 symbols), the time series representation is "abbbbbbbbbbbbbbabbbbb"; (b) setting to k=3 (3 symbols), the time series representation is "cdedededdedededcdeded"; (c) the implementation of ABBA at k=3.

4.3.2. ABBA-LSTM

The Raw-LSTM (a. k. a., Vanilla-LSTM) encounters performance decreasing in long-term prediction, especially when there is a lack of training data concerning the prediction horizon [109]. In the stage of SoH prediction, we use an LSTM model with adaptive Brownian bridge-based aggregation (ABBA-LSTM) to tackle this issue. The core idea is to express the original data with reduced dimensional symbols/letters to improve the sensitivity of Raw-LSTM to trend features. Specifically, ABBA-LSTM can be divided into three parts: representation, prediction, and reconstruction, as in Figure 4.4.

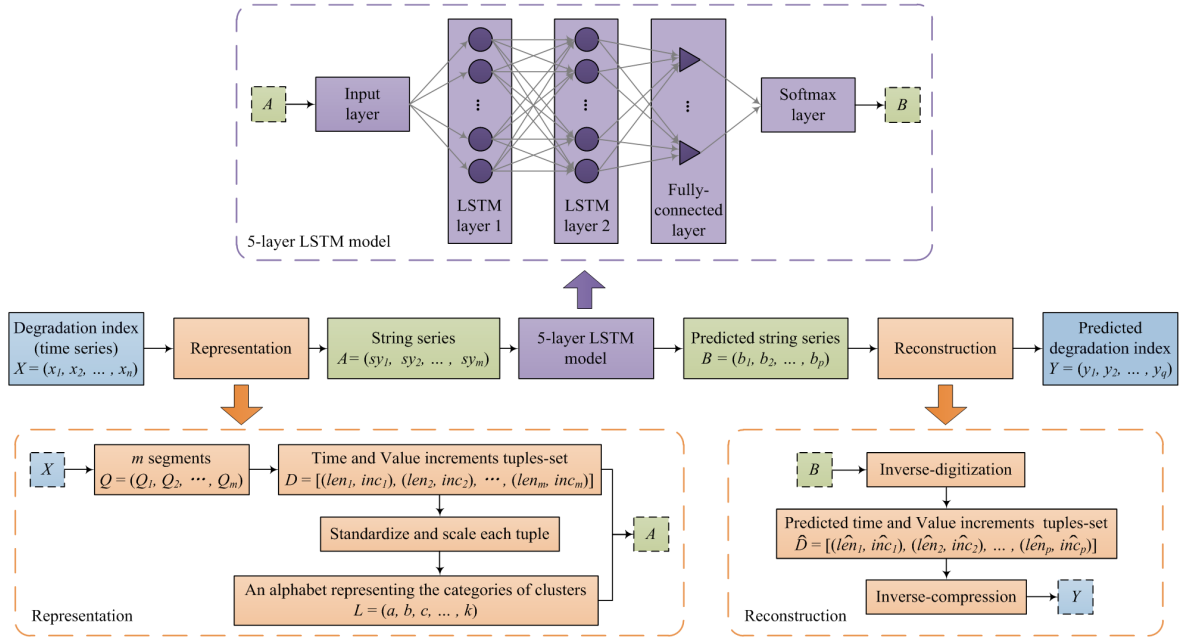

Figure 4.4 Flowchart of the proposed ABBA-LSTM prognostics model.

(1) Representation

As described in section 4.3.2, there are two steps. First, Compression converts an n-dimensional historical HI (time series X) into a tuples-set (D). Second, in Digitization, by standardization and scaling, an alphabet set (L) corresponding to k clustering categories is constructed. The tuples in D are expressed using the letters in L to obtain the character series A of length m.

(2) Prediction

In the prediction part, a 5-layer LSTM model is utilized, where the input is the character series A. After two LSTM layers, a fully connected layer and a Softmax layer, the output character series B contains the predictions for p time steps.

(3) Reconstruction

The predicted character series needs to be recovered as a time series before it is used for FC prognostics, and this part is regarded as the inverse process of representation. Converting character series B to predicted time series Y is realized by Inverse-digitization and Inverse-compression.

To describe this process more clearly, a series of notation marks involved in the ABBA-LSTM prognostics model are shown in Table 4.1. The detailed operations listed in Figure 4.4 for each step of ABBA can be found in Section 4.3.1.

Type	Notation of sets	Remark
Time series	$X = (x_1, x_2, \cdots, x_n) \in \mathbb{R}^n$	Historical health indicator
Compression	$D = \begin{bmatrix} (len_1, inc_1), (len_2, inc_2) \\ , \cdots, (len_m, inc_m) \end{bmatrix} \in \mathbb{R}^{2\times m}$	Time and numerical increment tuples-set
Digitization	$L = (a, b, c, \cdots, k)$	Alphabet set representing clusters' categories
Digitization	$A = (sy_1, sy_2, \cdots, sy_m)$, where $sy_i \in L$ $(i = 1, \ldots, m)$	m-dimensional character series
Prediction	$B = (b_1, b_2, \cdots, b_p)$ where $b_j \in L$ $(j = 1, \ldots, p)$	p-dimensional predicted set of characters
Inverse-digitization	$\widehat{D} = \begin{bmatrix} (\hat{len}_1, \hat{inc}_1), (\hat{len}_2, \hat{inc}_2) \\ , \cdots, (\hat{len}_p, \hat{inc}_p) \end{bmatrix} \in \mathbb{R}^{2\times p}$	Predicted increments tuples-set
Inverse-compression	$Y = (y_1, y_2, \cdots y_q) \in \mathbb{R}^q$	Predicted health indicator (q time steps)

Table 4.1 Notation marks during health indicator series conversion

4.3.3. Hybrid prognostics strategy

The central goal of hybrid prognostics is to predict RUL. The failure threshold directly determines the EoL of fuel cells. In 2011, the United States Department of Energy defined EoL as a 10% loss of initial performance, which is suitable for constant current operating conditions. However, when a PEMFC operates in dynamic load conditions, there is still no agreement on the definition of the FT [30]. In some cases, different FTs lead to significantly different RULs [92]. Furthermore, desirable FTs should be closely

related to the application. It is not optimal to have a single/uniform FT for fuel cells from different applications.

A Probable Failure Range (PFR) and a Calculable Failure Range (CFR) are proposed in this Chapter. Specifically, as shown in Figure 4.5 (a), the prediction starting point (t_0) and the extreme point of recoverable fault (t_{limit}) divide the ageing data into three parts: training, prognostics, and invalid data. Before t_0 is considered as the observed historical data (a. k. a., training set), which is used to train the prognostics model. Then between t_0 and t_{limit} is the prognostics zone (a. k. a., test set). It is worth noting that the operation time corresponding to t_{limit} is usually less than or equal to the one corresponding to t_{end} (complete failure point or data ending point). In the case where t_{limit} is not equal to t_{end}, the part between the two points is defined as invalid data. This is because the performance recovery that occurs after t_{limit} is not sufficiently reliable and may cause serious errors in the prognostics. The range between the expected earliest failure point (t_{a_1}) and the t_{end} is considered as PFR, and the range between the t_{a_1} and the t_{limit} is considered as CFR.

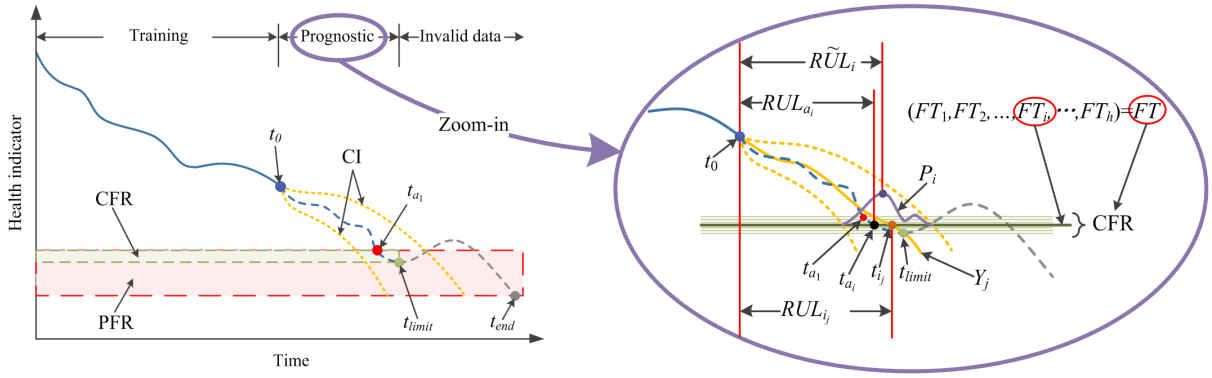

(a) (b)

Figure 4.5 Schematic of hybrid prognostics: (a) segmentation of health indicator (data set), and failure ranges; (b) when prediction starting point is t_0, zoom-in prognostics part and predict remaining useful life.

As a fuel cell runs, fresh observations are constantly acquired. The t_0, which divides the "history" from the "future", will also be updated to deploy the next-round of prognostics. For a particular prediction starting time point, the zoom-in illustration of the prognostics part is shown in Figure 4.5 (b). By setting l random initial weight parameters, the ABBA-LSTM model can output a series of predicted health indicator $\hat{Y} = (Y_1, Y_2, \ldots, Y_l)$, where $Y_j \in \mathbb{R}^q$ is the j-th ($j = 1,2, \ldots, l$) predicted degradation trend. The CFR contains h failure thresholds $FT = (FT_1, FT_2, \ldots, FT_h)$.

(1) For the i-th ($i = 1, 2, \ldots, h$) failure threshold FT_i

Based on the health indicator series $\hat{Y}$ and FT_i, a series of RUL (RUL_i) can be calculated as

$$\begin{cases} RUL_i = \left(RUL_{i_1}, RUL_{i_2}, \ldots, RUL_{i_j}, \ldots, RUL_{i_l}\right) \in \mathbb{R}^l \\ RUL_{i_j} = t_{i_j} - t_0 \\ RUL_{a_i} = t_{a_i} - t_0 \end{cases} \tag{4.17}$$

where RUL_{i_j} is the j-th ($j = 1,2,\dots,l$) element in RUL_i. t_{i_j} is the j-th predicted end-of-life at FT_i, i.e., the operation time at the crossing point of the j-th health indicator Y_j and FT_i. t_{a_i} actual end-of-life at FT_i, i.e., is the operation time at the crossing point of actual HI and FT_i. RUL_{a_i} is the actual RUL value. Estimate the probability density distribution (P_i) based on the RUL series RUL_i, as

$$f\left(RUL_{P_i}\right) = P_i \tag{4.18}$$

where RUL_{P_i} corresponds to the RUL values of the horizontal coordinate of P_i. The final predicted RUL value ($\widetilde{RUL}_i$) at FT_i can be obtained as

$$\widetilde{RUL}_i = \underset{RUL_{P_i} \in RUL_i}{\operatorname{argmax}} f\left(RUL_{P_i}\right) \tag{4.19}$$

where the "$\operatorname{argmax}_{x \in S} f(x)$" represent arguments x for which $f(x)$ attains its largest value.

(2) For the failure threshold series FT

Each failure threshold contained in FT corresponds to a predicted RUL value as described above, and h predicted RUL values constitute a final predicted RUL series $\widehat{RUL} = \left(\widetilde{RUL}_1, \widetilde{RUL}_2, \dots, \widetilde{RUL}_h\right) \in \mathbb{R}^h$.

4.4. Vehicle-oriented long-term accelerated stress test experiments

To validate properly the proposed hybrid prognostics method, long-term dynamic ageing experimental data ([122]) from a vehicle-oriented commercial PEMFC single cell is used. Specifically, a test station with integrated control and observation is used to deploy the ageing experiment, and to activate the PEMFC before performing the test. The relative humidity of the cathode and anode is regulated by the built-in humidifier of the test station. A peripheral water-cooling system is used to handle the operating temperature of PEMFC. The main technical parameters of the PEMFC are listed in Table 4.2, where the cathode/anode inlet pressures and relative humidity, as well as the operating temperature, are set to the desired optimal values.

Items	Values			
Active surface (cm^2)	25			
Hydrogen inlet-pressure (kPa)	110			
Air inlet-pressure (kPa)	110			
Operating temperature (°C)	85			
Hydrogen relative humidity (%)	50			
Air relative humidity (%)	80			
Full load current (A)	35.6			
Load currents involved in dynamic load cycles (A)	0;	1.78;	4.45;	9.51;
	10.4;	14.85;	20.75;	29.65

Table 4.2 Dynamic ageing test conditions.

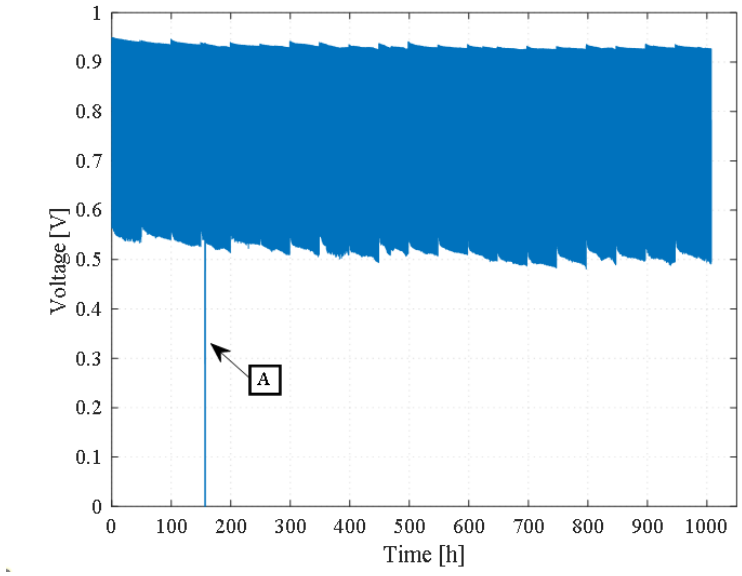

(a)

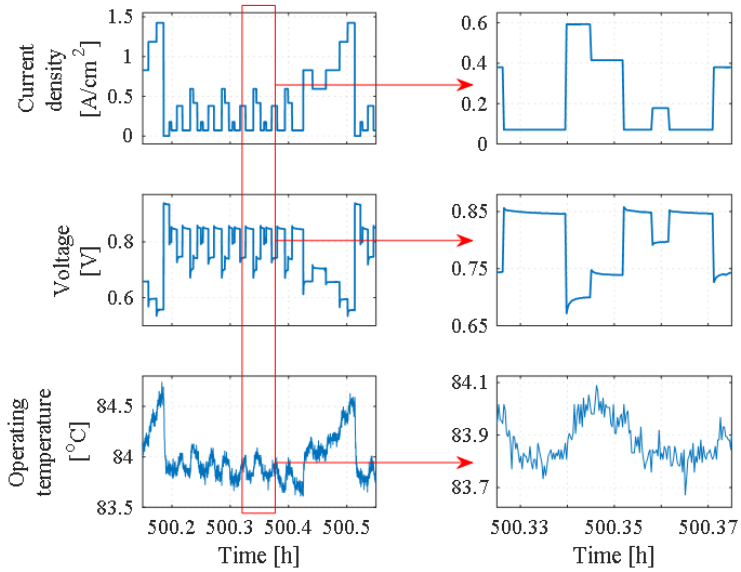

(b)

Figure 4.6 Cyclic dynamic loading for accelerated stress testing: (a) overall dynamic voltage; (b) around 500 hours, current density, voltage and operating temperature in one cycle, and zoom-in details.

This ageing experiment can be considered as an in-situ accelerated stress test [92], which is designed with reference to the New European Driving Cycle (NEDC) [122]. As shown in Figure 4.6, each cycle lasts for 1,181 s, including the urban condition (performed 4 times) and the suburban condition (performed one time). Nine different load currents (0-100%) are involved as shown in Table 4.2. The entire ageing experiment consists of 3,076 cycles, accounting for approximately 1,008 hours. A polarization curve test is performed before the start of the overall ageing experiment. Subsequently, the AST is suspended every 50 hours and resumed until the end of the polarization curve test (non-shutdown). In addition, every 100 hours, a planned

shutdown of 12 hours is executed to simulate the shutdown-condition of the actual vehicle. It is worth mentioning that typically the shutdown comes with a performance recovery of the PEMFC. This is realistic, but it inevitably causes fluctuations in HI, making the prognostics challenging.

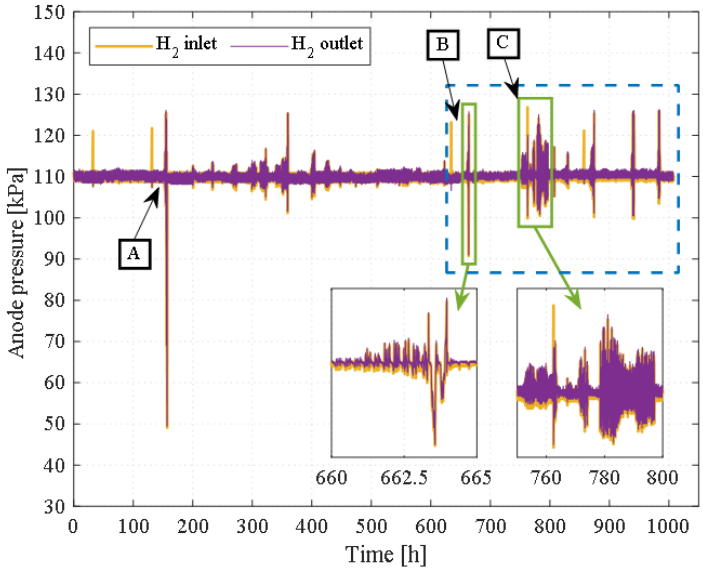

(a)

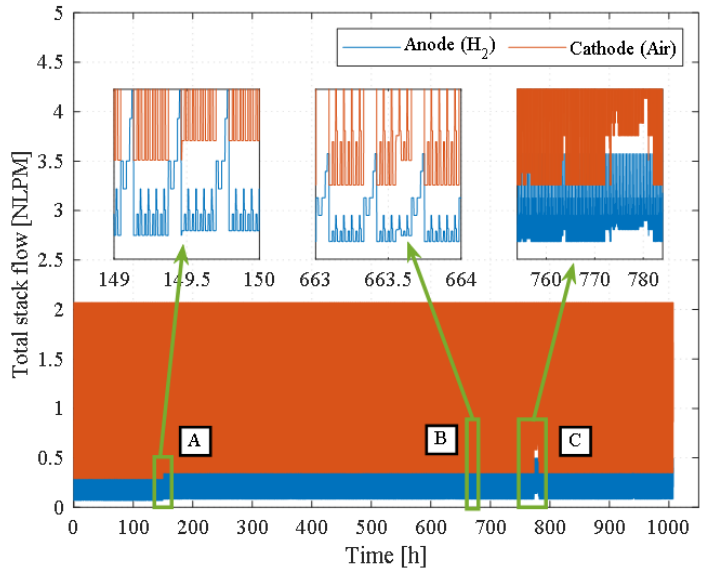

(b)

Figure 4.7 Anode gas pressure conditions and total stack flow, (a) the relationship between anode gas pressure and abnormal operation; (b) the relationship between total stack flow and abnormal operation.

During the ageing experiments, the test station and peripheral equipment encounter some anomalies, which are referred to as abnormal operations in this Chapter. As in Figure 4.7 (a), the inlet/outlet pressure of hydrogen is set at the optimal value of 110 kPa. However, significant fluctuations arise in practice. Coincidentally, as in Figure 4.7

(b), the total stack flow of H_2/Air also exhibit the related abnormal operations. Among them,

(1) Point A is a sharp oscillation of the inlet pressure that occurred at around 150 hours, corresponding to the shutdown-like voltage dip in Figure 4.6 (a).

(2) Point B is the frequent and more violent hydrogen supply anomalies starting at around 660 hours, as in the blue dashed box in Figure 4.7 (a).

(3) Point C, some gas pressure/flow anomalies lasting more than 10 hours are observed during 750-800 hours.

More details of the experimental data can be found in [100, 122].

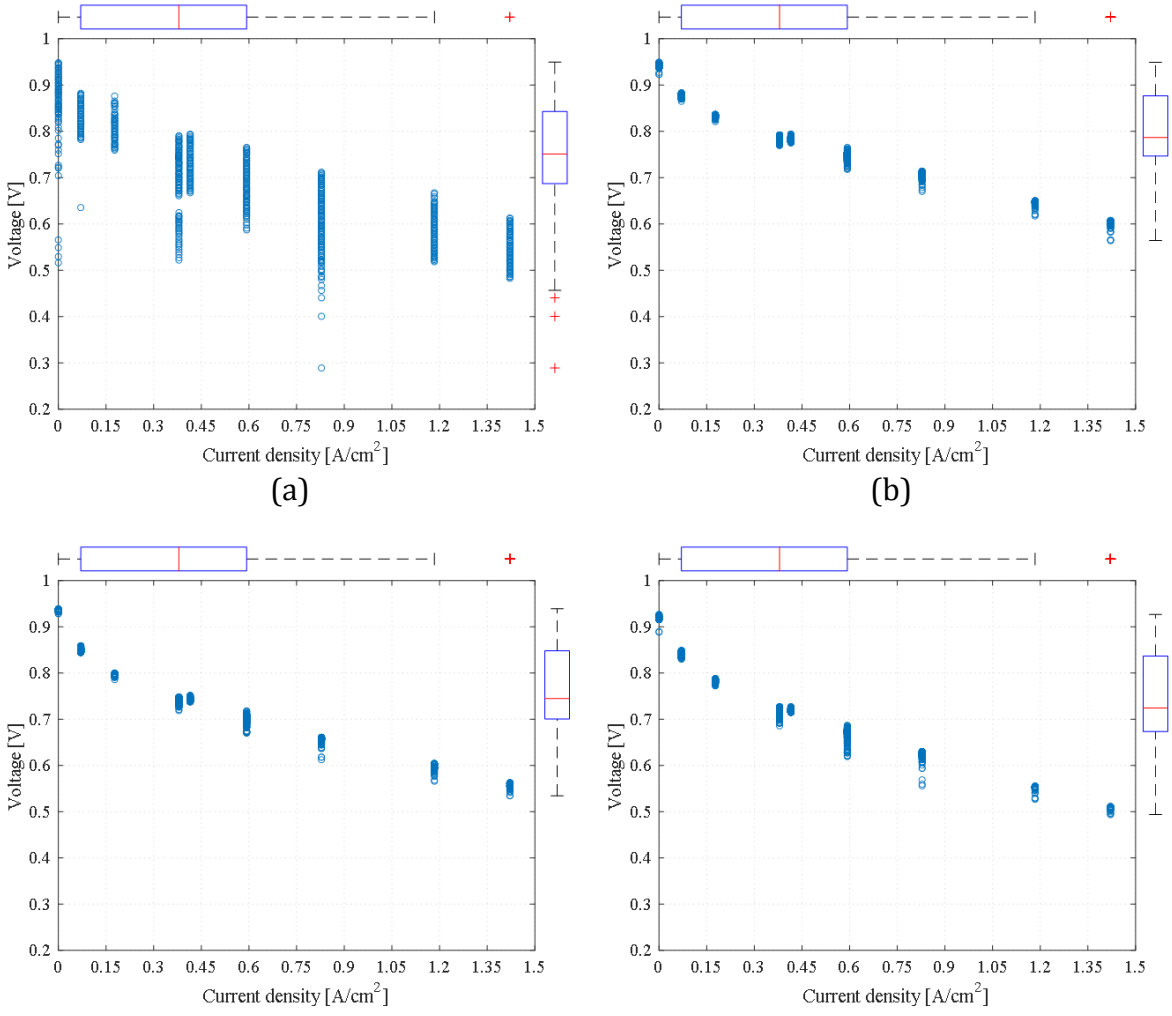

Figure 4.8 Current density-voltage scatterplot in, (a) overall (0-1008 hours); (b) 0-1 hours; (c) 500-501 hours; (d) 1007-1008 hours.

Figure 4.8 (a) is the overall (0-1008 hours) current density-voltage scatterplot, which contains the long-term degradation and anomalous operations. The following phenomena are contained in Figure 4.8 (b)-(d),

(1) ageing experiments with 9 different loads including full load, which covers most of the operating conditions.

(2) the decrease in voltage with time, which reflects the degradation in performance;
(3) unlike the typical polarization curve, the data points are more dispersive due to the inclusion of short-term (transient) dynamics.
(4) The cell dynamic load operates mainly in the ohmic losses region. In these cases, the degradation model proposed in this Chapter can be used to handle the dynamics.

Frankly, for most fuel cells, whether in the form of a single cell or a stack and regardless of the output power levels, it is recommended typically to operate in the ohmic losses region, which represents high efficiency. Recall that this Chapter is based on single-cell modelling that can be extended to a stack. Therefore, the use of the above experimental data to verify the prognostics strategy does not limit its generality.

4.5. Prognostics results evaluation and discussion

4.5.1. Evaluation criteria

In this Chapter, two metrics are used to evaluate the hybrid prognostics method, RE and Prognostics Horizon (PH). Among them, RE can be defined by Equation (3.19). In this case, x in Equation (3.19) can be the actual single-cell voltage (E_{cell}) or the actual remaining useful life (RUL_{a_i}); $\hat{x}$ corresponds to the identified/reconstructed single-cell voltage ($\hat{E}_{cell}$) or the predicted remaining useful life ($\widetilde{RUL}_i$).

Subsequently, the predicted RUL is further evaluated using PH, the definition of which differs from those proposed in [30, 123]. In this Chapter, PH is defined using a Trust Area (TA), which is the area between the upper/lower trustworthiness boundaries parallel to the actual RUL. In the CFR, the i-th ($i = 1,2,\ldots,h$) failure threshold FT_i corresponds to the TA_i as follows

$$RUL_{a_i} - t_{a_i} \cdot \alpha_{low} \leq TA_i \leq RUL_{a_i} + t_{a_i} \cdot \alpha_{up} \tag{4.20}$$

where α_{low} and α_{up} are used to adjust the tolerance of TA_i, the smaller they are the tighter the trust area (and the smaller the range of TA_i). In this Chapter, α_{low} and α_{up} are set to 15% and 5%, respectively. The PH_i as follows

$$PH_i = t_{a_i} - t_{1st_i} \tag{4.21}$$

where t_{1st_i} denotes the earliest time point after which the predicted RULs are all within the TA_i. The larger PH is, the more sufficient time is guaranteed for control/maintenance and the more effective the prognostics.

4.5.2. Evaluation of extracted health indicator

Based on the analysis for the current density-voltage scatterplot in Section 4.4, equal interval division is chosen for the HI extraction. The width of each time slot is set to the

duration of three dynamic cycles (about one hour). In Table 4.3, the identified parameters are listed, along with the type of voltage losses to which they belong.

Parameter	Value/Range	Overpotential losses
α_{a+c}	0.74	Activation
j_{loss} (mA/cm^2)	10	Activation
j_{exch} (mA/cm^2)	9	Activation
β_{a+c}	0.13	Concentration
j_{max} (A/cm^2)	3.539	Concentration
C_{dl} (mF/cm^2)	64 to 464	Activation & Concentration
R_{dyn} (Ωcm^2)	-0.007 to 0.053	Activation & Concentration
R_r (Ωcm^2)	0.03 to 0.08	Ohmic
R_{equ} (Ωcm^2)	0.0344 to 0.1002	Ohmic (nominal)
E_{rev} (V)	0.923 to 0.967	-

Table 4.3 Parameter identification results.

In Figure 4.9, the identified variable parameters are shown. By introducing all identified parameters into Equations (4.1)-(4.3) and setting the operating current at 35.6 A, the equivalent full-load power (P_{equ}) is calculated and illustrated in Figure 4.9 (f). In overall, almost all the variable parameters show a significant jump at point A, this is caused by a severe fault in the hydrogen supply. Meanwhile, there is a clear change of the trend after point B, which can be considered as an effect of the abnormal gas pressure/flow operation mentioned in Section 4.4 (Figure 4.7 (a) and (b)). There are some obvious outlier points in C_{dl} and the trend characteristics are not obvious. In addition, all other variable parameters show different levels of trend characteristics until point B. To be specific, $E_{rev}$and P_{equ} appear to possess generally decreasing trends, but P_{equ} looks smoother. R_r, R_{dyn} and R_{equ} imply generally increasing trends, with R_{equ} showing a more clearly monotonous trend. Moreover, considering that both R_{equ} and P_{equ} are the parameters that characterize the overall situation with physical interpretation, they are designated as HI_1 and HI_2, respectively. It is worth mentioning that the trend features inherent in the identified parameters are consistent with the experimental data or have physical interpretability. Moreover, some parameters are not selected as HIs, but they can still be potential candidates. For instance, the trend feature of C_{dl} is not obvious, but its outliers indicate some abnormal operation of the fuel cell.

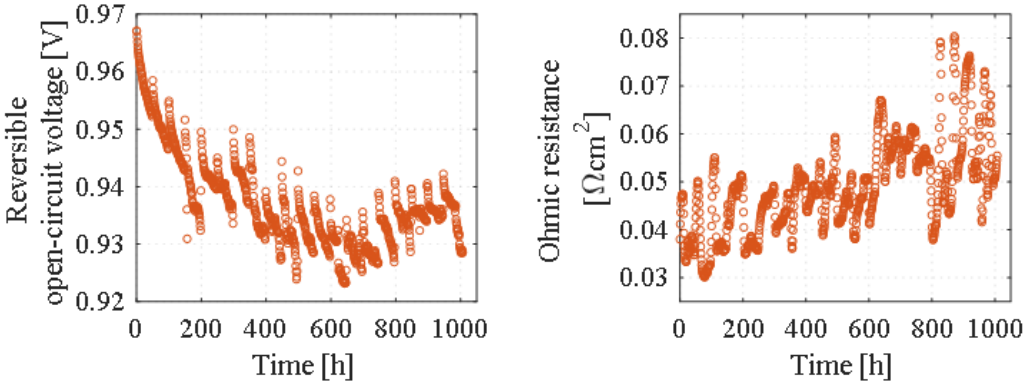

(a) (b)

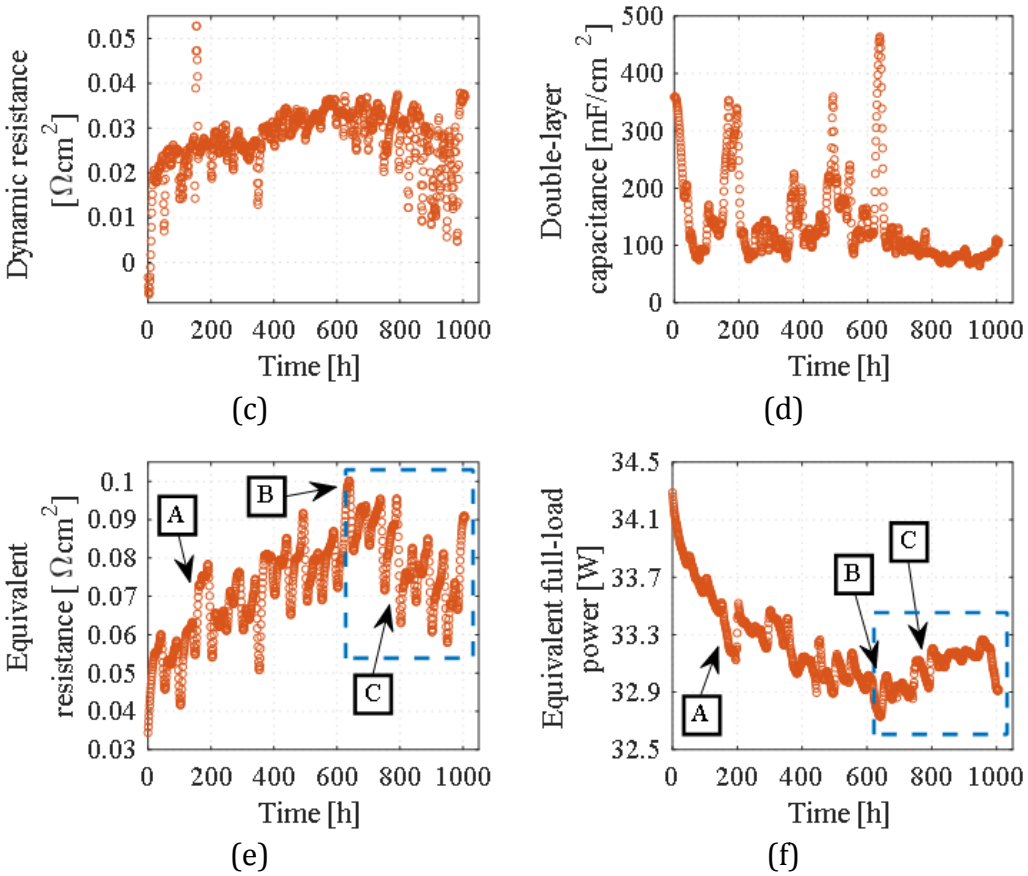

Figure 4.9 Parameters identification: (a) reversible open-circuit voltage (E_{rev}); (b) Ohmic resistor (R_r); (c) dynamic resistor (R_{dyn}); (d) double-layer capacitor (C_{dl}). (e) equivalent resistance (R_{equ}); (f) equivalent full-load power (P_{equ}).

The final output of the degradation mechanism model is the single cell voltage. Thus, the cell voltage values calculated by the identified model are compared with the actual measurements to evaluate the model identification performance. As an example, Figure 4.10 (a) and (b) show the comparison corresponding to a dynamic cycle around 500 hours. Figure 4.10 (a) shows that the operating voltages and the reconstructed voltages which can match well to each other. Figure 4.10 (b) shows the current density-voltage plot in which the overall match is satisfactory. It is worth noting that, after load switching, as in Figure 4.6 (b), the voltage exhibits an overshoot-like dynamic. Especially at the instants of switching, such dynamics correspond to the points in Figure 4.10 (b) where the experimental data are out of the identification curve. At these points, the reconstructed voltage fitting performance is slightly worse. That is because, as mentioned in Section 4.2, simplifications are considered when modelling the degradation mechanism. Furthermore, to quantitatively evaluate the model performance, the relative error (RE_E) in terms of single-cell voltage is calculated using Equation (3.19) and illustrated in Figure 4.10 (c). Observations for the ageing test are sampled at 1 Hz, so the RE_E is calculated over more than 3.6 million data points. The average RE_E is less than 1%, which demonstrates the effectiveness of the proposed model and model identification method.

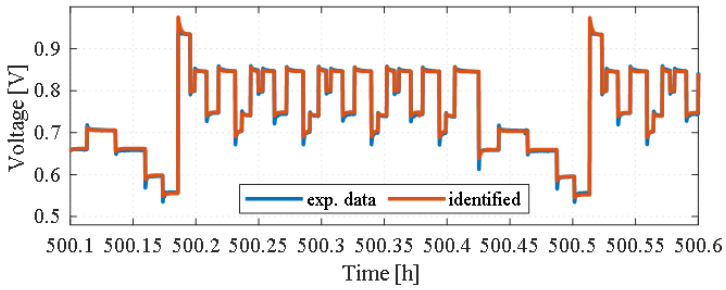

(a)

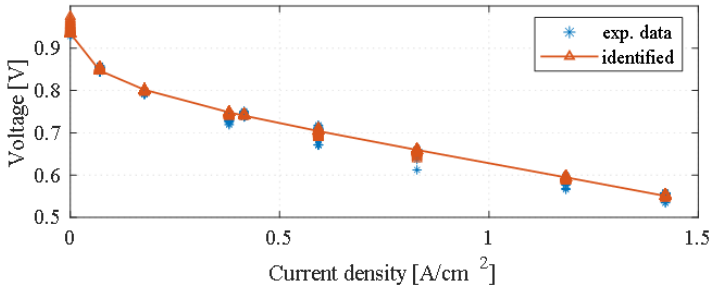

(b)

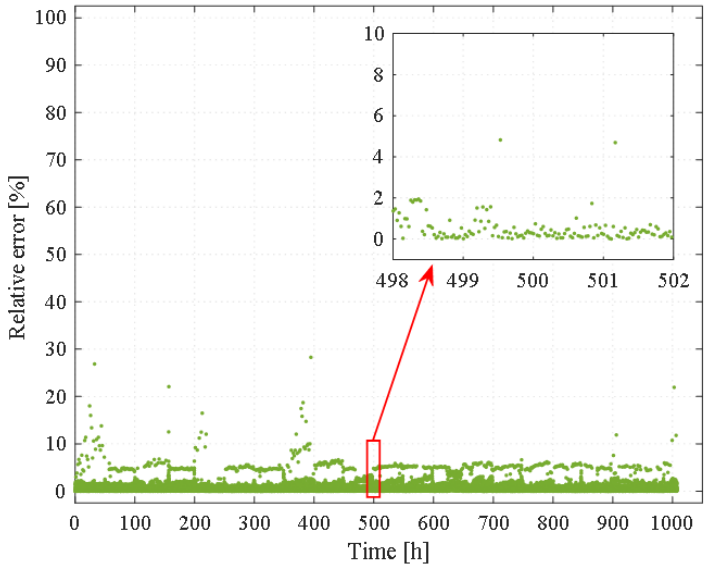

(c)

Figure 4.10 Evaluation of dynamic load identification performance: (a) identification of the cell voltage; (b) current density-voltage plot of identification results; (c) relative error of identification results.

4.5.3. Evaluation of predicted remaining useful life

In evaluating the performance of the proposed RUL prediction method, the prediction starting points and failure range are set based on the analysis of HI_1 and HI_2, as in Figure 4.11. In particular, a change in operational behaviour after point B is considered. As a consequent change in the degradation trend is observed after B, the HI after the maximum/minimum point near B (approximately hour 640) is set as invalid. For the useful HI, RUL predictions are deployed at 50-hour intervals from about 50 hours to

about 500 hours. Meanwhile, a CFR consisting of a series of failure thresholds is set in place of a single failure threshold. For HI_1, the CFR is 0.0961-0.1001 Ωcm² ; while the CFR for HI_2 is set to 32.74-32.82 W.

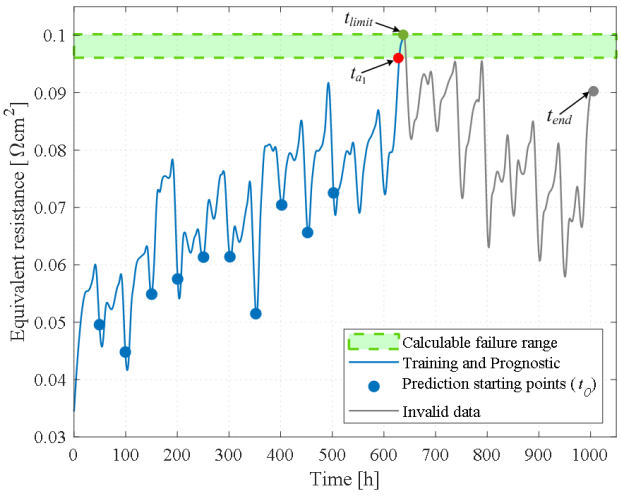

(a)

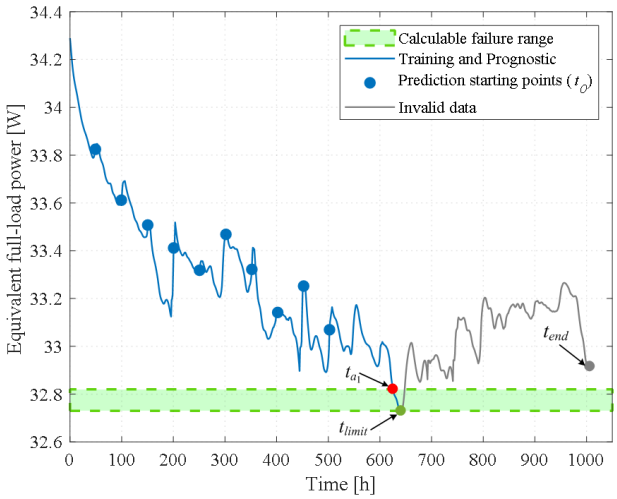

(b)

Figure 4.11 Health indicator and failure range for prognostics: (a) equivalent resistance (HI_1); (b) equivalent full-load power (HI_2).

For HI_1, the performance of the proposed method in terms of RUL prediction is evaluated as shown in Figure 4.12. In the first two test points, the predicted RUL does not enter the TA. This is mainly because the training data in the early stage are not sufficient to capture the global evolution trend. With increased training data, the prediction error gradually decreases and predicted RUL enters the TA. The calculated PH exceeds 350 hours on different FTs. If the full useful lifetime is set to 640 hours, this means that the PH exceeds 50% of it. In addition, to evaluate more appropriately the prognostics performance, comparison experiments are deployed using the autoregressive integrated moving average model. As in Figure 4.12 (a), some prediction results of the ARIMA model exhibit greater errors compared to the ABBA-LSTM. In terms of consistency, the two models perform similarly. On the other hand, in Figure

4.12 (b), the prediction performance is quantitatively evaluated using Equation (3.19). Overall, the prediction errors maintain high stability when FT varies. Moreover, the average relative error in the CFR is 15.5%.

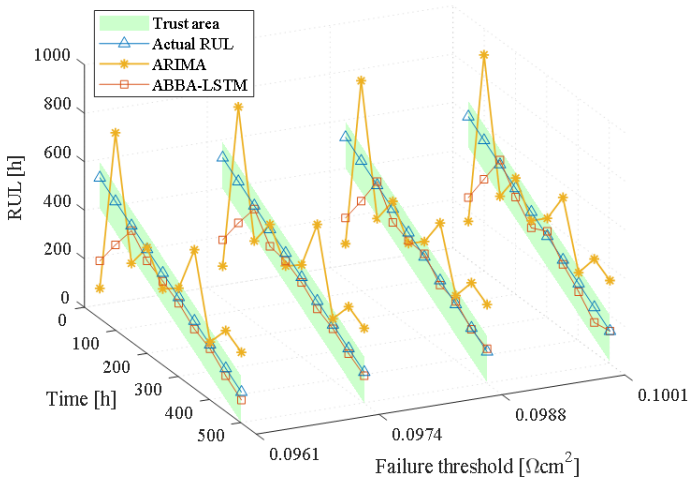

(a)

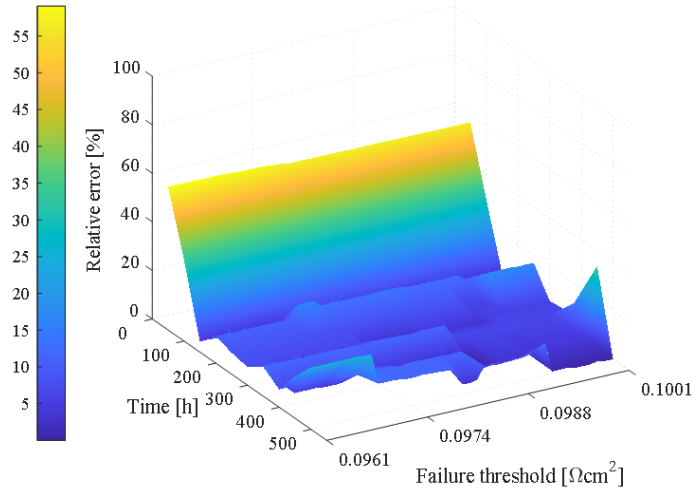

(b)

Figure 4.12 For HI_1, RUL prediction performance and evaluation at different failure thresholds: (a) comparison experiments and prognostics horizon evaluation; (b) relative error of the CFR (0.0961-0.1001 Ωcm²).

The same performance evaluation is deployed on HI_2, as in Figure 4.13. Thanks to HI_2 being smoother, the prediction performance is better than HI_1 overall. For different FTs, PHs are greater than 400 hours which accounts for more than 60% of the full useful lifetime. In the best case, PH exceeds 450 hours, which means that satisfactory prognostics results can be given with only 50 hours of ageing data. Additionally, in the comparison experiments, as in Figure 4.13 (a), almost all the predictions of the ARIMA model are lower than the actual RUL, and most of them perform worse than the ABBA-LSTM. On the other hand, the performance of the relative error is stable within the CFR. Then the average relative error in the CFR is 11.4%.

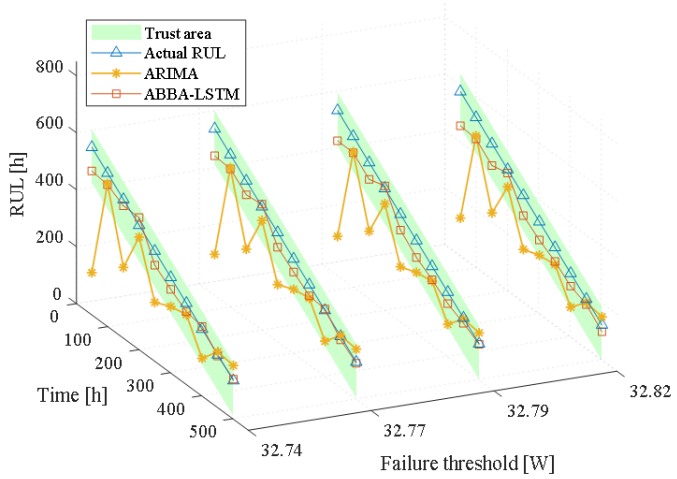

(a)

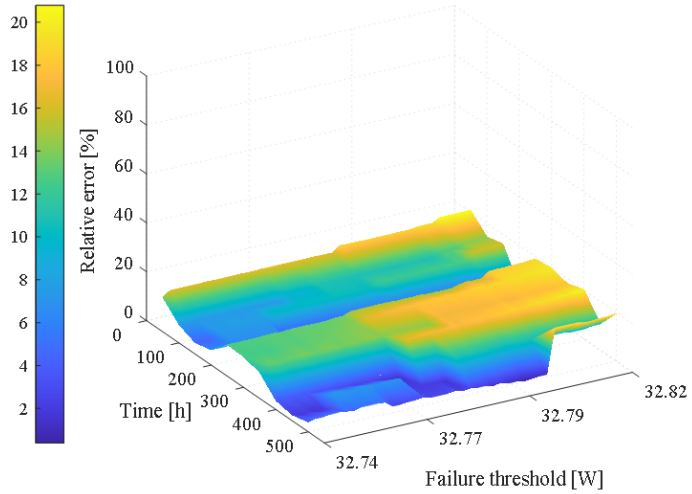

(b)

Figure 4.13 For HI_2, RUL prediction performance and evaluation at different failure thresholds: (a) comparison experiments and prognostics horizon evaluation; (b) relative error of the CFR (32.74-32.82 W).

4.6. Discussion

In this Chapter, a hybrid prognostics strategy is proposed for predicting the remaining useful life of fuel cells. A degradation mechanism model is used to handle the dynamic operating conditions of FC and extract the health indicators that can be used for prognostics. In addition, the proposed method is validated using the accelerated stress test/dynamic load cycle ageing test data of a vehicle-oriented PEMFC. The results show that the proposed degradation mechanism model can effectively track both the dynamics caused by load transitions and the ageing-related parameter variation. The average relative error of the model output is less than 1%. Furthermore, two different health indicators, i.e., equivalent resistance (HI_1) and full power (HI_2), are extracted and the ABBA-LSTM RUL prediction model is evaluated in the set failure region of the two health indicators respectively. The RUL predictions based on HI_1 and HI_2 are not

entirely consistent, especially at the earliest two “prediction start points”. This result can be attributed to the following factors.

(1) Generally, RUL prediction precision is related to the size of the historical dataset. The prediction results based on HI_1 and HI_2 are limited by the training set size at the initial “prediction start points”, thus the performances are not satisfactory.

(2) Overall, the fluctuation of HI_1 is larger than that of HI_2. After superimposing the limitation of the training data size, the prediction performance based on HI_1 is worse in the earliest two prediction points.

(3) As more data are available for training the model, the predictions gradually converge to the actual RUL. For both HIs, since the third “prediction start point”, the predictions almost all fall in the trust area.

(4) The ARIMA model used for performance comparison also exhibits the above characteristics, although its performance is inferior to that of the ABBA-LSTM in general.

In summary, the results show that the prognostics horizon that exceeds 60% of the useful full lifetime can be achieved, and the relative error of RUL prediction can reach 11.4%. The proposed hybrid strategy has the ability to handle long-term prognostics that are full of dynamics in automobile applications. However, there are non-negligible computational costs to deploy such a prognostics strategy. It is essential to reduce the computational cost while further optimizing the prognostics accuracy for potential online deployments.

5. Hybrid prognostics approach based on HHT and symbolic-GRU

5.1. Introduction

PHM assesses and predicts the evolving behavior of engineering equipment, systems and structures to enable the prediction of failures and the avoidance of accidents, and ultimately to achieve reliable, efficient, economical and safe operations [25, 26]. Machine learning and deep learning are already successful in the fields of control and computer vision [124]. In reliability engineering and safety analysis, data-centric PHM methods will undoubtedly be booming as well [125]. For PEMFCs, the PHM is also a promising solution for durability enhancement. As one of the keys to PHM, "Prognostics" tracks the health status of PEMFCs. In turn, the RUL can be predicted to support Condition-based Maintenance (CBM) [11]. However, dynamic mission profiles make it difficult to access the HI directly. As mentioned in the previous Chapters, scholars have proposed several fruitful prognostics methods for variable load conditions. However, these methods have shortcomings such as high computational cost, requiring extra characterization tests, and hardly tracking transient dynamics.

On the other hand, the degradation behaviour of PEMFC is coupled with dynamic operations, which makes it difficult to predict both the inherent degradation trend and the RUL. Some scholars prefer to deploy short-term prognostics (single-step-ahead prediction) under dynamic mission profiles [95, 100, 101]. In practice, highly accurate single-step-ahead prediction is more meaningful for the real-time control and monitoring of fuel cells. In contrast, the prognostics dedicated RUL prediction needs to extend the prognostics horizon to the order of hundreds to thousands of hours. Thus long-term prognostics provide ample time to develop maintenance schedules to avoid fatal failures. Most long-term prognostics methods for dynamic mission profiles are based on the multi-step-ahead prediction and set a fixed FT for method evaluation. The proposed prognostics methods often need cautious model configurations and the RUL performance in these proposed works is not fully justified due to limited data and evaluation criteria.

In summary, although studies involving PEMFC durability are highly noted, long-term prognostics under dynamic loading profiles has not yet been fully addressed. The main challenges arise from the following two-fold questions:

(1) How to extract the health indicator from dynamic mission profiles efficiently without disturbing PEMFC operation.

(2) How to extend the scale of prognostics horizon and to achieve stable prognostics performance under different failure thresholds.

To cope with the above issues, a data-driven prognostics method based on time-frequency analysis and symbolic recurrent neural networks is proposed in this Chapter. Specifically, the long-term degradation component of the dynamic stack voltage is first extracted as HI using the Hilbert-Huang transform. The HI is compressed using adaptive Brownian bridge-based aggregation and represented as a reduced-dimensional symbolic sequence [121]. The trend of the represented symbolic sequence is predicted by gated recurrent unit-based RNN, which in turn is used to reconstruct the HI trend and estimate the RUL. The proposed method is evaluated using dynamic load ageing experimental data from two different types of PEMFCs. In comparison with other state-of-the-art methods, the proposed method takes the shortest computational time while extracting reliable HI. In the RUL prediction phase, the proposed method provides effective PH up to hundreds of hours scale and shows consistency at different FTs.

5.2. Hilbert-Huang transform-based health indicator extraction

As the PEMFC operates under dynamic load profiles, the real-time measurements, such as fuel cell voltage, exhibit non-linear and non-stationary characteristics. The HHT, proposed by Huang et al., is adaptive and highly efficient [126]. In this Chapter, HHT is considered an appropriate tool to deal with non-linear and non-stationary signals and therefore used to extract the health indicator [127]. In fact, HHT is already being applied in the prognostics of complex systems/devices, e.g., lithium-ion batteries [128-130], rolling element bearings [131], and nuclear power plants [132]. In the field of fuel cells, HHT is also used for diagnostics [133] and prognostics [134]. The HHT consists of two steps: First, the input signal is decomposed into a series of Intrinsic Mode Function (IMF) and a residual using Empirical Mode Decomposition (EMD). Second, the Hilbert spectrum of each IMF is obtained by deploying the Hilbert Transform (HT). The combination of EMD and Hilbert Spectral Analysis (HSA) provides a time-frequency-energy analysis method [127].

Generally, EMD sifting is iteratively implemented and stopped under the condition that a monotonic residual is obtained. The residual reflects the trend characteristics in the original signal [134]. The residual contributes to revealing the physical characteristics of the signal as it is the low frequency or null component. In this Chapter, the dynamic voltage of the PEMFC is used as the input signal of EMD sifting. The proper residual from the input signal is identified by iteratively implementing EMD and designated as HI. Considering the Instantaneous Frequency (IF) is one of the key features for analyzing the signal based on natural conditions [127]. In this Chapter, an HI extraction process based on IF analysis is proposed as shown in Figure 5.1. Instead of pursuing a completely monotonic residual as the stop condition of the EMD sifting process, the method analyzes whether the IF of the residual is below a set threshold.

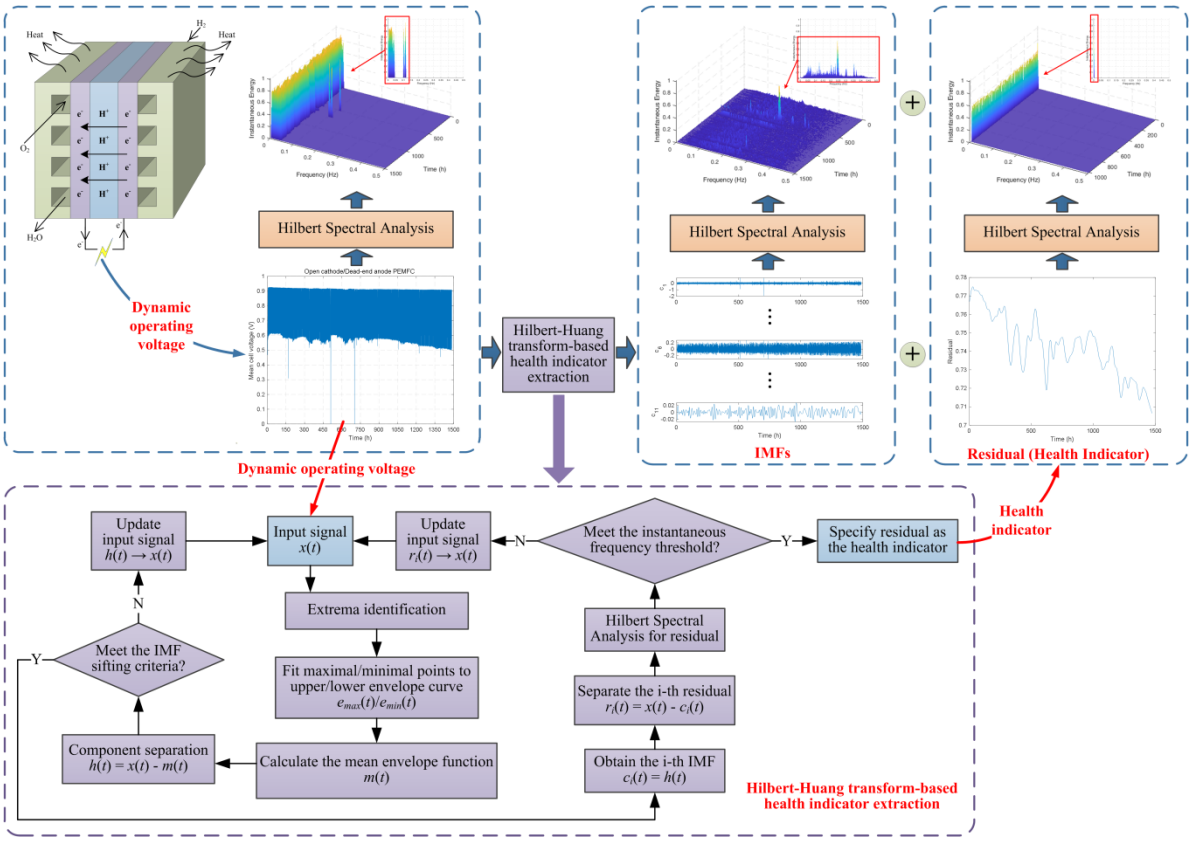

Figure 5.1 Hilbert-Huang transform-based health indicator extraction process.

As shown in Figure 5.1, the specific sifting process is explained as follows.

(1) Identify all extrema of the input signal $x(t)$. The upper envelope curve $e_{max}(t)$ and the lower envelope curve $e_{min}(t)$ are formed by fitting the maximal and minimal points through cubic spline curves, respectively. The mean envelope function $m_{1,1}(t)$ is calculated as below

$$m_{1,1}(t) = \left(e_{max}(t) + e_{min}(t)\right)/2 \tag{5.1}$$

(2) Subtract $m_{1,1}(t)$ from $x(t)$ to obtain the first component $h_{1,1}(t)$,

$$h_{1,1}(t) = x(t) - m_{1,1}(t) \tag{5.2}$$

IMF should satisfy the following criteria [126]:

- The number of poles and zeros should not differ by more than one;
- The mean of the upper and lower envelope curves should be zero.

$h_{1,1}(t)$ is defined as the first IMF $c_1(t)$ if it satisfies the criteria. Otherwise, repeat steps (1)-(2) until the requirements are satisfied at the j-th repetition,

$$h_{1,j}(t) = h_{1,j-1}(t) - m_{1,j}(t) \tag{5.3}$$

Then $h_{1,j}(t)$ is specified as $c_1(t)$.

(3) Subtract $c_1(t)$ from $x(t)$ to obtain the first residual $r_1(t)$,

$$r_1(t) = x(t) - c_1(t) \tag{5.4}$$

(4) The Hilbert transform is deployed only for the residual to obtain its IF, and the decomposition is stopped when the IF is less than a pre-set frequency threshold. Otherwise, the residual is used as the input signal and the above steps are repeated until the IF is satisfied at the n-th repetition. Then the final residual is $r_n(t)$ and is specified as HI,

$$r_n(t) = r_{n-1}(t) - c_n(t) \tag{5.5}$$

Up to this point, $x(t)$ can be expressed by the following equation,

$$x(t) = r_n(t) + \sum_{i=1}^{n} c_n(t) \tag{5.6}$$

In addition, the residual signal implies the long-term degradation trend characteristics of the PEMFC stack voltage. The IF threshold is set based on the time scale of PEMFC degradation and the time-frequency-energy characteristics of the stack voltage signal. The details about Hilbert transform as follows.

For the i-th residual $r_i(t)$, where $i = 1, \dots, n$. The Hilbert transform of the residual (e.g., $\mathcal{H}_i(t)$) can be calculated as follow,

$$\mathcal{H}_i(t) = \frac{1}{\pi} PV \int_{-\infty}^{\infty} \frac{r_i(\tau)}{t-\tau} d\tau \tag{5.7}$$

where PV is the Cauchy principal value. The $z_i(t)$, which is an analytical function of $r_i(t)$, can be constructed as the following equation,

$$z_i(t) = r_i(t) + j\mathcal{H}_i(t) = a_i(t)e^{j\phi_i(t)} \tag{5.8}$$

where j is the imaginary unit. The amplitude function $a_i(t)$ and the instantaneous phase function $\phi_i(t)$ can be expanded as following equation,

$$\begin{cases} a_i(t) = \sqrt{{r_i}^2(t) + {\mathcal{H}_i}^2(t)} \\ \phi_i(t) = arctan[\mathcal{H}_i(t)/r_i(t)] \end{cases} \tag{5.9}$$

The instantaneous frequency $\omega_i(t)$ is calculated by the following equation,

$$\omega_i(t) = \frac{1}{2\pi} \frac{d\phi_i(t)}{dt} \tag{5.10}$$

Then, the instantaneous energy $\varepsilon_i(t)$, corresponding to $r_i(t)$, is calculated by the following equation,

$$\begin{cases} \varepsilon_i(t) = \int_{\omega_i^-}^{\omega_i^+} H^2(\omega_i, t)\, d\omega_i \\ H(\omega_i, t) = Re\left[a_i(t)e^{j\phi_i(t)}\right] \end{cases} \tag{5.11}$$

where ω_i^+ and ω_i^- are the frequency range upper and lower bounds of $r_i(t)$. The $H(\omega_i, t)$ is the Hilbert spectrum of $r_i(t)$, and $Re[f(x)]$ denotes to extract the real component of the function $f(x)$.

5.3. Symbolic GRU-based lifetime prediction

The essential task of prognostics is to track the degradation trend of HI and predict the RUL. Thanks to the convincing time series processing capability, several LSTM framework-based RUL prediction methods are developed for different applacations [135,

136]. Compared to LSTM, GRU effectively simplifies the hidden unit structure and reduces the number of parameters [137, 138]. This facilitates the training/prediction efficiency of GRU and promises to improve the real-time prognostics performance. The GRU-based degradation prediction method is successfully applied in fields such as aero-propulsion system [139] and lithium-ion batteries [129, 130]. As mentioned in the previous Chapters, the performance of raw LSTM is not satisfactory in multi-step-ahead prediction in the application of fuel cell prognostics. Similarly, GRU suffers from this issue.

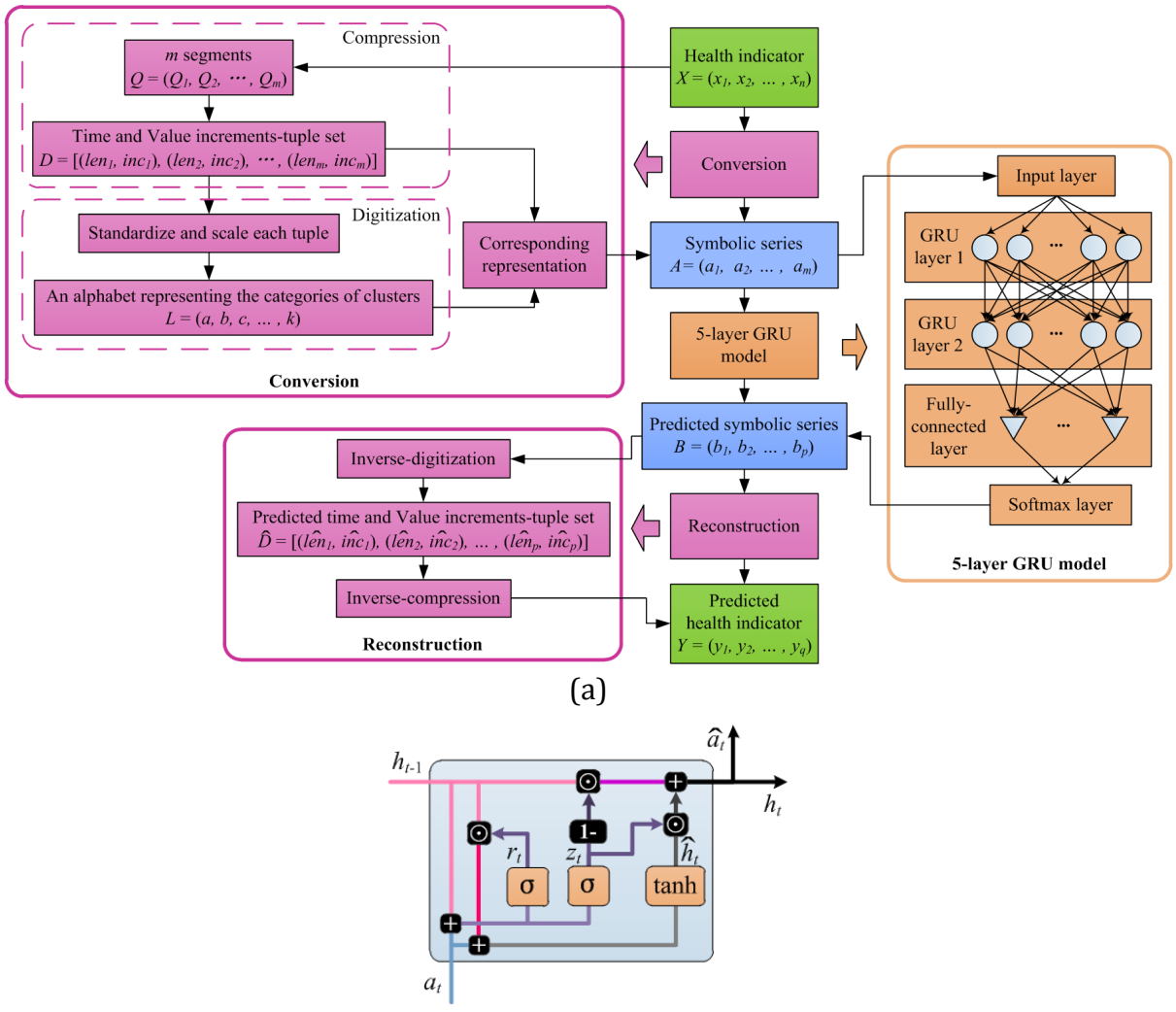

Figure 5.2 Symbolic GRU-based degradation trends prediction process, (a). ABBA-GRU structure; (b). GRU architecture.

This Chapter proposes an ABBA-based GRU (ABBA-GRU) model to tackle multi-step-ahead prediction involved in prognostics. The historical HI is used as input, while the output is the predicted trend. The core of the ABBA-GRU model includes three components: conversion, prediction, and reconstruction, as in Figure 5.2 (a) and Table 5.1. To improve prediction efficiency and accuracy, HI is normalized and re-scaled to between zero and one before being fed to ABBA-GRU.

Conversion, a. k. a. representation, is a data dimensionality reducing process that transforms a time series into a symbolic series. In the first step, the time series (X) is changed into the increments-tuple set (D) by compression; in the second step, D is converted into the symbolic series (A) by digitization. A is to be used as the input for the prediction phase.

Step		Data type	Notation
Input		Time series	$X = (x_1, x_2, \cdots, x_n) \in \mathbb{R}^n$
Representation	Compression	Time and numerical increments-tuple set	$D = \begin{bmatrix} (len_1, inc_1), (len_2, inc_2) \\ , \cdots, (len_m, inc_m) \end{bmatrix} \in \mathbb{R}^{2\times m}$
	Digitization	Alphabet set	$L = (a, b, c, \cdots, k)$, k types of clusters
		Symbolic series	$A = (a_1, a_2, \cdots, a_m) \in L^m$
Prediction		Symbolic series (predicted)	$B = (b_1, b_2, \cdots, b_p) \in L^p$
Reconstruction	Inverse digitization	Increments-tuple set (predicted)	$\widehat{D} = \begin{bmatrix} (\hat{len}_1, \hat{inc}_1), (\hat{len}_2, \hat{inc}_2) \\ , \cdots, (\hat{len}_p, \hat{inc}_p) \end{bmatrix} \in \mathbb{R}^{2\times p}$
	Inverse compression (Output)	Time series (predicted)	$Y = (y_1, y_2, \cdots, y_q) \in \mathbb{R}^q$

Table 5.1 Degradation trend prediction steps and notation defination.

A five-layer GRU model is used in the prediction phase, as in Figure 5.2 (a). Meanwhile, Figure 5.2 (b) shows the structure of a typical GRU hidden unit. The previous hidden state (h_{t-1}) together with the current symbol (a_t) constitute the input. After proper processing by the reset gate (r_t) and update gate (z_t), the current hidden state (h_t, i.e., predicted symbol) is output. In a GRU layer, the hidden units are linked sequentially to form a chain. The functional equations of the GRU are as follows.

$$\begin{cases} r_t = \sigma(W_r a_t + U_r h_{t-1} + b_r) \\ z_t = \sigma(W_z a_t + U_z h_{t-1} + b_z) \\ \tilde{h}_t = tanh[W_h a_t + U_h(r_t \circ h_{t-1}) + b_h] \\ h_t = (1 - z_t) \circ h_{t-1} + z_t \circ \tilde{h}_t \end{cases} \tag{5.12}$$

where σ and tanh represent the activation functions, which are sigmoid and hyperbolic tangent, respectively. W_x, U_x, and b_x are the input weight matrix, the unit internal weight matrix, and the bias vector, respectively. Among them, the subscript x corresponds to r (reset gate), z (update gate), and h (hidden state). The $\tilde{h}_t$ is unit internal hidden state (a. k. a., candidate activation) vector. The operator "$\circ$" denotes Hadamard product.

The reconstruction phase can be considered as the inverse process of conversion. The predicted symbolic series (B) is changed into the predicted increments-tuple set ($\widehat{D}$) by inverse digitization. Subsequently, $\widehat{D}$ is changed into the predicted time series (Y) by inverse compression. More details about ABBA can be found in Section 4.3.1.

This Chapter sets multiple failure thresholds to evaluate the consistency and credibility of the prognostics approach. At the i-th failure threshold, as in Figure 5.3, multiple (here N) ABBA-GRU models are constructed by setting different initial weight matrices. Multiple predicted degradation trends are used to calculate the corresponding RULs respectively. Afterwards, the Probability Distribution Function (PDF) of the RULs

is generated. The RUL corresponding to the maximum of the PDF is considered the final prediction.

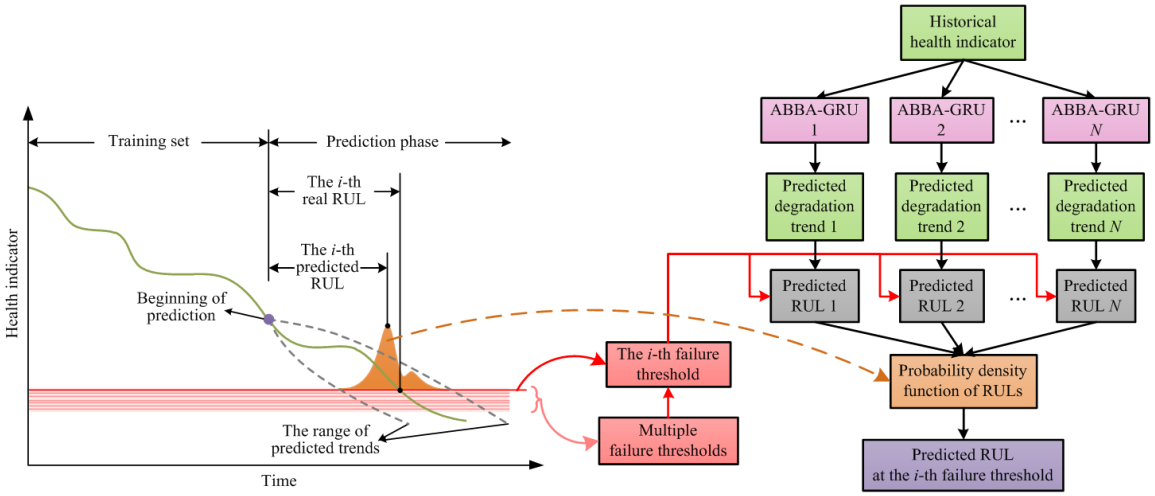

Figure 5.3 Remaining useful life prediction process and multiple failure thresholds evaluation.

5.4. PEMFC ageing experiments under dynamic load

Two long-term ageing experiments under dynamic load are implemented in this Chapter. Although they have been mentioned in the previous Chapters, it is still necessary to make some of their details specific. These durability tests are from two different types of PEMFCs, an open cathode/dead-end anode PEMFC (hereafter referred to as FC-1) and a vehicle-oriented commercial PEMFC (hereafter referred to as FC-2). The operating conditions of FC-1 and FC-2 are shown in Table 5.2.

Parameter	Value	
	FC-1	FC-2
Active surface (cm^2)	33.63	25
Pressure at hydrogen inlet (bar)	1.35	1.1
Pressure at air inlet (bar)	1.013 (i.e., 1 atm)	1.1
Nominal output power (W)	73.5	23.14
Operating temperature (°C)	29.6 to 51.7 (Corresponding to current)	85
Number of cells	15	1
Temperature regulate mode	24-V dc air fan	External circulating water pump
Humidity regulate mode	Non-humidifier (self-humidified)	Built-in humidifier

Table 5.2 Ageing experiments operating conditions.

The FC-1 is compactly designed for hybrid electric bicycles. The stack of FC-1 contains 15 cells with an integrated 24 V DC-fan for air supply and temperature regulation. The operating temperature of FC-1 is related to the load current, which can be expressed by the following equation.

$$T_{\mathrm{FC1}} = 2.5074 I_{\mathrm{FC1}} + 30.3585 \tag{5.13}$$

where T_{FC1} and I_{FC1} are the operating temperature and load current of FC-1, respectively. In addition, FC-1 is self-humidifying and performs a purge lasting 0.5 s per 30 s. The mean cell voltage profile from the dynamic load cycle of FC-1 is shown in Figure 5.4 (a), whereas the current profile is shown in Table 4.2. In each dynamic cycle, the load current of FC-1 is organized into seven test steps that repeatedly switch between 0 A and 8 A. In this way, the start-up/standby operating conditions in the hybrid system are simulated. More details about FC-1 and durability testing can be found in Section 3.3 and/or literature [85].

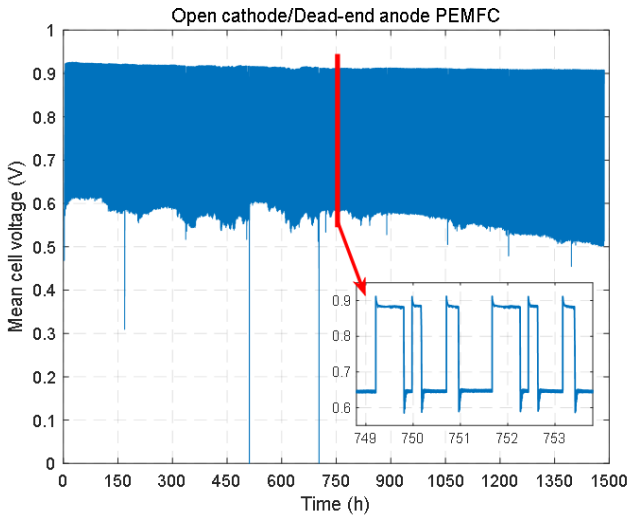

(a)

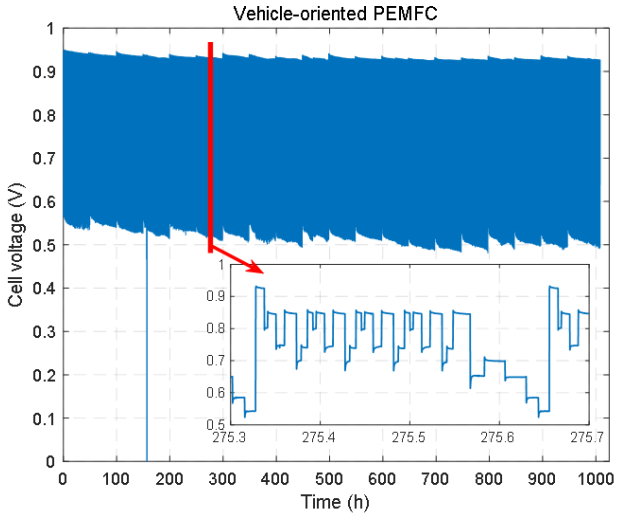

(b)

Figure 5.4 Voltage profiles of dynamic load cyclic from fuel cell ageing experiments, (a). FC-1; (b). FC-2.

The FC-2, produced by Wuhan New Energy Co., Ltd, is a PEMFC for automotive applications [122]. The stack of FC-2 contains a single cell. Ageing experiments are deployed on the Greenlight test station. The built-in humidifier is placed at the cathode and anode. The operating temperature is regulated using an external circulating water pump [100]. The cell voltage profile of the FC-2 dynamic load cycle is shown in Figure 5.4 (b), and the current profile is shown in Table 5.3. One dynamic cycle consists of two phases, each consisting of seven test steps. The first phase, called "Urban", is designed to simulate the frequent load switching of the vehicle at low speeds. The second phase, called "Suburban", is designed to simulate the vehicle switching between loads at medium/high speeds. In each dynamic cycle, "Urban" is repeated four times and then "Suburban" is executed once [100]. More details about FC-2 and ageing tests can be found in Section 4.4 and/or literature [100, 122].

Test step	FC-1		FC-2			
	Duration (s)	Current (A)	Urban condition		Suburban condition	
			Duration (s)	Current (A)	Duration (s)	Current (A)
1	108	0	13	4.45	46	1.78
2	59	8	33	1.78	58	20.75
3	76	0	35	9.51	82	14.85
4	186	8	47	1.78	85	20.75
5	96	0	20	14.85	50	29.65
6	252	8	25	10.4	44	35.6
7	108	0	22	1.78	36	0

Table 5.3 Current profiles of dynamic load cyclic

5.5. Prognostics performance evaluation

5.5.1. Evaluation metrics

Among various evaluation metrics, the prognostics horizon and the Relative Accuracy (RA) are considered both effective and widely used [3]. For the *i*-th failure threshold, a trust area (TA_i) is set which can be calculated by Equation (4.20). In this Chapter, the tolerance adjustment factors for TA_i bounds are set as $\alpha_{low} = 0.2$ and $\alpha_{up} = 0.1$. The prognostics horizon (PH_i) at this point can be calculated by Equation (4.21).

In addition, another trust area is further defined stringently, for instance, using the $\alpha-\lambda$ performance to set the trust area ($TA_i^{\alpha-\lambda}$) as follows,

$$RUL_{a_i}(1-\alpha_{low}) \le TA_i^{\alpha-\lambda} \le RUL_{a_i}(1+\alpha_{up}) \tag{5.14}$$

The trust area $TA_i^{\alpha-\lambda}$ tightens over time, requiring more demanding prognostics performance. RUL_{a_i} is actual remaining useful life.

Moreover, it is essential to calculate the relative accuracy of the predicted RUL for quantitatively evaluating the prediction performance. The calculation procedure is as follows,

$$RA_i = 1 - \frac{\left|RUL_{a_i} - R\tilde{U}L_i\right|}{RUL_{a_i}} \tag{5.15}$$

where the relative accuracy RA_i corresponding to the i-th failure threshold. $R\tilde{U}L_i$ corresponds to the predicted remaining useful life.

5.5.2. Evaluate the feasibility of the extracted HI

The programs used in this Chapter are developed in Python 3.7.11, Keras version 2.4.3, and Tensorflow version 1.15.0 backend software environments. They are deployed on a desktop computer containing an Intel Xeon E3-1230-v3 processor @ 3.3 GHz and 16 GB memory.

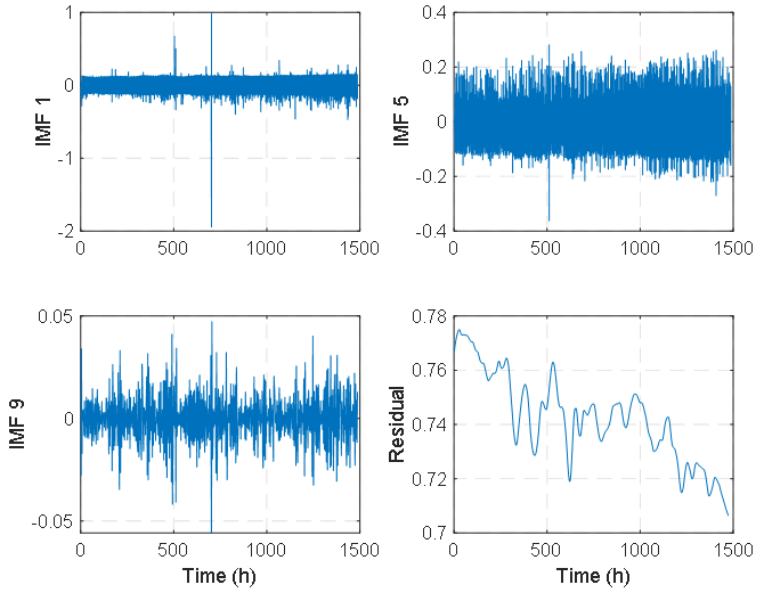

(a)

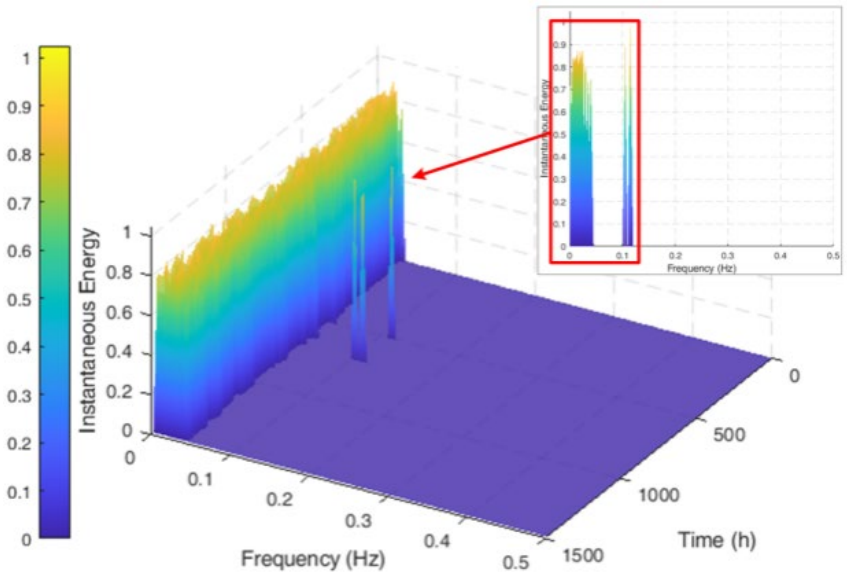

(b)

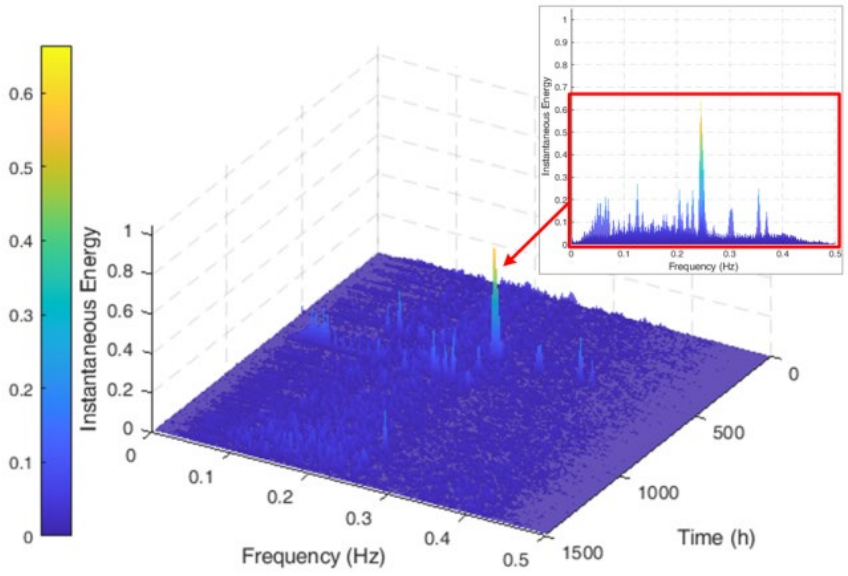

(c)

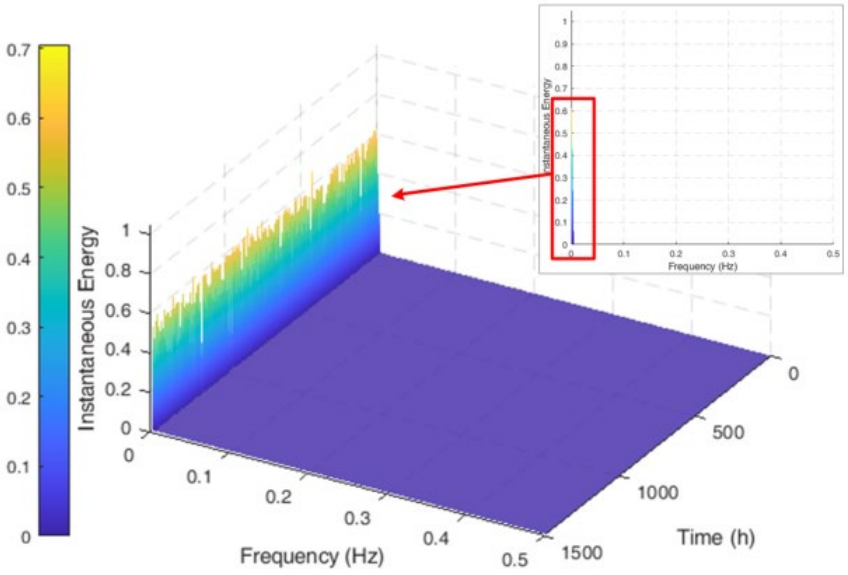

(d)

Figure 5.5 For FC-1, (a). IMFs and residual obtained by EMD; Time-frequency-energy spectrum: (b) the dynamic voltage, (c) all IMFs, (d) the residual.

The HHT-based method proposed in Section 5.2 is utilized to extract the HI, and the threshold of IF is set to 0.005 Hz. The dynamic voltage of FC-1 is decomposed into eleven IMFs and one residual, while the dynamic voltage of FC-2 is decomposed into nine IMFs and one residual. Figure 5.5 (a) and Figure 5.6 (a) show the partial (1st, 5th, 9th) IMFs and the final residual of FC-1 and FC-2, respectively. Besides, Figure 5.5 (b), (c), and (d) show the time-frequency-energy spectrum of the dynamic voltage (original signal), all IMFs, and residual of FC-1, respectively. Similarly, Figure 5.6 (b), (c), and (d) correspond to FC-2. The HHT-based HI extraction method square effectively separates the high-frequency features (IMFs) and the low-frequency feature (residual) of the dynamic voltage signal. By analyzing the instantaneous energy distribution of IMFs, it facilitates to identify fuel cell abnormal operation. For instance, in Figure 5.5 (c) and Figure 5.6 (c),

most of the instantaneous energies are at low levels. Whereas several obvious instantaneous energy anomaly peaks can be found, which correspond to the abnormal operation of FC-1 and FC-2 mentioned in Section 3.3 and/or Section 4.4. In contrast, the residual retains a relatively high level of instantaneous energy, as in Figure 5.5 (d) and Figure 5.6 (d). The instantaneous energy distribution of the residual shows a natural decreasing trend along the ageing time. This allows the residual to indicate the intrinsic degradation process of stack voltage.

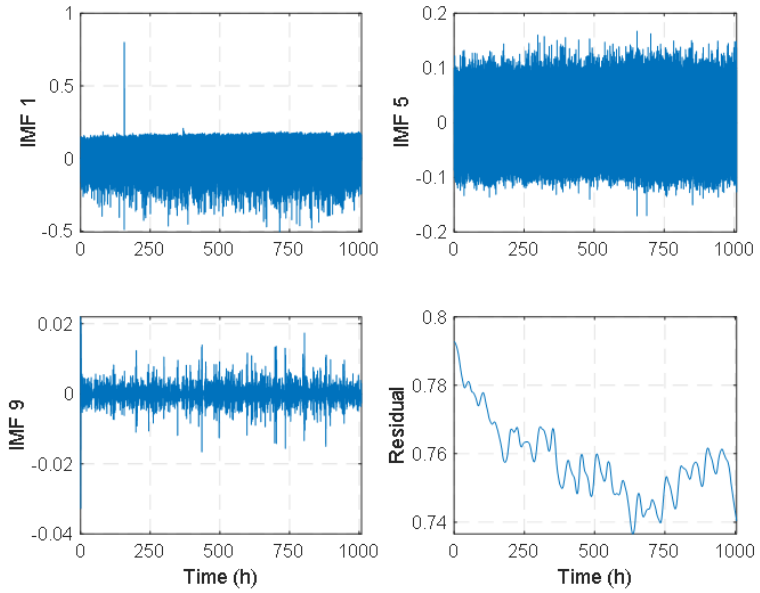

(a)

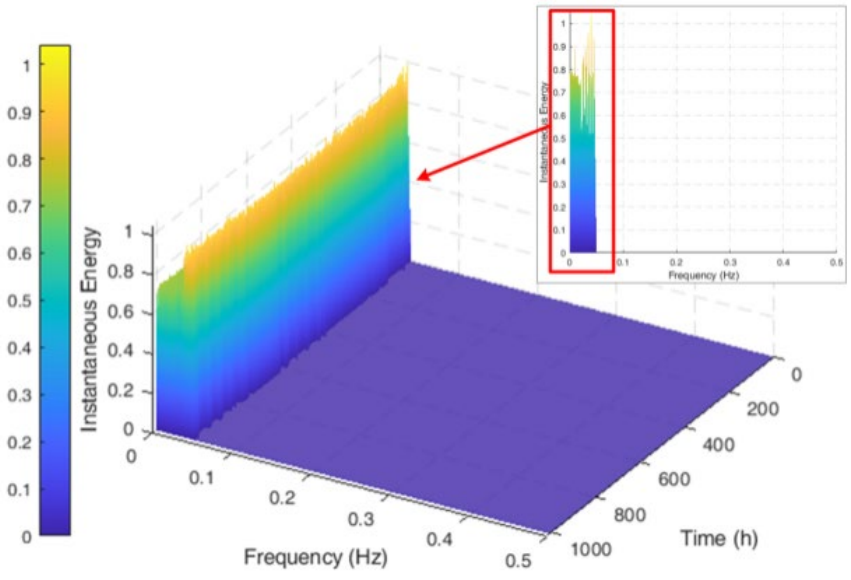

(b)

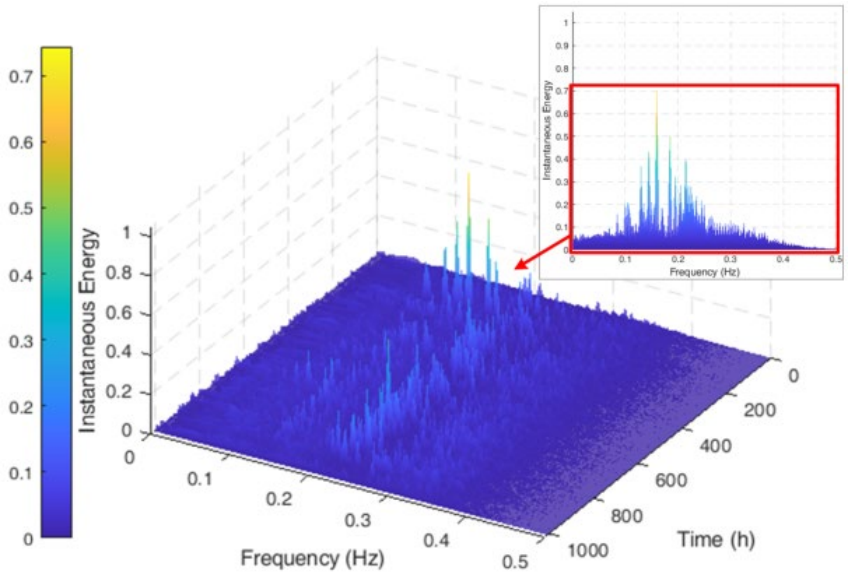

(c)

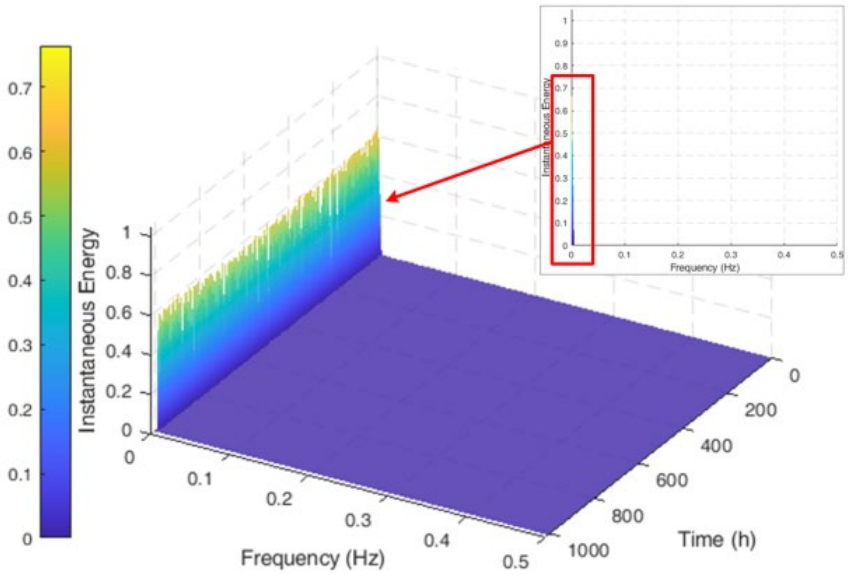

(d)

Figure 5.6 For FC-2, (a). IMFs and residual obtained by EMD; Time-frequency-energy spectrum: (b) the dynamic voltage, (c) all IMFs, (d) the residual.

In addition, the rationality of the proposed method is evaluated by comparing it with two other HI extraction methods. The first method uses the degradation model proposed in [103]. The equivalent internal resistance is obtained by piecewise linear regression and the virtual steady-state voltage is reconstructed as HI. Hereinafter, it is called the "Curve-fitting" method. The second method utilizes the linear parameter-varying model structure, as in [85], which in turn is combined with autoregressive model with exogenous input. Hereinafter, it is called "LPV-ARX" method. The virtual steady-state voltage is extracted as HI by combining time-varying properties identification and sliding-window methods. The HIs extracted by all three methods are normalized and rescaled into the range of zero to one. As in Figure 5.7, all three methods match well on both PEMFC stacks, besides a few outlier points. In particular, they all capture the

inherent voltage degradation trend. This is crucial for both analyzing the PEMFC degradation and predicting the RUL.

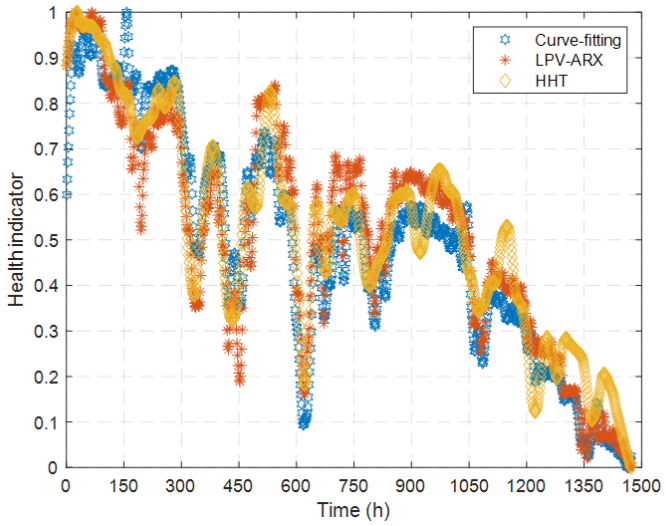

(a)

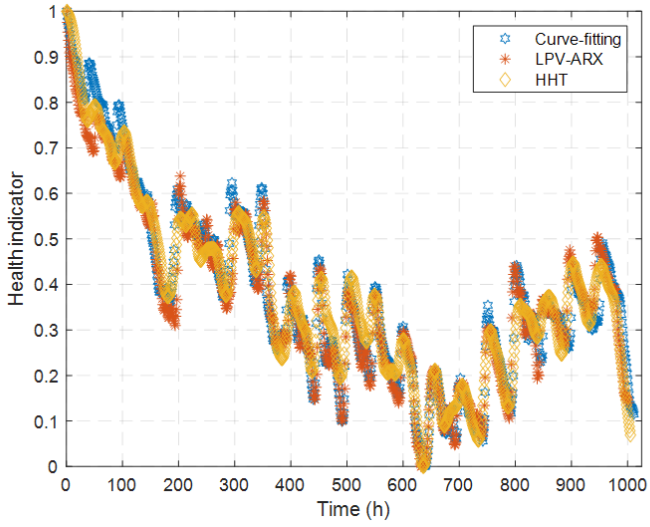

(b)

Figure 5.7 Comparison of health indicators extracted based on HHT with the other two methods, for (a) FC-1; (b) FC-2.

Method	Execution time (s)	
	FC-1	FC-2
Curve-fitting	55.61	51.85
LPV-ARX	1167.77	518.42
HHT	21.73	16.93

Table 5.4 Computational cost comparison of the three methods.

Further, the computational costs of the three methods are compared, as in Table 5.4. LPV-ARX has the highest computational cost and is significantly more than the other methods. The computational cost of HHT is slightly lower than that of Curve-fitting. It is noteworthy that the FC-1 ageing test duration is about 50% longer than the FC-2. The increase in ageing data causes the computational cost of LPV-ARX to expand significantly.

In contrast, for the other two methods, the computational cost impact of the increased ageing data is not significant.

5.5.3. Evaluate the predicted lifetime

For properly evaluating the RUL prediction performance, nine prognostics test points are set for FC-1, as in Figure 5.8 (a), with 147.5 hours between each two prognostics points. Meanwhile, twelve prognostics test points are set for FC-2, as in Figure 5.8 (b), with 49 hours between each two prognostics points. Then, ten failure thresholds from 0 to 0.09 spacing 0.01 are set. Twenty ABBA-GRU models are deployed with random initialization of the weight matrix, and for each model, the configuration is as follows: ABBA tolerance is set to 0.001; The types of clusters coefficient k is chosen adaptively between 1 and 100; Two GRU layers are included, each with 50 hidden units. The training process is optimized using Adam [116], the training learning rate is set to 0.001, the batch size is 128, and the maximum training epoch is 10,000.

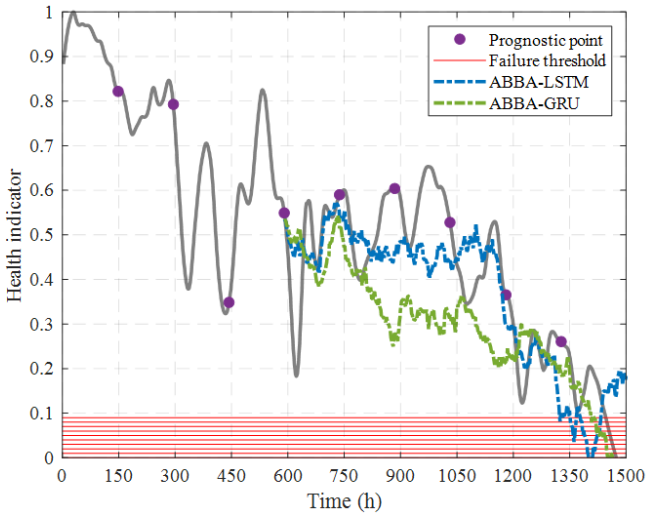

(a)

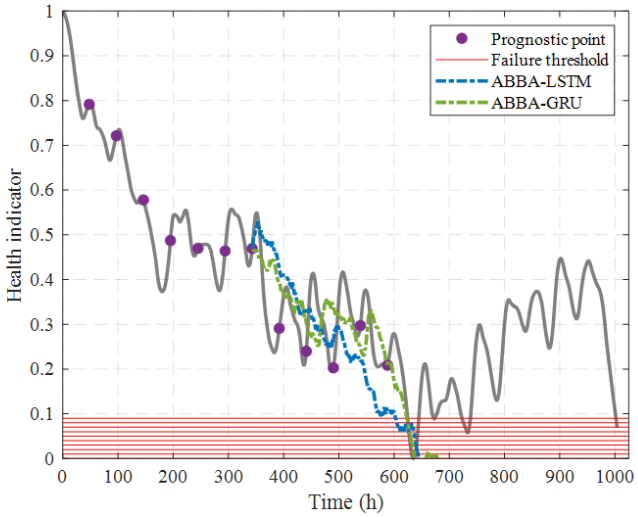

(b)

Figure 5.8 Prognostics points set on health indicators, for (a) FC-1, (b) FC-2; Comparison of trends predicted by ABBA-LSTM and ABBA-GRU, (a) from FC-1 at hour 590, (b) from FC-2 at hour 343.

In order to concretize the enhancement of the GRU model on the prediction performance, a comparison experiment between the ABBA-LSTM model and the ABBA-GRU model is arranged. In this case, the ABBA-LSTM model is set up in the same way as Chapter 4. For FC-1, one of the degradation trends predicted by each model at hour 590 is shown in Figure 5.8 (a). For FC-2, one of the degradation trends predicted by each model at hour 343 is shown in Figure 5.8 (b). The degradation trends predicted by the two models are similar, but there are differences in the computational costs. In comparison, the computational cost of the ABBA-GRU model is reduced by more than 30%, as in Table 5.5.

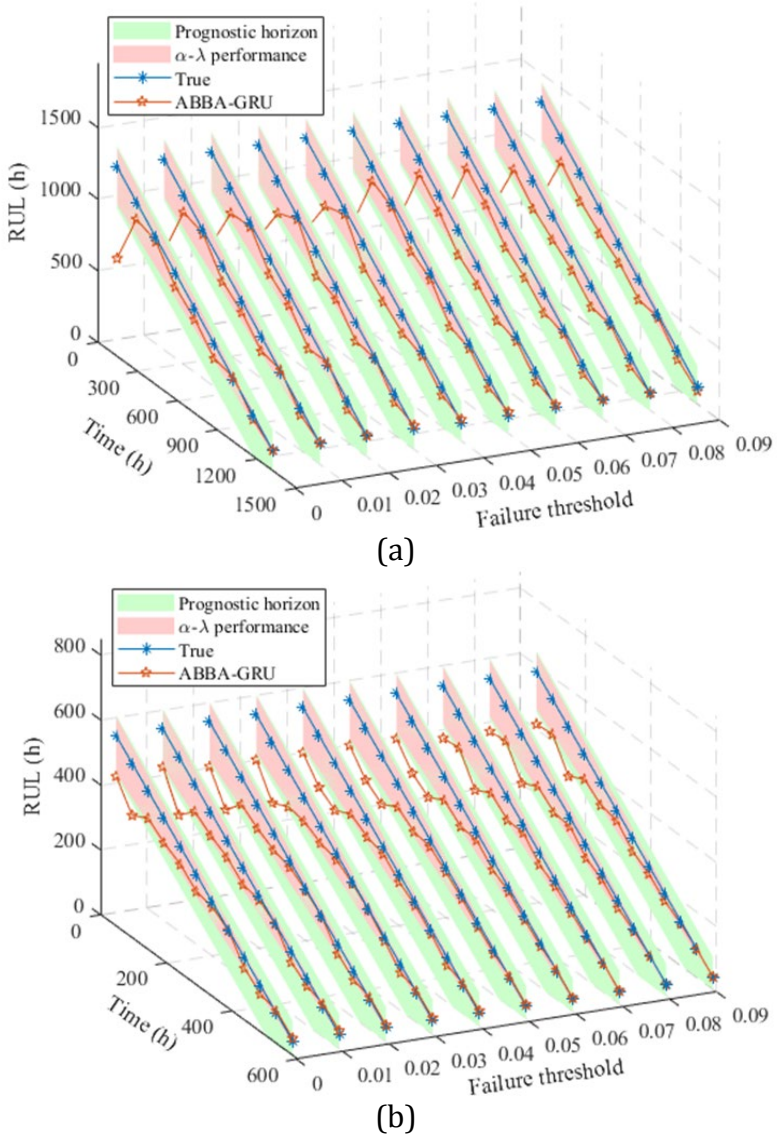

Figure 5.9 The predicted RULs at different failure thresholds from: (a) FC-1; (b) FC-2.

The ABBA-GRU model is deployed at each prognostics point and the RUL is predicted. The RUL prediction results for FC-1 and FC-2 are shown in Figure 5.9 (a) and (b), respectively. For FC-1, all PHs reach 1032.5 hours. Among all the 90 prognostics points under different failure thresholds, 63 points meet the $\alpha-\lambda$ performance requirements, with a passing rate of 70%. For FC-2, the maximum PH is 441 hours, the minimum is 392 hours, and the average is 411.6 hours. Among all the 120 prognostics points under

different failure thresholds, 92 points met the $\alpha-\lambda$ performance requirements, with a passing rate of 77%.

Method	Training duration (s)		Prediction duration (s)	
	FC-1	FC-2	FC-1	FC-2
ABBA-LSTM	689.42	524.26	53.59	49.22
ABBA-GRU	465.72	354.15	37.28	34.24

Table 5.5 Computational cost comparison of ABBA-LSTM and ABBA-GRU.

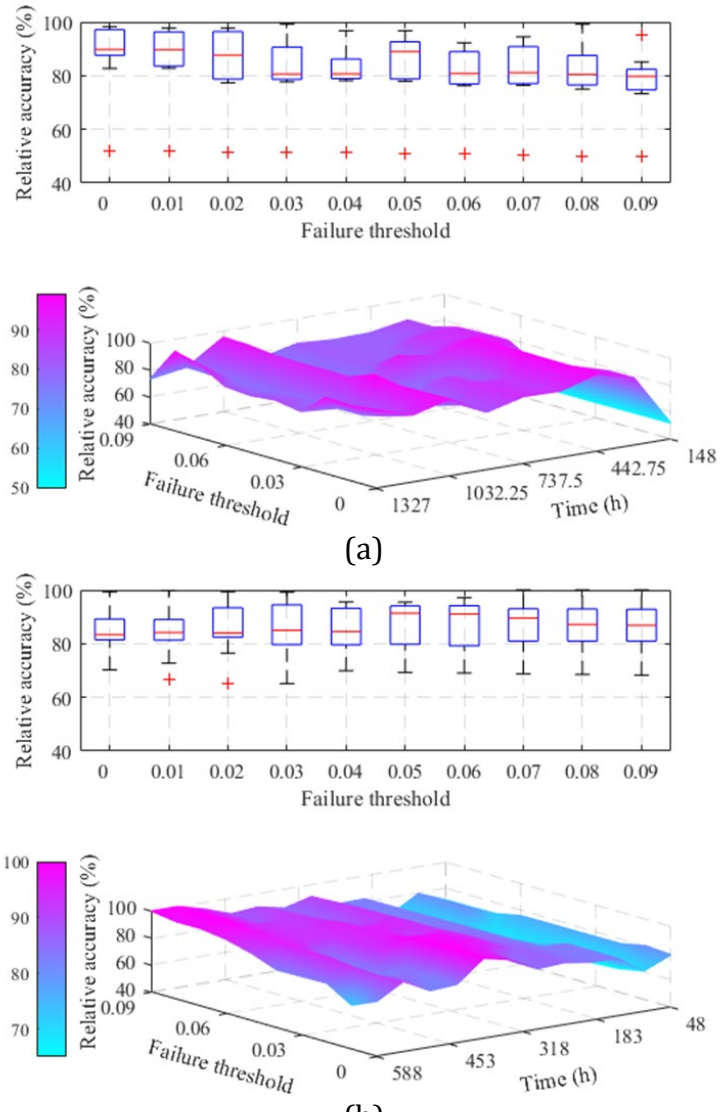

Figure 5.10 The distribution of RAs at different failure thresholds from: (a) FC-1; (b) FC-2.

Figure 5.10 (a) and (b) show the relative accuracies for FC-1 and FC-2, respectively. The red "+" in the upper part of Figure 5.10 (a) and (b) corresponds to the RA of outlier points. Overall, the accuracy of the prediction improves over time. The distribution of RA under different failure thresholds fluctuates slightly and is consistent overall. In summary, the prognostics performance of the proposed method is stable with satisfactory accuracy under different failure thresholds.

5.6. Discussion

In this Chapter, a data-driven prognostics approach is proposed for fuel cells under dynamic operating conditions. A Hilbert-Huang transform-based method is utilized to extract the health indicator from the dynamic voltage of fuel cells. The historical health indicator data is used to train the ABBA-GRU model, which in turn predicts the degradation trends and the remaining useful life of the stack. Dynamic load ageing experiments are carried out on two different types of fuel cells, and the prognostics approach is evaluated with the ageing data. The following conclusions can be summarized from the experimental and simulation results.

(1) The extracted health indicators characterize the inherent degradation behaviour of the stack voltage and the extraction method is computationally low-cost.
(2) The symbolic-based gated recurrent unit model provides a credible prognostics horizon of up to 2-6 weeks.
(3) While obtaining similar prediction performance as the ABBA-LSTM model, the computational cost of the ABBA-GRU model is reduced by 30%.
(4) The ABBA-GRU model exhibits satisfactory relative accuracy and consistency under multiple failure thresholds.

The above approach enhances real-time performance while providing a credible prognostics horizon and appropriate prediction accuracy. It facilitates the online deployment of the prognostics method.

6. Conclusion and perspectives

6.1. Main contributions summary

Shortage of durability is an essential factor limiting the large-scale commercial rollout of fuel cells. The prognostics technology is beneficial to provide suitable operating control and maintenance schedule that can enhance durability and reduce cost. This dissertation aims to address the challenges of extracting health indicators under variable load conditions, improving the accuracy/efficiency of predicting degradation states, enhancing the reliability of estimating remaining useful life, etc. The main contributions are summarized as follows.

A navigation sequence driven LSTM model for long-term prognostics is proposed. In this case, a navigation sequence is firstly generated by using an autoregressive integrated moving average model with exogenous variables. The sequence is then fed iteratively into LSTM in the implementation stage to achieve long-term perdition. The simulation and experimental results show that the cumulative error of multi-step prediction of the LSTM model is optimized. Prediction results are able to break through the limitations of historical degradation data. The proposed prognostics strategy has better long-term degradation trend prediction consistency and remaining useful life estimation robustness.

In order to extract reliable degradation indicators for prognostics in FC operating under variable load conditions and to improve the long-term prediction performance of the prognostics model. A fusion prognostics strategy is proposed. Specifically, the system dynamics is identified by using an electrochemical mechanism model and the degradation indexes are extracted based on the identified model parameters. Subsequently, a reduced-dimensional symbolic representation based long short-term memory network is developed for predicting the evolution of degradation. The degradation mechanism model can be used to identify degradation indexes in dynamic operating conditions. Based on the prognostics model, accurate RUL prediction can further be achieved over the extracted degradation indexes.

A hybrid "data-driven" + "data-driven" approach is proposed for fuel cell prognostics under dynamic operating conditions. Based on the modified HHT method, health indicators are extracted from the dynamic voltage of the fuel cell. The GRU model is used to replace the LSTM for improving the computational efficiency. The health indicators extracted by this method are reliable and the algorithm is computationally low-cost. This data-driven hybrid prognostics-based approach can provide a hundreds of hours prognostics horizon. Robust prognostics performance consistency is exhibited under several different failure thresholds.

6.2. Perspectives

Although the above work has been able to accurately extract and/or predict some of the health indicators, it is still not fully apply this result to diverse practical operating conditions of fuel cells.

In future work, efforts will be made to explore the effects of loading conditions on various degradation processes. Attempt to differentiate the degradation stages of fuel cells, e.g., according to the rate of degradation. Develop specific prognostics strategies for different degradation stages. In addition to variable loads, more variable operating parameters that may cause fuel cell performance degradation should be considered, such as ambient temperature, humidity, altitude, cleanliness of the air, etc. In parallel, the sensitivity of the prognostics models will be investigated under different practical operating conditions. Try to explore and focus on the commonality of degradation in different models/power fuel cells aiming to improve the prognostics model sensitivity.

In terms of historical degradation data processing, when recoverable performance loss is frequent, the prognostics is usually not satisfactory. Efforts to explore further separation of recoverable performance loss and inherent long-term degradation characteristics will hopefully alleviate this issue. For instance, the identification and removal of non-natural aging components from health indicators will be explored, as well as the appropriate combination of multiple health indicators to improve aging prediction performance.

In the area of life-extension-based operational control, efforts will be made to explore prognostics-based operational monitoring and maintenance decisions to extend the life of fuel cells. For instance, try to find out which operating conditions bring the least loss of fuel cell performance. This will be useful to support the life extension strategy.

Bibliography

[1] European Commission. (2020). *A hydrogen strategy for a climate-neutral Europe*.

[2] T. Ramsden, "2019 Annual Progress Report: DOE Hydrogen and Fuel Cells Program," United States, 2020.

[3] M. Yue, S. Jemei, N. Zerhouni, and R. Gouriveau, "Proton exchange membrane fuel cell system prognostics and decision-making: Current status and perspectives," *Renewable Energy,* vol. 179, pp. 2277-2294, 2021, doi: 10.1016/j.renene.2021.08.045.

[4] S. McQueen *et al.*, "Department of Energy Hydrogen Program Plan,"; US Department of Energy (USDOE), Washington DC (United States), 2020.

[5] H. Lohse-Busch, K. Stutenberg, M. Duoba, and S. Iliev, "Technology Assessment Of A Fuel Cell Vehicle: 2017 Toyota Mirai,"; Argonne National Lab. (ANL), Argonne, IL (United States), 2018.

[6] V. Das, S. Padmanaban, K. Venkitusamy, R. Selvamuthukumaran, F. Blaabjerg, and P. Siano, "Recent advances and challenges of fuel cell based power system architectures and control – A review," *Renewable and Sustainable Energy Reviews,* vol. 73, pp. 10-18, 2017, doi: 10.1016/j.rser.2017.01.148.

[7] D. Hart, S. Jones, and J. Lewis, "The Fuel Cell Industry Review 2020," 2020.

[8] D. Hart, F. Lehner, S. Jones, and J. Lewis, "The Fuel Cell Industry Review 2019," 2019.

[9] D. Hart, S. Jones, T. Houghton, X. Cordobes, and J. Lewis, "The Fuel Cell Industry Review 2021," 2021.

[10] H. Liu, J. Chen, D. Hissel, J. Lu, M. Hou, and Z. Shao, "Prognostics methods and degradation indexes of proton exchange membrane fuel cells: A review," *Renewable and Sustainable Energy Reviews,* vol. 123, 2020, doi: 10.1016/j.rser.2020.109721.

[11] Z. Hua, Z. Zheng, E. Pahon, M.-C. Péra, and F. Gao, "A review on lifetime prediction of proton exchange membrane fuel cells system," *Journal of Power Sources,* vol. 529, 2022, doi: 10.1016/j.jpowsour.2022.231256.

[12] M. Yue, S. Jemei, R. Gouriveau, and N. Zerhouni, "Review on health-conscious energy management strategies for fuel cell hybrid electric vehicles: Degradation models and strategies," *International Journal of Hydrogen Energy,* vol. 44, no. 13, pp. 6844-6861, 2019, doi: 10.1016/j.ijhydene.2019.01.190.

[13] X. Hao, Y. Yuan, H. Wang, and M. Ouyang, "Plug-in hybrid electric vehicle utility factor in China cities: Influencing factors, empirical research, and energy and environmental application," *eTransportation,* 2021, doi: 10.1016/j.etran.2021.100138.

[14] Z. Hu, L. Xu, J. Li, M. Ouyang, Z. Song, and H. Huang, "A reconstructed fuel cell life-prediction model for a fuel cell hybrid city bus," *Energy Conversion and Management,* vol. 156, pp. 723-732, 2018, doi: 10.1016/j.enconman.2017.11.069.

[15] H. Peng *et al.*, "A comparison of various universally applicable power distribution strategies for fuel cell hybrid trains utilizing component modeling at different levels of detail: From simulation to test bench measurement," *eTransportation,* vol. 9, 2021, doi: 10.1016/j.etran.2021.100120.

[16] A. Pfeifer, P. Prebeg, and N. Duić, "Challenges and opportunities of zero emission shipping in smart islands: A study of zero emission ferry lines," *eTransportation,* vol. 3, 2020, doi: 10.1016/j.etran.2020.100048.

[17] W. Gao *et al.*, "All-condition economy evaluation method for fuel cell systems: System efficiency contour map," *eTransportation,* vol. 9, 2021, doi: 10.1016/j.etran.2021.100127.

[18] L. Eudy and M. B. Post, "Fuel Cell Buses in U.S. Transit Fleets: Current Status 2018,"; National Renewable Energy Lab. (NREL), Golden, CO (United States), NREL/TP-5400-72208 United States 10.2172/1489893 NREL English, 2019.

[19] T. Sutharssan, D. Montalvao, Y. K. Chen, W.-C. Wang, C. Pisac, and H. Elemara, "A review on prognostics and health monitoring of proton exchange membrane fuel cell," *Renewable and Sustainable Energy Reviews,* vol. 75, pp. 440-450, 2017, doi: 10.1016/j.rser.2016.11.009.

[20] C. Lorenzo, D. Bouquain, S. Hibon, and D. Hissel, "Synthesis of degradation mechanisms and of their impacts on degradation rates on proton-exchange membrane fuel cells and lithium-ion nickel–manganese–cobalt batteries in hybrid transport applications," *Reliability Engineering & System Safety,* vol. 212, 2021, doi: 10.1016/j.ress.2020.107369.

[21] J. M. Kurtz, S. Sprik, G. Saur, and S. Onorato, "Fuel cell electric vehicle durability and fuel cell

performance," National Renewable Energy Lab.(NREL), Golden, CO (United States), 2019.
[22] O. Z. Sharaf and M. F. Orhan, "An overview of fuel cell technology: Fundamentals and applications," *Renewable and Sustainable Energy Reviews,* vol. 32, pp. 810-853, 2014, doi: 10.1016/j.rser.2014.01.012.
[23] U. Lucia, "Overview on fuel cells," *Renewable and Sustainable Energy Reviews,* vol. 30, pp. 164-169, 2014, doi: 10.1016/j.rser.2013.09.025.
[24] Z. Huang, J. Shen, S. H. Chan, and Z. Tu, "Transient response of performance in a proton exchange membrane fuel cell under dynamic loading," *Energy Conversion and Management,* vol. 226, 2020, doi: 10.1016/j.enconman.2020.113492.
[25] E. Zio, "Prognostics and Health Management (PHM): Where are we and where do we (need to) go in theory and practice," *Reliability Engineering & System Safety,* vol. 218, 2022, doi: 10.1016/j.ress.2021.108119.
[26] Y. Hu, X. Miao, Y. Si, E. Pan, and E. Zio, "Prognostics and health management: A review from the perspectives of design, development and decision," *Reliability Engineering & System Safety,* vol. 217, 2022, doi: 10.1016/j.ress.2021.108063.
[27] M. Jouin, R. Gouriveau, D. Hissel, M.-C. Péra, and N. Zerhouni, "Degradations analysis and aging modeling for health assessment and prognostics of PEMFC," *Reliability Engineering & System Safety,* vol. 148, pp. 78-95, 2016, doi: 10.1016/j.ress.2015.12.003.
[28] M. Jouin, R. Gouriveau, D. Hissel, M. C. Pera, and N. Zerhouni, "Prognostics of PEM fuel cell in a particle filtering framework," *International Journal of Hydrogen Energy,* vol. 39, no. 1, pp. 481-494, Jan 2014, doi: 10.1016/j.ijhydene.2013.10.054.
[29] E. Lechartier, E. Laffly, M.-C. Péra, R. Gouriveau, D. Hissel, and N. Zerhouni, "Proton exchange membrane fuel cell behavioral model suitable for prognostics," *International Journal of Hydrogen Energy,* vol. 40, no. 26, pp. 8384-8397, 2015, doi: 10.1016/j.ijhydene.2015.04.099.
[30] M. Jouin *et al.*, "Estimating the end-of-life of PEM fuel cells: Guidelines and metrics," *Applied Energy,* vol. 177, pp. 87-97, 2016, doi: 10.1016/j.apenergy.2016.05.076.
[31] A. Jacome, D. Hissel, V. Heiries, M. Gerard, and S. Rosini, "Prognostic methods for proton exchange membrane fuel cell under automotive load cycling: a review," *IET Electrical Systems in Transportation,* vol. 10, no. 4, pp. 369-375, 2020, doi: 10.1049/iet-est.2020.0045.
[32] *ISO 13381-1:2015 Condition monitoring and diagnostics of machines — prognostics — Part 1: General Guidelines*, ISO, 2015.
[33] R. Ma *et al.*, "Data-Fusion Prognostics of Proton Exchange Membrane Fuel Cell Degradation," *IEEE Transactions on Industry Applications,* vol. 55, no. 4, pp. 4321-4331, 2019, doi: 10.1109/tia.2019.2911846.
[34] C. Wang, Z. Li, R. Outbib, D. Zhao, and M. Dou, "Proton Exchange Membrane Fuel Cells Prognostic Strategy Based on Navigation Sequence Driven Long Short-term Memory Networks," in *IECON 2020 The 46th Annual Conference of the IEEE Industrial Electronics Society*, 2020: IEEE, pp. 3969-3974.
[35] F. K. Wang, X. B. Cheng, and K. C. Hsiao, "Stacked long short-term memory model for proton exchange membrane fuel cell systems degradation," *Journal of Power Sources,* vol. 448, Feb 2020, Art no. 227591, doi: 10.1016/j.jpowsour.2019.227591.
[36] R. Ma, T. Yang, E. Breaz, Z. Li, P. Briois, and F. Gao, "Data-driven proton exchange membrane fuel cell degradation predication through deep learning method," *Applied Energy,* vol. 231, pp. 102-115, 2018, doi: 10.1016/j.apenergy.2018.09.111.
[37] H. Chen *et al.*, "Whole life cycle performance degradation test and RUL prediction research of fuel cell MEA," *Applied Energy,* vol. 310, Mar 2022, Art no. 118556, doi: 10.1016/j.apenergy.2022.118556.
[38] R. Gouriveau, M. Hilairet, D. Hissel, S. Jemei, M. Jouin, and E. Lechartier, "IEEE PHM 2014 data challenge: outline, experiments, scoring of results, winners," FCLAB, Belfort, France, 2014.
[39] R. E. Silva *et al.*, "Proton exchange membrane fuel cell degradation prediction based on Adaptive Neuro-Fuzzy Inference Systems," *International Journal of Hydrogen Energy,* vol. 39, no. 21, pp. 11128-11144, Jul 2014, doi: 10.1016/j.ijhydene.2014.05.005.
[40] M. Ibrahim, N. Y. Steiner, S. Jemei, and D. Hissel, "Wavelet-Based Approach for Online Fuel Cell Remaining Useful Lifetime Prediction," *IEEE Transactions on Industrial Electronics,* vol. 63, no. 8, pp. 5057-5068, 2016, Art no. 7442113, doi: 10.1109/TIE.2016.2547358.
[41] K. Javed, R. Gouriveau, N. Zerhouni, and D. Hissel, "Prognostics of Proton Exchange Membrane Fuel Cells stack using an ensemble of constraints based connectionist networks," *Journal of Power Sources,* vol. 324, pp. 745-757, 2016, doi: 10.1016/j.jpowsour.2016.05.092.
[42] M. S. Jha, M. Bressel, B. Ould-Bouamama, and G. Dauphin-Tanguy, "Particle filter based hybrid prognostics of proton exchange membrane fuel cell in bond graph framework," *Computers & Chemical Engineering,* vol. 95, pp. 216-230, Dec 2016, doi: 10.1016/j.compchemeng.2016.08.018.
[43] T. Kim, H. Oh, H. Kim, and B. D. Youn, "An Online-Applicable Model for Predicting Health

Degradation of PEM Fuel Cells with Root Cause Analysis," *IEEE Transactions on Industrial Electronics,* vol. 63, no. 11, pp. 7094-7103, 2016, Art no. 7501842, doi: 10.1109/TIE.2016.2586022.

[44] J. Chen, D. Zhou, C. Lyu, and C. Lu, "A novel health indicator for PEMFC state of health estimation and remaining useful life prediction," *International Journal of Hydrogen Energy,* vol. 42, no. 31, pp. 20230-20238, 2017, doi: 10.1016/j.ijhydene.2017.05.241.

[45] H. Liu, J. Chen, M. Hou, Z. Shao, and H. Su, "Data-based short-term prognostics for proton exchange membrane fuel cells," *International Journal of Hydrogen Energy,* vol. 42, no. 32, pp. 20791-20808, 2017, doi: 10.1016/j.ijhydene.2017.06.180.

[46] L. Mao, L. Jackson, and T. Jackson, "Investigation of polymer electrolyte membrane fuel cell internal behaviour during long term operation and its use in prognostics," *Journal of Power Sources,* vol. 362, pp. 39-49, 2017, doi: 10.1016/j.jpowsour.2017.07.018.

[47] D. Zhou, F. Gao, E. Breaz, A. Ravey, and A. Miraoui, "Degradation prediction of PEM fuel cell using a moving window based hybrid prognostic approach," *Energy,* vol. 138, pp. 1175-1186, 2017, doi: 10.1016/j.energy.2017.07.096.

[48] Y. Cheng, N. Zerhouni, and C. Lu, "A hybrid remaining useful life prognostic method for proton exchange membrane fuel cell," *International Journal of Hydrogen Energy,* vol. 43, no. 27, pp. 12314-12327, 2018, doi: 10.1016/j.ijhydene.2018.04.160.

[49] D. Zhang, C. Cadet, N. Yousfi-Steiner, and C. Bérenguer, "Proton exchange membrane fuel cell remaining useful life prognostics considering degradation recovery phenomena," *Proceedings of the Institution of Mechanical Engineers, Part O: Journal of Risk and Reliability,* vol. 232, no. 4, pp. 415-424, 2018, doi: 10.1177/1748006X18776825.

[50] D. Zhou, A. Al-Durra, K. Zhang, A. Ravey, and F. Gao, "Online remaining useful lifetime prediction of proton exchange membrane fuel cells using a novel robust methodology," *Journal of Power Sources,* vol. 399, pp. 314-328, 2018, doi: 10.1016/j.jpowsour.2018.06.098.

[51] L. Zhu and J. Chen, "Prognostics of PEM fuel cells based on Gaussian process state space models," *Energy,* vol. 149, pp. 63-73, 2018, doi: 10.1016/j.energy.2018.02.016.

[52] K. Chen, S. Laghrouche, and A. Djerdir, "Degradation prediction of proton exchange membrane fuel cell based on grey neural network model and particle swarm optimization," *Energy Conversion and Management,* vol. 195, pp. 810-818, Sep 2019, doi: 10.1016/j.enconman.2019.05.045.

[53] H. Liu, J. Chen, D. Hissel, M. Hou, and Z. G. Shao, "A multi-scale hybrid degradation index for proton exchange membrane fuel cells," *Journal of Power Sources,* vol. 437, Oct 2019, Art no. 226916, doi: 10.1016/j.jpowsour.2019.226916.

[54] H. Liu, J. Chen, D. Hissel, and H. Su, "Remaining useful life estimation for proton exchange membrane fuel cells using a hybrid method," *Applied Energy,* vol. 237, pp. 910-919, 2019, doi: 10.1016/j.apenergy.2019.01.023.

[55] H. Liu, J. Chen, D. Hissel, and H. Su, "Short-Term Prognostics of PEM Fuel Cells: A Comparative and Improvement Study," *IEEE Transactions on Industrial Electronics,* vol. 66, no. 8, pp. 6077-6086, 2019, Art no. 8482479, doi: 10.1109/TIE.2018.2873105.

[56] J. Liu, Q. Li, W. Chen, Y. Yan, Y. Qiu, and T. Cao, "Remaining useful life prediction of PEMFC based on long short-term memory recurrent neural networks," *International Journal of Hydrogen Energy,* vol. 44, no. 11, pp. 5470-5480, 2019, doi: 10.1016/j.ijhydene.2018.10.042.

[57] J. W. Liu *et al.*, "PEMFC Residual Life Prediction Using Sparse Autoencoder-Based Deep Neural Network," *Ieee Transactions on Transportation Electrification,* vol. 5, no. 4, pp. 1279-1293, Dec 2019, doi: 10.1109/tte.2019.2946065.

[58] J. Liu, Q. Li, W. Chen, X. Wang, and Y. Yan, "Remaining Useful Life Prediction Method of PEMFC Based on Kernel Extreme Learning Machine and Locally Weighted Scatterplot Smoothing," *Zhongguo Dianji Gongcheng Xuebao/Proceedings of the Chinese Society of Electrical Engineering,* Article vol. 39, no. 24, pp. 7272-7279, 2019, doi: 10.13334/j.0258-8013.pcsee.181614.

[59] K. Chen, S. Laghrouche, and A. Djerdir, "Proton Exchange Membrane Fuel Cell Prognostics Using Genetic Algorithm and Extreme Learning Machine," *Fuel Cells,* vol. 20, no. 3, pp. 263-271, 2020, doi: 10.1002/fuce.201900085.

[60] K. Chen, S. Laghrouche, and A. Djerdir, "Aging prognosis model of proton exchange membrane fuel cell in different operating conditions," *International Journal of Hydrogen Energy,* vol. 45, no. 20, pp. 11761-11772, 2020, doi: 10.1016/j.ijhydene.2020.02.085.

[61] K. He, C. Zhang, Q. He, Q. Wu, L. Jackson, and L. Mao, "Effectiveness of PEMFC historical state and operating mode in PEMFC prognosis," *International Journal of Hydrogen Energy,* vol. 45, no. 56, pp. 32355-32366, 2020, doi: 10.1016/j.ijhydene.2020.08.149.

[62] Z. Hua, Z. Zheng, M.-C. Péra, and F. Gao, "Remaining useful life prediction of PEMFC systems based on the multi-input echo state network," *Applied Energy,* vol. 265, 2020, doi: 10.1016/j.apenergy.2020.114791.

[63] R. Pan, D. Yang, Y. Wang, and Z. Chen, "Performance degradation prediction of proton exchange membrane fuel cell using a hybrid prognostic approach," *International Journal of Hydrogen Energy,* vol. 45, no. 55, pp. 30994-31008, 2020, doi: 10.1016/j.ijhydene.2020.08.082.

[64] R. Pan, D. Yang, Y. J. Wang, and Z. H. Chen, "Health degradation assessment of proton exchange membrane fuel cell based on an analytical equivalent circuit model," *Energy,* vol. 207, Sep 2020, Art no. 118185, doi: 10.1016/j.energy.2020.118185.

[65] F. K. Wang, T. Mamo, and X. B. Cheng, "Bi-directional long short-term memory recurrent neural network with attention for stack voltage degradation from proton exchange membrane fuel cells," *Journal of Power Sources,* vol. 461, Jun 2020, Art no. 228170, doi: 10.1016/j.jpowsour.2020.228170.

[66] R. Xie, R. Ma, S. Pu, L. Xu, D. Zhao, and Y. Huangfu, "Prognostic for fuel cell based on particle filter and recurrent neural network fusion structure," *Energy and AI,* vol. 2, 2020, Art no. 100017, doi: 10.1016/j.egyai.2020.100017.

[67] Y. C. Xie, J. X. Zou, C. Peng, Y. Zhu, and F. Gao, "A novel PEM fuel cell remaining useful life prediction method based on singular spectrum analysis and deep Gaussian processes," *International Journal of Hydrogen Energy,* vol. 45, no. 55, pp. 30942-30956, Nov 2020, doi: 10.1016/j.ijhydene.2020.08.052.

[68] Y. J. Ao, S. Laghrouche, D. Depernet, and K. Chen, "Proton Exchange Membrane Fuel Cell Prognosis Based on Frequency-Domain Kalman Filter," *Ieee Transactions on Transportation Electrification,* vol. 7, no. 4, pp. 2332-2343, Dec 2021, doi: 10.1109/tte.2021.3077506.

[69] K. Chen, S. Laghrouche, and A. Djerdir, "Health state prognostic of fuel cell based on wavelet neural network and cuckoo search algorithm," *ISA Transactions,* vol. 113, pp. 175-184, 2021, doi: 10.1016/j.isatra.2020.03.012.

[70] K. He, L. Mao, J. Yu, W. Huang, Q. He, and L. Jackson, "Long-Term Performance Prediction of PEMFC Based on LASSO-ESN," *IEEE Transactions on Instrumentation and Measurement,* vol. 70, 2021, Art no. 9351964, doi: 10.1109/TIM.2021.3058365.

[71] J. Jin, Y. Chen, C. Xie, W. Zhu, and F. Wu, "Remaining useful life prediction of PEMFC based on cycle reservoir with jump model," *International Journal of Hydrogen Energy,* vol. 46, no. 80, pp. 40001-40013, 2021, doi: 10.1016/j.ijhydene.2021.09.233.

[72] R. Ma, R. Xie, L. Xu, Y. Huangfu, and Y. Li, "A Hybrid Prognostic Method for PEMFC with Aging Parameter Prediction," *IEEE Transactions on Transportation Electrification,* vol. 7, no. 4, pp. 2318-2331, 2021, doi: 10.1109/TTE.2021.3075531.

[73] F. K. Wang, C. Y. Huang, T. Mamo, and X. B. Cheng, "Ensemble model for the degradation prediction of proton exchange membrane fuel cell stacks," *Quality and Reliability Engineering International,* vol. 37, no. 1, pp. 34-46, Feb 2021, doi: 10.1002/qre.2718.

[74] P. Wang *et al.*, "A novel degradation model of proton exchange membrane fuel cells for state of health estimation and prognostics," *International Journal of Hydrogen Energy,* vol. 46, no. 61, pp. 31353-31361, 2021, doi: 10.1016/j.ijhydene.2021.07.004.

[75] Z. Zhang, Y. X. Wang, H. He, and F. Sun, "A short- and long-term prognostic associating with remaining useful life estimation for proton exchange membrane fuel cell," *Applied Energy,* vol. 304, 2021, Art no. 117841, doi: 10.1016/j.apenergy.2021.117841.

[76] B. Zuo, J. S. Cheng, and Z. H. Zhang, "Degradation prediction model for proton exchange membrane fuel cells based on long short-term memory neural network and Savitzky-Golay filter," *International Journal of Hydrogen Energy,* vol. 46, no. 29, pp. 15928-15937, Apr 2021, doi: 10.1016/j.ijhydene.2021.02.069.

[77] K. Benaggoune, M. L. Yue, S. Jemei, and N. Zerhouni, "A data-driven method for multi-step-ahead prediction and long-term prognostics of proton exchange membrane fuel cell," *Applied Energy,* vol. 313, May 2022, Art no. 118835, doi: 10.1016/j.apenergy.2022.118835.

[78] K. Chen, S. Laghrouche, and A. Djerdir, "Remaining Useful Life Prediction for Fuel Cell Based on Support Vector Regression and Grey Wolf Optimizer Algorithm," *Ieee Transactions on Energy Conversion,* vol. 37, no. 2, pp. 778-787, Jun 2022, doi: 10.1109/tec.2021.3121650.

[79] Z. Deng *et al.*, "Degradation Prediction of PEMFCs Using Stacked Echo State Network Based on Genetic Algorithm Optimization," *IEEE Transactions on Transportation Electrification,* vol. 8, no. 1, pp. 1454-1466, 2022, doi: 10.1109/TTE.2021.3111906.

[80] Z. Hua, Z. Zheng, E. Pahon, M. C. Pera, and F. Gao, "Lifespan Prediction for Proton Exchange Membrane Fuel Cells Based on Wavelet Transform and Echo State Network," *IEEE Transactions on Transportation Electrification,* vol. 8, no. 1, pp. 420-431, 2022, doi: 10.1109/TTE.2021.3121179.

[81] M. Z. Pan, P. F. Hu, R. Gao, and K. Liang, "Multistep prediction of remaining useful life of proton exchange membrane fuel cell based on temporal convolutional network," *International Journal of Green Energy,* 2022, doi: 10.1080/15435075.2022.2050377.

[82] Y. M. Wu, E. Breaz, F. Gao, and A. Miraoui, "A Modified Relevance Vector Machine for PEM Fuel-

Cell Stack Aging Prediction," *Ieee Transactions on Industry Applications,* vol. 52, no. 3, pp. 2573-2581, May-Jun 2016, doi: 10.1109/tia.2016.2524402.

[83] Y. M. Wu, E. Breaz, F. Gao, D. Paire, and A. Miraoui, "Nonlinear Performance Degradation Prediction of Proton Exchange Membrane Fuel Cells Using Relevance Vector Machine," *Ieee Transactions on Energy Conversion,* vol. 31, no. 4, pp. 1570-1582, Dec 2016, doi: 10.1109/tec.2016.2582531.

[84] D. M. Zhou, Y. M. Wu, F. Gao, E. Breaz, A. Ravey, and A. Miraoui, "Degradation Prediction of PEM Fuel Cell Stack Based on Multiphysical Aging Model With Particle Filter Approach," *Ieee Transactions on Industry Applications,* vol. 53, no. 4, pp. 4041-4052, Jul-Aug 2017, doi: 10.1109/tia.2017.2680406.

[85] Z. Li, Z. Zheng, and R. Outbib, "Adaptive prognostic of fuel cells by implementing ensemble echo state networks in time-varying model space," *IEEE Transactions on Industrial Electronics,* vol. 67, no. 1, pp. 379-389, 2020, Art no. 8626772, doi: 10.1109/TIE.2019.2893827.

[86] J. Ma *et al.*, "Degradation prognosis for proton exchange membrane fuel cell based on hybrid transfer learning and intercell differences," *ISA Transactions,* vol. 113, pp. 149-165, 2021, doi: 10.1016/j.isatra.2020.06.005.

[87] S. Meraghni, L. S. Terrissa, M. Yue, J. Ma, S. Jemei, and N. Zerhouni, "A data-driven digital-twin prognostics method for proton exchange membrane fuel cell remaining useful life prediction," *International Journal of Hydrogen Energy,* vol. 46, no. 2, pp. 2555-2564, 2021, doi: 10.1016/j.ijhydene.2020.10.108.

[88] M. Bressel, M. Hilairet, D. Hissel, and B. O. Bouamama, "Extended Kalman Filter for prognostic of Proton Exchange Membrane Fuel Cell," *Applied Energy,* vol. 164, pp. 220-227, Feb 2016, doi: 10.1016/j.apenergy.2015.11.071.

[89] M. Jouin, R. Gouriveau, D. Hissel, M. C. Pera, and N. Zerhouni, "Joint Particle Filters Prognostics for Proton Exchange Membrane Fuel Cell Power Prediction at Constant Current Solicitation," *Ieee Transactions on Reliability,* vol. 65, no. 1, pp. 336-349, Mar 2016, doi: 10.1109/tr.2015.2454499.

[90] S. Morando, S. Jemei, D. Hissel, R. Gouriveau, and N. Zerhouni, "Proton exchange membrane fuel cell ageing forecasting algorithm based on Echo State Network," *International Journal of Hydrogen Energy,* vol. 42, no. 2, pp. 1472-1480, 2017, doi: 10.1016/j.ijhydene.2016.05.286.

[91] C. Robin, M. Gerard, M. Quinaud, J. d'Arbigny, and Y. Bultel, "Proton exchange membrane fuel cell model for aging predictions: Simulated equivalent active surface area loss and comparisons with durability tests," *Journal of Power Sources,* vol. 326, pp. 417-427, Sep 2016, doi: 10.1016/j.jpowsour.2016.07.018.

[92] J. Zhao and X. Li, "A review of polymer electrolyte membrane fuel cell durability for vehicular applications: Degradation modes and experimental techniques," *Energy Conversion and Management,* vol. 199, 2019, doi: 10.1016/j.enconman.2019.112022.

[93] M. Ou *et al.*, "A novel approach based on semi-empirical model for degradation prediction of fuel cells," *Journal of Power Sources,* vol. 488, 2021, Art no. 229435, doi: 10.1016/j.jpowsour.2020.229435.

[94] K. Chen, S. Laghrouche, and A. Djerdir, "Fuel cell health prognosis using Unscented Kalman Filter: Postal fuel cell electric vehicles case study," *International Journal of Hydrogen Energy,* vol. 44, no. 3, pp. 1930-1939, 2019, doi: 10.1016/j.ijhydene.2018.11.100.

[95] K. Chen, S. Laghrouche, and A. Djerdir, "Degradation model of proton exchange membrane fuel cell based on a novel hybrid method," *Applied Energy,* vol. 252, 2019, doi: 10.1016/j.apenergy.2019.113439.

[96] M. Bressel, M. Hilairet, D. Hissel, and B. O. Bouamama, "Remaining Useful Life Prediction and Uncertainty Quantification of Proton Exchange Membrane Fuel Cell Under Variable Load," *Ieee Transactions on Industrial Electronics,* vol. 63, no. 4, pp. 2569-2577, Apr 2016, doi: 10.1109/tie.2016.2519328.

[97] E. Pahon *et al.*, "Long-term tests duration reduction for PEMFC mu-CHP application," *International Journal of Hydrogen Energy,* vol. 42, no. 2, pp. 1527-1533, Jan 2017, doi: 10.1016/j.ijhydene.2016.06.222.

[98] Z. Hua, Z. Zheng, E. Pahon, M. C. Péra, and F. Gao, "Remaining useful life prediction of PEMFC systems under dynamic operating conditions," *Energy Conversion and Management,* vol. 231, 2021, Art no. 113825, doi: 10.1016/j.enconman.2021.113825.

[99] Z. Hua, Z. Zheng, E. Pahon, M. C. Pera, and F. Gao, "Multi-Timescale Lifespan Prediction for PEMFC Systems under Dynamic Operating Conditions," *IEEE Transactions on Transportation Electrification,* vol. 8, no. 1, pp. 345-355, 2022, doi: 10.1109/TTE.2021.3103921.

[100] J. Zuo *et al.*, "Deep learning based prognostic framework towards proton exchange membrane fuel cell for automotive application," *Applied Energy,* vol. 281, 2021, doi: 10.1016/j.apenergy.2020.115937.

[101] R. Mezzi, N. Yousfi-Steiner, M. C. Pera, D. Hissel, and L. Larger, "An Echo State Network for fuel cell lifetime prediction under a dynamic micro-cogeneration load profile," *Applied Energy,* vol. 283, Feb 2021, Art no. 116297, doi: 10.1016/j.apenergy.2020.116297.

[102] M. Liu, D. Wu, C. Yin, Y. Gao, K. Li, and H. Tang, "Prediction of voltage degradation trend for a proton exchange membrane fuel cell city bus on roads," *Journal of Power Sources,* vol. 512, 2021, Art no. 230435, doi: 10.1016/j.jpowsour.2021.230435.

[103] M. Yue, Z. Li, R. Roche, S. Jemei, and N. Zerhouni, "Degradation identification and prognostics of proton exchange membrane fuel cell under dynamic load," *Control Engineering Practice,* vol. 118, 2022, Art no. 104959, doi: 10.1016/j.conengprac.2021.104959.

[104] L. Vichard, F. Harel, A. Ravey, P. Venet, and D. Hissel, "Degradation prediction of PEM fuel cell based on artificial intelligence," *International Journal of Hydrogen Energy,* vol. 45, no. 29, pp. 14953-14963, 2020, doi: 10.1016/j.ijhydene.2020.03.209.

[105] M. Yue, Z. Li, R. Roche, S. Jemei, and N. Zerhouni, "A Feature-based Prognostics Strategy For PEM Fuel Cell Operated Under Dynamic Conditions," in *Prognostics and System Health Management Conference (PHM-Besancon)*, Besancon, FRANCE, 2020, pp. 122-127, doi: 10.1109/PHM-Besancon49106.2020.00026.

[106] Z. L. Li, S. Jemei, R. Gouriveau, D. Hissel, N. Zerhouni, and Ieee, "Remaining useful life estimation for PEMFC in dynamic operating conditions," in *2016 Ieee Vehicle Power and Propulsion Conference*, (IEEE Vehicle Power and Propulsion Conference, 2016.

[107] C. Wang, Z. Li, R. Outbib, M. Dou, and D. Zhao, "A novel long short-term memory networks-based data-driven prognostic strategy for proton exchange membrane fuel cells," *International Journal of Hydrogen Energy,* vol. 47, no. 18, pp. 10395-10408, 2022, doi: 10.1016/j.ijhydene.2022.01.121.

[108] H. Liu, J. Chen, C. Y. Zhu, H. Y. Su, and M. Hou, "Prognostics of Proton Exchange Membrane Fuel Cells Using A Model-based Method," *Ifac Papersonline,* vol. 50, no. 1, pp. 4757-4762, 2017, doi: 10.1016/j.ifacol.2017.08.947.

[109] S. Elsworth and S. Güttel, "Time series forecasting using LSTM networks: A symbolic approach," *arXiv preprint arXiv:2003.05672,* 2020.

[110] J. Larminie, A. Dicks, and M. S. McDonald, *Fuel cell systems explained*. J. Wiley Chichester, UK, 2003.

[111] M. Mohammadi Taghiabadi and M. Zhiani, "Degradation analysis of dead-ended anode PEM fuel cell at the low and high thermal and pressure conditions," *International Journal of Hydrogen Energy,* vol. 44, no. 10, pp. 4985-4995, 2019, doi: 10.1016/j.ijhydene.2019.01.040.

[112] R. O'hayre, S.-W. Cha, W. Colella, and F. B. Prinz, *Fuel cell fundamentals*. John Wiley & Sons, 2016.

[113] G. K, K. M, and U. S, "An intelligent parametric modeling and identification of a 5 kW ballard PEM fuel cell system based on dynamic recurrent networks with delayed context units," *International Journal of Hydrogen Energy,* vol. 46, no. 29, pp. 15912-15927, 2021, doi: 10.1016/j.ijhydene.2021.02.065.

[114] G. E. Box, G. M. Jenkins, G. C. Reinsel, and G. M. Ljung, *Time series analysis: forecasting and control*. John Wiley & Sons, 2015.

[115] A. Jalalkamali, M. Moradi, and N. Moradi, "Application of several artificial intelligence models and ARIMAX model for forecasting drought using the Standardized Precipitation Index," *International Journal of Environmental Science and Technology,* vol. 12, no. 4, pp. 1201-1210, 2014, doi: 10.1007/s13762-014-0717-6.

[116] D. P. Kingma and J. Ba, "Adam: A method for stochastic optimization," *arXiv preprint arXiv:1412.6980,* 2014.

[117] F. J. Asensio, J. I. San Martín, I. Zamora, G. Saldaña, and O. Oñederra, "Analysis of electrochemical and thermal models and modeling techniques for polymer electrolyte membrane fuel cells," *Renewable and Sustainable Energy Reviews,* vol. 113, 2019, doi: 10.1016/j.rser.2019.109283.

[118] L. Ljung, "Experiments with identification of continuous time models," in *IFAC Proceedings Volumes (IFAC-PapersOnline)*, 2009, vol. 15, PART 1 ed., pp. 1175-1180, doi: 10.3182/20090706-3-FR-2004.0209.

[119] C. Gong, J. Shen, Y. Yu, K. Wang, and Z. Tu, "A novel radiator structure for enhanced heat transfer used in PEM fuel cell vehicle," *International Journal of Heat and Mass Transfer,* vol. 157, 2020, doi: 10.1016/j.ijheatmasstransfer.2020.119926.

[120] B. Chen, Y. Cai, Z. Tu, S. H. Chan, J. Wang, and Y. Yu, "Gas purging effect on the degradation characteristic of a proton exchange membrane fuel cell with dead-ended mode operation I. With different electrolytes," *Energy,* vol. 141, pp. 40-49, 2017, doi: 10.1016/j.energy.2017.09.067.

[121] S. Elsworth and S. Güttel, "ABBA: Adaptive Brownian bridge-based symbolic aggregation of time series," *Data Mining and Knowledge Discovery,* vol. 34, pp. 1175-1200, 2020.

[122] J. Zuo *et al.*, "Long-term dynamic durability test datasets for single proton exchange membrane fuel cell," *Data Brief,* vol. 35, p. 106775, Apr 2021, doi: 10.1016/j.dib.2021.106775.

[123] A. Saxena *et al.*, "Metrics for evaluating performance of prognostic techniques," in *International Conference on Prognostics & Health Management*, 2008.

[124] A. Theissler, J. Pérez-Velázquez, M. Kettelgerdes, and G. Elger, "Predictive maintenance enabled by machine learning: Use cases and challenges in the automotive industry," *Reliability Engineering & System Safety,* vol. 215, 2021, doi: 10.1016/j.ress.2021.107864.
[125] Z. Xu and J. H. Saleh, "Machine learning for reliability engineering and safety applications: Review of current status and future opportunities," *Reliability Engineering & System Safety,* vol. 211, 2021, doi: 10.1016/j.ress.2021.107530.
[126] N. E. Huang *et al.*, "The empirical mode decomposition and the Hilbert spectrum for nonlinear and non-stationary time series analysis," *Proceedings of the Royal Society a-Mathematical Physical and Engineering Sciences,* vol. 454, no. 1971, pp. 903-995, Mar 1998, doi: 10.1098/rspa.1998.0193.
[127] U. B. d. Souza, J. P. L. Escola, and L. d. C. Brito, "A survey on Hilbert-Huang transform: Evolution, challenges and solutions," *Digital Signal Processing,* vol. 120, 2022, doi: 10.1016/j.dsp.2021.103292.
[128] Y. Chang, H. Fang, and Y. Zhang, "A new hybrid method for the prediction of the remaining useful life of a lithium-ion battery," *Applied Energy,* vol. 206, pp. 1564-1578, 2017, doi: 10.1016/j.apenergy.2017.09.106.
[129] J. C. Chen, T.-L. Chen, W.-J. Liu, C. C. Cheng, and M.-G. Li, "Combining empirical mode decomposition and deep recurrent neural networks for predictive maintenance of lithium-ion battery," *Advanced Engineering Informatics,* vol. 50, 2021, doi: 10.1016/j.aei.2021.101405.
[130] T. Tang and H. Yuan, "A hybrid approach based on decomposition algorithm and neural network for remaining useful life prediction of lithium-ion battery," *Reliability Engineering & System Safety,* vol. 217, 2022, doi: 10.1016/j.ress.2021.108082.
[131] H.-P. Nguyen, P. Baraldi, and E. Zio, "Ensemble empirical mode decomposition and long short-term memory neural network for multi-step predictions of time series signals in nuclear power plants," *Applied Energy,* vol. 283, 2021, doi: 10.1016/j.apenergy.2020.116346.
[132] J. Wu, C. Wu, S. Cao, S. W. Or, C. Deng, and X. Shao, "Degradation Data-Driven Time-To-Failure Prognostics Approach for Rolling Element Bearings in Electrical Machines," *IEEE Transactions on Industrial Electronics,* vol. 66, no. 1, pp. 529-539, 2019, doi: 10.1109/tie.2018.2811366.
[133] C. Damour, M. Benne, B. Grondin-Perez, M. Bessafi, D. Hissel, and J.-P. Chabriat, "Polymer electrolyte membrane fuel cell fault diagnosis based on empirical mode decomposition," *Journal of Power Sources,* vol. 299, pp. 596-603, 2015, doi: 10.1016/j.jpowsour.2015.09.041.
[134] X. Zhang, Z. He, Z. Zhan, and T. Han, "Performance degradation analysis and fault prognostics of solid oxide fuel cells using the data-driven method," *International Journal of Hydrogen Energy,* vol. 46, no. 35, pp. 18511-18523, 2021, doi: 10.1016/j.ijhydene.2021.01.126.
[135] S. Fu, Y. Zhang, L. Lin, M. Zhao, and S.-s. Zhong, "Deep residual LSTM with domain-invariance for remaining useful life prediction across domains," *Reliability Engineering & System Safety,* vol. 216, 2021, doi: 10.1016/j.ress.2021.108012.
[136] Z. Shi and A. Chehade, "A dual-LSTM framework combining change point detection and remaining useful life prediction," *Reliability Engineering & System Safety,* vol. 205, 2021, doi: 10.1016/j.ress.2020.107257.
[137] K. Cho *et al.*, "Learning phrase representations using RNN encoder-decoder for statistical machine translation," *arXiv preprint arXiv:1406.1078,* 2014.
[138] J. Chung, C. Gulcehre, K. Cho, and Y. Bengio, "Empirical evaluation of gated recurrent neural networks on sequence modeling," *arXiv preprint arXiv:1412.3555,* 2014.
[139] J. Chen, H. Jing, Y. Chang, and Q. Liu, "Gated recurrent unit based recurrent neural network for remaining useful life prediction of nonlinear deterioration process," *Reliability Engineering & System Safety,* vol. 185, pp. 372-382, 2019, doi: 10.1016/j.ress.2019.01.006.

List of Figures

List of Tables